SANDIA REPORT

SAND2015-7952
Unlimited Release
Printed September 2015

Science-based design of stable quantum dots for energy-efficient lighting

James E. Martin, Lauren E. Rohwer, Frank B. van Swol, Xiawong Zhou, and Ping Lu

Prepared by
Sandia National Laboratories
Albuquerque, New Mexico 87185 and Livermore, California 94550

Sandia National Laboratories is a multi-program laboratory managed and operated by Sandia Corporation, a wholly owned subsidiary of Lockheed Martin Corporation, for the U.S. Department of Energy's National Nuclear Security Administration under contract DE-AC04-94AL85000.

Issued by Sandia National Laboratories, operated for the United States Department of Energy by Sandia Corporation.

Available to DOE and DOE contractors from
U.S. Department of Energy
Office of Scientific and Technical Information
P.O. Box 62
Oak Ridge, TN 37831

Telephone: (865) 576-8401
Facsimile: (865) 576-5728
E-Mail: reports@osti.gov
Online ordering: http://www.osti.gov/scitech

Available to the public from
U.S. Department of Commerce
National Technical Information Service
5301 Shawnee Rd
Alexandria, VA 22312

Telephone: (800) 553-6847
Facsimile: (703) 605-6900
E-Mail: orders@ntis.gov
Online order: http://www.ntis.gov/search

SAND2015-7952
Unlimited Release
Printed September 2015

Science-based design of stable quantum dots for energy-efficient lighting

James E. Martin, Lauren E. Rohwer, Frank B. van Swol , Xiawong Zhou, and Ping Lu
Sandia National Laboratories
P.O. Box 5800, MS 1415
Albuquerque, New Mexico 87185-1415

II-VI quantum dots, such as CdSe and CdTe, are attractive as downconversion materials for solid-state lighting, because of their narrow linewidth, tunable emission. However, for these materials to have acceptable quantum yields (QYs) requires that they be coated with a II-VI shell material whose valence band offset serves to confine the hole to the core. Confinement prevents the hole from accessing surface traps that lead to nonradiative decay of the exciton. Examples of such hole-confined core/shell QDs include CdTe/CdSe and CdSe/CdS. Unfortunately, the shell can also cause problems due to lattice mismatch, which ranges from 4-6% for systems of interest. This lattice mismatch can create significant interface energies at the heterojunction and places the core under radial compression and the shell under tangential tension. At elevated temperatures (~240°C) interfacial diffusion can relax these stresses, as can surface reconstruction, which can expose the core, creating hole traps. But such high temperatures favor the hexagonal Wurtzite structure, which has lower QY than the cubic zinc blende structure, which can be synthesized at lower temperatures, ~140°C. In the absence of alloying the core/shell structure can become metastable, or even unstable, if the shell is too thick. This can cause result in an irregular shell or even island growth. But if the shell is too thin thermally-activated transport of the hole to surface traps can occur. In our LDRD we have developed a fundamental atomistic modeling capability, based on Stillinger-Weber and Bond-Order potentials we developed for the entire II-VI class. These pseudo-potentials have enabled us to conduct large-scale atomistic simulations that have led to the computation of phase diagrams of II-VI QDs. These phase diagrams demonstrate that at elevated temperatures the zinc blende phase of CdTe with CdSe grown on it epitaxially becomes thermodynamically unstable due to alloying. This is accompanied by a loss of hole confinement and a severe drop in the QY and emission lifetime, which is confirmed experimentally for the zinc blende core/shell QDs prepared at low temperatures. These QDs have QYs as high as 95%, which makes them very attractive for lighting. Finally, to address strain relaxation in these materials we developed a model for misfit dislocation formation that we have validated through atomistic simulations.

ACKNOWLEDGEMENTS

Sandia National Laboratories is a multi-program laboratory managed and operated by Sandia Corporation, a wholly owned subsidiary of Lockheed Martin Corporation, for the US Department of Energy's National Nuclear Security Administration under contract DE-AC04-94AL85000. This work was performed under a Laboratory Directed Research and Development (LDRD) project.

CONTENTS

ACKNOWLEDGEMENTS 4

Nomenclature 9

CHAPTER 1: An analytical bond-order potential for the Cd-Te-Se ternary system 11

I. INTRODUCTION 11

II. BOND-ORDER POTENTIAL EXPRESSIONS 13

III. PARAMETERIZATION 17

IV. EVALUATION OF THE POTENTIAL 21
- IV.1 Small-Cluster Properties 21
- IV.2 Bulk Lattice Structures 24
- IV.3 Elastic Constants 27
- IV.4 Melting Temperature 28
- IV.5 Point Defects 28
- IV.6 Surface Reconstructions 32
- IV.7 Vapor Deposition Simulations 34

V. CONCLUSIONS 40

APPENDICES 41
- APPENDIX 1-A Target Structures 41
- APPENDIX 1-B Parameter Bounds 42
- A 46

CHAPTER 2: Thermodynamic Properties of Model CdTe/CdSe Mixtures. 51

Abstract 51

Acknowledgements 52

VI. INTRODUCTION 53

VII. Simulation methods 55

VIII. Results 59
- VIII.1 Phase behavior 62
- VIII.2 Simulations of Finite Samples 63
- VIII.3 Surface energy 67

IX. DISCUSSIONS AND CONCLUSIONS 69

appendices 71
- Appendix 2-A 71
- Appendix 2-B 73

CHAPTER 3: HETEROJUNCTIONS of MODEL CdTe/CdSe MIXTURES. 77

Abstract 77

Acknowledgements 78

X. Introduction 79
XI. Results 81
XII. Conclusions 91
CHAPTER 4: Radiative Lifetimes of Zincblende CdSe/CdS Quantum Dots 93
Abstract 93
XIII. Introduction 95
XIV. Results and Discussion 97
XV. Experimental Methods 107
XV.1 Optical measurements 107
XV.2 Synthesis and sample preparation 107
CHAPTER 5: An Atomistically Validated Continuum Model for Strain Relaxation and Misfit Dislocation Formation 111
ABSTRACT 111
ACKNOWLEDGEMENTS 113
XVI. INTRODUCTION 115
XVII. DERIVATION OF MISFIT DISLOCATION ENERGY EXPRESSION 117
XVIII. CONTINUUM ENERGY OF DISLOCATION DIPOLES UNDER PERIODIC BOUNDARY CONDITIONS 125
XIX. MD GEOMETRY OF STRAIN RELAXATION, AND CALCULATIONS OF LATTICE AND ELASTIC CONSTANTS OF OUR MODEL SYSTEM 129
XIX.1 Geometry of the Strain Relaxation Problem 129
XIX.2 MD Calculations of Lattice Constants 130
XIX.3 C. MD Calculations of Young's Modulus 131
XX. MD CALCULATIONS OF CdTe AND CdS DISLOCATION DIPOLE ENERGIES UNDER PERIODIC BOUNDARY CONDITIONS 133
XX.1 A. Effect of System Size 133
XX.2 B. Effect of Dislocation Dipole Distance 135
XXI. EXAMINATION OF CONTNUUM MISFIT DISLOCATION THEORY USING MD SIMULATIONS 137
XXII. CONCLUSIONS 141
XXIII. 9. Distribution 143

Figures

Figure 1-1. Cohesive energies per atom for selected clusters.....22
Figure 1-2. Atomic volumes for selected clusters.....23
Figure 1-3. Cohesive energies per atom for selected lattices.....25
Figure 1-4. Atomic volumes for selected lattices.....26
Figure 1-5. Defect energies obtained from different models for the CdTe-zb and CdSe-zb phases.....31
Figure 1-6. Possible surface reconstructions on (010) zb surface.....32
Figure 1-7. Surface energy phase diagrams predicted by the BOP.....33
Figure 1-8. Surface energy phase diagrams predicted by the SW potential.....34
Figure 1-9. BOP prediction of the Se-A8 structure deposited in the [0001] direction.....36
Figure 1-10. BOP prediction of the Te0.50Se0.50-A8 structure deposited in the [0001] direction.....37
Figure 1-11. BOP prediction of the CdSe-zb structure deposited in the [010] direction.....39
Figure 1-12. BOP prediction of the CdTe0.5Se0.5-zb structure deposited in the [010] direction.....36
Figure 2-1. The lattice parameter as a function of composition (mole fraction of Se).....56
Figure 2-2. Volume per particle as a function of composition (mole fraction of Se).....57
Figure 2-3. The lattice excess volume per particle, $v^{ex}{}_{12} \equiv v12 - v^{id}{}_{12}$.....60
Figure 2-4. The potential energy per particle as a function of composition, for a compound mixture of $CdTe_{1-x}Se_x$.....62
Figure 2-5. The excess potential energy per particle, or enthalpy of mixing ($\Delta H/N$).....64
Figure 2-6. (a) The excess Gibbs free energy per particle as a function of composition.....65
Figure 2-6. (b) The coexistence composition envelope as a function of temperature.....63
Figure 2-7. Image of the cubic nanoparticle of $CdTe_{1-x}Se_x$, $x = 0.2$.....66
Figure 2-8. The bond length R_{CdCd} as a function of composition.…….....67
Figure 2-9. The surface energy versus the mole fraction of Se for a cube.....68
Figure 2-10. The excess surface energy versus the mole fraction of Se for a cube.....69
Figure 2-A-1. The lattice parameter as a function of mole fraction for a substitutional fcc crystal.....72
Figure 2-B-1. The lattice parameter as a function of mole fraction for a substitutional zincblende crystal.....73
Figure 3-1. Curved minimum energy configuration of a bilayer sheet of CdSe (left layer) and CdTe (right layer).....80
Figure 3-2. Curved minimum energy configuration of a bilayer sheet of CdSe (left layer) and CdTe (right layer).....81
Figure 3-3. Sketch of the one-dimensional model used to analyze the crystal plane deflections.....82
Figure 3-4. One-dimensional model of the layer deflection for a bilayer sheet.....84
Figure 3-5. The effects of asymmetry in a CdSe/CdTe bilayer.....85
Figure 3-6. The displacement per particle as a function of the slope.....88
Figure 4-1. Absorption spectra of 2.64 nm zincblende CdSe QDs and corresponding 98
Figure 4-2. Normalized photoluminescence spectra of the same QDs as in Figure 1..... 98
Figure 4-3. TEM image of the core/shell particles having an absorption maximum at.....100

Figure 4-4. Exciton wavelength map assuming no core-shell interdiffusion.....102
Figure 4-5. Radiative lifetime as a function of the wavelength of the lowest energy exciton.....105
Figure 5-2. Geometry of a dislocation array under a surface.....120
Figure 5-3. Comparison between f(x) and 4□x in (a) a rough and (b) a fine scale.....122
Figure 5-4. (a) Dislocation dipoles under periodic boundary conditions.....125
Figure 5-4.(b) interaction of a positive dislocation.....125
Figure 5-5. MD Geometry of the CdTe on CdS structures.....130
Figure 5-6. Strain energy density of CdS and CdTe.....132
Figure 5-7. CdS dislocation line energy as a function of system dimension.....134
Figure 5-8. CdS and CdTe dislocation energies as a function of dislocation dipole distance...136
Figure 5-9. Comparison between the MD and continuum models.....139

List of Tables

Table 1-1. Global and point-dependent BOP Parameters…….17
Table 1-2. Pair-dependent BOP parameters……..…….18
Table 1-3. Three-body-dependent BOP parameters.....18
Table 1-4. BOP prediction of heat of formation ΔH_f (eV/atom) of various phases……..…..27
Table 1-5. Elastic Constants C_{11}, C_{12}, C_{44} (GPa) and melting temperatures T_m (K) of CdTe-zb and CdSe-zb….....…….…27
Table 1-B-1. Bounds on BOP parameters……..……....42
Table 1-C-1. Cohesive energies E_c (eV/atom)…….……..….46
Table 1-C-2. Cohesive energies E_c (eV/atom), lattice constants a, b, c (Å).....47
Table 1-C-3. Intrinsic defect energy $E_D^{'}$ (eV) obtained from different models for CdTe-zb and CdSe-zb.....50
Table 2-1. The Stillinger-Weber potential parameters for the ternary $CdTe_{1-x}Se_x$…..…..…….54
Table 2-2. Basic simulation results for the structure and energies of the pure compounds CdTe and CdSe, at two temperatures.....59
Table 5-1. Dislocation core radius r_0 (Å), core energy E_c (eV/Å), and apparent Young's modulus E (eV/Å^3)……..136

NOMENCLATURE

DOE	Department of Energy
SNL	Sandia National Laboratories

CHAPTER 1: AN ANALYTICAL BOND-ORDER POTENTIAL FOR THE CD-TE-SE TERNARY SYSTEM

I. INTRODUCTION

Photoluminescent CdTe quantum dots (QDs) have the potential to replace rare earth elements (Y, Eu, Tb, and Ce) for low-cost optoelectronic applications [1]. As QDs do not suffer from the defects typically seen in lattice-mismatched films, they can lead to improved solid-state lighting devices as compared to the multilayered structures (e.g., $In_xGa_{1-x}N/GaN$). To meet the extreme lighting environments, these QDs must have sufficient photo- and thermal stability. Increased stability can be achieved by coating the CdTe QD cores with CdSe shells, but these lead to stresses that generate compositional and structural defects both at the heterojunctions and within the lattice. Such defects serve as nonradioactive recombination centers that greatly reduce the quantum yield. To stimulate innovative ideas for new designs of QDs that have both high stability and quantum yield, predictive molecular dynamics (MD) simulations are needed for exploring effects of atomistic scale characteristics (e.g., core radii, shell thicknesses, and graded compositions at the interface) on the stresses and defects. For CdTe/CdS core/shell structures, this requires a Cd-Te-Se interatomic potential that is transferrable to a variety of environments including Cd, Te, Se elements, CdTe, CdSe, and $CdTe_{1-x}Se_x$ compounds, other possible solid solutions, and various defects.

Specific metrics can be used to determine if an interatomic potential is transferrable. In principle, a potential can be confidently said to be transferable when it satisfies simultaneously two criteria: it captures property trends of a variety of pre-designated clusters, lattices, defects, and surfaces as determined from density function theory (DFT) calculations, and it correctly predicts the crystalline growth of ground state structures during high-temperature molecular dynamics simulations of growth (e.g., vapor deposition). Note that due to Arrhenius equation, the kinetics near the melting temperature can be increased by ten orders of magnitude or more as compared to that at temperatures three to four hundred degrees below. High temperature simulations, therefore, can mitigate the effects of the accelerated growth rates that are always used in MD deposition simulations due to computational cost.

The deposition simulation criterion is extremely important because by randomly adding adatoms on the growth surface, it not only tests a variety of surface configurations that cannot be tested in other simulations, but also allows realistic defect configurations to be predicted from natural material synthesis without any assumptions. In particular, if a potential prescribes a wrong structure to have a lower energy than the equilibrium substrate, wrong configurations are likely to be triggered during the deposition simulation resulting in unphysical amorphous growth. Unfortunately, deposition simulation tests are not regularly used in past potential developments.

Developing a "growth simulation enabling" interatomic potential is far more challenging than optimizing the potential against known structures because the former is required to address unlimited structures not included in the training set. Particularly for higher fidelity potentials that are typically more flexible for fitting a variety of structures, there are no obvious ways to ensure the lowest energy for the ground state phase as compared to any other configurations not

[1] A. Mandal, J. Saha, and G. De, Opt. Mater., 34, 6 (2011).

included in the training set. As a result, literature potentials, especially the more advanced ones, often fail to predict the crystalline growth [2].

As an exception, Stillinger-Weber potentials [3] are empirically designed to give the lowest energy for tetrahedrally bonded structures (e.g., diamond cubic, zinc-blende, or wurtzite crystals) and so they can be easily parameterized to enable the crystalline growth of zinc-blende semiconductor compounds. Due to this simplicity, SW potential is the most widely used semiconductor potential. We found that the key for a multi-element SW potential to correctly predict growth is to capture exactly the experimental structures, lattice constants, cohesive energies, and bulk moduli of all stoichiometric compounds, the experimental cohesive energies for the model elements, and the correct positive heat of mixing for all the non-stoichiometric alloys. The literature SW potentials that failed in the growth simulations are likely not fitted to these important properties. By fitting these properties, we developed a SW potential for the II-VI elements Zn-Cd-Hg-S-Se-Te [4]. This potential is successfully used to simulate the crystalline growth of two extremely challenging structures: a $(Cd_{0.28}Zn_{0.68}Hg_{0.04})(Te_{0.20}Se_{0.18}S_{0.62})$ super alloyed compound film on ZnS, and a ZnS/CdSe/HgTe compound multilayer on ZnS [4]. This is also the only literature potential currently available for studying the Cd-Te-Se system.

Due to their fundamental limitations, SW potentials are not transferrable to many elemental structures. This may not be a serious problem under stoichiometric compound conditions where no elemental phases can form. To design CdTe/CdS core/shell structures with any compositions, an interatomic potential that is more fundamental than SW potential is desired. The analytical bond order potentials (BOP) we recently developed for the Cd-Te binary [5] and the Cd-Zn-Te [6] ternary systems represent one example of such potentials. This BOP is uniquely attractive because it is analytically derived from quantum-mechanical theories [7,8,9,10,11] and is therefore fundamentally transferable to environments not explicitly tested. In particular, we demonstrated [5,6] that our Cd-Zn-Te BOP captures the property (i.e. atomic energies, atomic volumes, elastic constants, and melting temperatures) trends of a variety of structures including clusters, bulk lattices, point defects, and surfaces, and can predict crystalline growth of both elements and compounds during MD vapor deposition simulations. The potential has also been used to capture crystalline growth from melt [12].

BOP is not trivial to develop. The present paper looks to develop a ternary BOP for Cd-Te-Se. In addition to refining the parameters of the existing Cd-Te binary BOP, we require that our Cd-Te-Se BOP additionally captures property trends of a large number of Se, Cd-Se, Te-Se, and Cd-Te-Se clusters and lattices as compared with available experiments and density functional theory (DFT) data. Most critically, we validate that this Cd-Te-Se BOP correctly predicts the crystalline growth of Se element as well as CdSe and $CdTe_{1-x}Se_x$ compounds, and also correctly predicts the growth of the experimentally observed continuous $Te_{1-x}Se_x$ solid solution [13]. The work can have multiple impacts: it will further improve the simulations on CdTe/CdSe quantum

---

2 D. K. Ward , X. W. Zhou, B. M. Wong, F. P. Doty, and J. A. Zimmerman, J. Chem. Phys. 134, 244703 (2011).
3 F. H. Stillinger and T. A. Weber, Phys. Rev. B 31, 5262 (1985).
4 X. W. Zhou, D. K. Ward, J. E. Martin, F. B. van Swol, J. L. Cruz-Campa, and D. Zubia, Phys. Rev. B, 88, 085309 (2013).
5 D. K. Ward, X. W. Zhou, B. M. Wong, F. P. Doty, and J. A. Zimmerman, Phys. Rev. B, 85, 115206 (2012).
6 D. K. Ward, X. W. Zhou, B. M. Wong, F. P. Doty, and J. A. Zimmerman, Phys. Rev. B, 86, 245203 (2012).
7 D. G. Pettifor, M. W. Finnis, D. Nguyen-Manh, D. A. Murdick, X. W. Zhou, and H. N. G. Wadley, Mater. Sci. Eng. A, 365, 2 (2004).
8 D. G. Pettifor, and I. I. Oleinik, Phys. Rev. Lett., 84, 4124 (2000).
9 D. G. Pettifor, and I. I. Oleinik, Phys. Rev. B, 65, 172103 (2002).
10 R. Drautz, D. Nguyen-Manh, D. A. Murdick, X. W. Zhou, H. N. G. Wadley, and D. G. Pettifor, TMS Lett., 1, 31 (2004).
11 R. Drautz, D. A. Murdick, D. Nguyen-Manh, X. W. Zhou, H. N. G. Wadley, and D. G. Pettifor, Phys. Rev. B, 72, 144105 (2005).
12 X. W. Zhou, D. K. Ward, B. M. Wong, and F. P. Doty, Phys. Rev. Lett. 108, 245503 (2012).
13 R. C. Sharma, D. T. Li, and Y. A. Chang, Se-Te (Selenium-Tellurium), Ed. By T. B. Massalski, H. Okamoto, P. R. Subramanian, and L. Kacprzak, *Binary Alloy Phase Diagrams*, p. 3344, 2nd ed., Vol. 3, (ASM International, 1990).

dots, provide a more fundamental model to compare with the SW potential, and move significantly towards developing a first-ever quaternary Cd-Te-Zn-Se BOP in a future effort.

II. BOND-ORDER POTENTIAL EXPRESSIONS

The BOP has been implemented in public parallel MD code LAMMPS [14,15]. The potential formalism is rather complex. For a convenient understanding of the BOP, its mathematic formulation is first outlined. In the framework of the BOP [5], the total energy of a system containing N atoms (i = 1, 2, … N) is expressed as

$$E = \frac{1}{2}\sum_{i=1}^{N}\sum_{j=i_1}^{i_N}\phi_{ij}(r_{ij}) - \sum_{i=1}^{N}\sum_{j=i_1}^{i_N}\beta_{\sigma,ij}(r_{ij})\,\Theta_{\sigma,ij} - \sum_{i=1}^{N}\sum_{j=i_1}^{i_N}\beta_{\pi,ij}(r_{ij})\,\Theta_{\pi,ij} \tag{1}$$

where $\phi_{ij}(r_{ij})$, $\beta_{\sigma,ij}(r_{ij})$, and $\beta_{\pi,ij}(r_{ij})$ are pair functions, and $\Theta_{\sigma,ij}$ and $\Theta_{\pi,ij}$ are many-body functions corresponding respectively to σ and π bond-orders, and the list $j = i_1, i_2, \ldots, i_N$ represents neighbors of atom i. $\phi_{ij}(r_{ij})$, $\beta_{\sigma,ij}(r_{ij})$, and $\beta_{\pi,ij}(r_{ij})$ are expressed in a general form as

$$\phi_{ij}(r_{ij}) = \phi_{0,ij}\cdot f_{ij}(r_{ij})^{m_{ij}}\cdot f_{c,ij}(r_{ij}) \tag{2}$$

$$\beta_{\sigma,ij}(r_{ij}) = \beta_{\sigma,0,ij}\cdot f_{ij}(r_{ij})^{n_{ij}}\cdot f_{c,ij}(r_{ij}) \tag{3}$$

$$\beta_{\pi,ij}(r_{ij}) = \beta_{\pi,0,ij}\cdot f_{ij}(r_{ij})^{n_{ij}}\cdot f_{c,ij}(r_{ij}) \tag{4}$$

where $\phi_{0,ij}$, $\beta_{\sigma,0,ij}$, $\beta_{\pi,0,ij}$, m_{ij}, and n_{ij} are pair (ij) dependent parameters, $f_{ij}(r_{ij})$ is a Goodwin-Skinner-Pettifor (GSP) radial function [16], and $f_{c,ij}(r_{ij})$ is a cutoff function. The GSP and the cutoff functions are written respectively as

$$f_{ij}(r_{ij}) = \frac{r_{0,ij}}{r_{ij}}\exp\left[\left(\frac{r_{0,ij}}{r_{c,ij}}\right)^{n_{c,ij}} - \left(\frac{r_{ij}}{r_{c,ij}}\right)^{n_{c,ij}}\right] \tag{5}$$

and

$$f_{c,ij}(r_{ij}) = \begin{cases} \dfrac{\exp\left(-\alpha_{ij}\cdot r_{ij}^{\gamma_{ij}}\right) - \exp\left(-\alpha_{ij}\cdot r_{cut,ij}^{\gamma_{ij}}\right)}{\exp\left(-\alpha_{ij}\cdot r_{1,ij}^{\gamma_{ij}}\right) - \exp\left(-\alpha_{ij}\cdot r_{cut,ij}^{\gamma_{ij}}\right)}, & r_{ij} < r_{cut,ij} \\ 0, & r_{ij} \geq r_{cut,ij} \end{cases} \tag{6}$$

where $r_{0,ij}$, $r_{c,ij}$, $n_{c,ij}$, $r_{1,ij}$, $r_{cut,ij}$ are independent pair parameters (in particular, $r_{cut,ij}$ represents the cutoff distance of the potential), and γ_{ij}, and α_{ij} are dependent pair parameters defined as

---

14 LAMMPS download site: lammps.sandia.gov.
15 S. Plimpton, J. Comp. Phys. 117, 1 (1995).
16 L. Goodwin, A. J. Skinner, and D. G. Pettifor, Europhys. Lett, 9, 701 (1989).

$$\gamma_{ij} = \frac{\ln\left[\ln(0.99)/\ln(0.01)\right]}{\ln\left(r_{1,ij}/r_{cut,ij}\right)} \text{ and } \alpha_{ij} = -\frac{\ln(0.99)}{\left(r_{1,ij}\right)^{\gamma_{ij}}}.$$

The σ bond-order $\Theta_{\sigma,ij}$ used in Eq. (1) is calculated as

$$\Theta_{\sigma,ij} = \Theta_{s,ij}\left(\Theta_{\sigma,ij}^{(1/2)}\right)\left[1-\left(f_{\sigma,ij}-\frac{1}{2}\right)\cdot k_{\sigma,ij}\cdot\frac{\beta_{\sigma,ij}^2\left(r_{ij}\right)R_{3\sigma,ij}}{\beta_{\sigma,ij}^2\left(r_{ij}\right)+\frac{\beta_{\sigma,ij}^2\left(r_{ij}\right)\Phi_{2\sigma}^i+\beta_{\sigma,ij}^2\left(r_{ij}\right)\Phi_{2\sigma}^j}{2}+\varsigma_2}\right] \tag{7}$$

where $0 \le f_{\sigma,ij} \le 1$ and $k_{\sigma,ij}$ are respectively band filling and skewing pair parameters, $\Phi_{2\sigma}^i$, $\Phi_{2\sigma}^j$, and $R_{3\sigma,ij}$ are local variables that can be calculated from atom positions, ς_2 is a constant, and $\Theta_{s,ij}$ is a symmetric band-filling function that modifies the half-full valence shell bond-order expression $\Theta_{\sigma,ij}^{(1/2)}$. $\Theta_{s,ij}$ as a function of $\Theta_{\sigma,ij}^{(1/2)}$ can be well described by

$$\Theta_{s,ij}\left(\Theta_{\sigma,ij}^{(1/2)}\right) = \frac{\Theta_0+\Theta_1+S\cdot\Theta_{\sigma,ij}^{(1/2)}-\sqrt{\left(\Theta_0+\Theta_1+S\cdot\Theta_{\sigma,ij}^{(1/2)}\right)^2-4\left(\varepsilon\sqrt{1+S^2}+\Theta_0\cdot\Theta_1+S\cdot\Theta_1\cdot\Theta_{\sigma,ij}^{(1/2)}\right)}}{2} \tag{8}$$

where

$$\begin{cases}\varepsilon = 10^{-10}\\ \Theta_0 = 15.737980\cdot\left(\frac{1}{2}-\left|f_{\sigma,ij}-\frac{1}{2}\right|\right)^{1.137622}\cdot\left|f_{\sigma,ij}-\frac{1}{2}\right|^{2.087779}\\ S = 1.033201\cdot\left\{1-\exp\left[-22.180680\cdot\left(\frac{1}{2}-\left|f_{\sigma,ij}-\frac{1}{2}\right|\right)^{2.689731}\right]\right\}\\ \Theta_1 = 2\cdot\left(\frac{1}{2}-\left|f_{\sigma,ij}-\frac{1}{2}\right|\right)\end{cases} \tag{9}$$

To use Eq. (7), expressions of the half-full bond-order $\Theta_{\sigma,ij}^{(1/2)}$, and local variables $\Phi_{2\sigma}^i$, $\Phi_{2\sigma}^j$, $R_{3\sigma,ij}$, are further needed. $\Theta_{\sigma,ij}^{(1/2)}$ is expressed as

$$\Theta_{\sigma,ij}^{(1/2)} = \frac{\beta_{\sigma,ij}\left(r_{ij}\right)}{\sqrt{\beta_{\sigma,ij}^2\left(r_{ij}\right)+c_{\sigma,ij}\cdot\left[\beta_{\sigma,ij}^2\left(r_{ij}\right)\Phi_{2\sigma}^i+\beta_{\sigma,ij}^2\left(r_{ij}\right)\Phi_{2\sigma}^j\right]+\varsigma_1}} \tag{10}$$

where $c_{\sigma,ij}$ is a pair parameter and ς_1 is a constant. The $\Phi_{2\sigma}^i$ and $\Phi_{2\sigma}^j$ terms have the same formulation except that they are evaluated at the center of atom *i* and atom *j* respectively.

Considering that Eqs. (7) and (10) use only the product $\beta^2_{\sigma,ij}(r_{ij})\cdot\Phi^i_{2\sigma}$, we only give the formula for $\beta^2_{\sigma,ij}(r_{ij})\cdot\Phi^i_{2\sigma}$ as:

$$\beta^2_{\sigma,ij}(r_{ij})\cdot\Phi^i_{2\sigma}=\sum_{\substack{k=i_1\\k\neq j}}^{i_N} g^2_{\sigma,jik}(\theta_{jik})\cdot\beta^2_{\sigma,ik}(r_{ik}) \tag{11}$$

where θ_{jik} is the bond angle at atom i spanning atoms j and k, and the three-body angular function $g_{\sigma,jik}(\theta_{jik})$ is written as

$$\begin{aligned} g_{\sigma,jik}(\theta_{jik})= & \frac{(b_{\sigma,jik}-g_{0,jik})\cdot u^2_{\sigma,jik}-(g_{0,jik}+b_{\sigma,jik})\cdot u_{\sigma,jik}}{2\cdot(1-u^2_{\sigma,jik})}+\frac{g_{0,jik}+b_{\sigma,jik}}{2}\cdot\cos\theta_{jik}+ \\ & \frac{g_{0,jik}-b_{\sigma,jik}+(g_{0,jik}+b_{\sigma,jik})\cdot u_{\sigma,jik}}{2\cdot(1-u^2_{\sigma,jik})}\cdot\cos^2\theta_{jik} \end{aligned} \tag{12}$$

where $g_{0,jik}$, $b_{\sigma,jik}$, and $u_{\sigma,jik}$ are three-body-dependent parameters.

Similarly, we give the product of $\beta^2_{\sigma,ij}(r_{ij})\cdot R_{3\sigma,ij}$ as

$$\beta^2_{\sigma,ij}(r_{ij})\cdot R_{3\sigma,ij}=\sum_{\substack{k=i_1\\k,j=n}}^{i_N} g_\sigma(\theta_{jik})\cdot g_\sigma(\theta_{ijk})\cdot g_\sigma(\theta_{ikj})\beta_{\sigma,ik}(r_{ik})\cdot\beta_{\sigma,jk}(r_{jk}) \tag{13}$$

where $k,j=n$ in the summation indicates that k and j are neighbors.

The π bond-order $\Theta_{\pi,ij}$ used in Eq. (1) is expressed as

$$\begin{aligned} \Theta_{\pi,ij}= & \frac{a_{\pi,ij}\cdot\beta_{\pi,ij}(r_{ij})}{\sqrt{\beta^2_{\pi,ij}(r_{ij})+c_{\pi,ij}\cdot\left(\frac{\beta^2_{\pi,ij}(r_{ij})\cdot\Phi^i_{2\pi}+\beta^2_{\pi,ij}(r_{ij})\cdot\Phi^j_{2\pi}}{2}+\sqrt{\beta^4_{\pi,ij}(r_{ij})\cdot\Phi_{4\pi}+\varsigma_3}\right)+\varsigma_4}}+ \\ & \frac{a_{\pi,ij}\cdot\beta_{\pi,ij}(r_{ij})}{\sqrt{\beta^2_{\pi,ij}(r_{ij})+c_{\pi,ij}\cdot\left(\frac{\beta^2_{\pi,ij}(r_{ij})\cdot\Phi^i_{2\pi}+\beta^2_{\pi,ij}(r_{ij})\cdot\Phi^j_{2\pi}}{2}-\sqrt{\beta^4_{\pi,ij}(r_{ij})\cdot\Phi_{4\pi}+\varsigma_3}+\sqrt{\varsigma_3}\right)+\varsigma_4}} \end{aligned} \tag{14}$$

where $a_{\pi,ij}$ and $c_{\pi,ij}$ are pair parameters, ς_3 and ς_4 are constants, and $\Phi^i_{2\pi}$, $\Phi^j_{2\pi}$, $\Phi_{4\pi}$ are local variables. For calculations using Eq. (14), the $\beta^2_{\pi,ij}(r_{ij})\cdot\Phi^i_{2\pi}$ and $\beta^4_{\pi,ij}(r_{ij})\cdot\Phi_{4\pi}$ terms are further expressed as

$$\beta^2_{\pi,ij}(r_{ij})\cdot\Phi^i_{2\pi}=\sum_{\substack{k=i_1\\k\neq j}}^{i_N}\left[p_{\pi,i}\cdot\beta^2_{\sigma,ik}(r_{ik})\cdot\sin^2\theta_{jik}+(1+\cos^2\theta_{jik})\cdot\beta^2_{\pi,ik}(r_{ik})\right] \tag{15}$$

$$
\begin{aligned}
\beta^4_{\pi,ij}(r_{ij})\cdot\Phi_{4\pi} = {} & \frac{1}{4}\sum_{\substack{k=i_1\\k\neq j}}^{i_N}\sin^4\theta_{jik}\cdot\hat{\beta}^4_{ik}(r_{ik})+\frac{1}{4}\sum_{\substack{k=j_1\\k\neq i}}^{j_N}\sin^4\theta_{ijk}\cdot\hat{\beta}^4_{jk}(r_{jk})+\\
& \frac{1}{2}\sum_{\substack{k=i_1\\k\neq j}}^{i_N}\sum_{\substack{k'=k+1\\k'\neq j}}^{i_N}\sin^2\theta_{jik}\cdot\sin^2\theta_{jik'}\cdot\hat{\beta}^2_{ik}(r_{ik})\cdot\hat{\beta}^2_{ik'}(r_{ik'})\cdot\cos(\Delta\psi_{kk'})+\\
& \frac{1}{2}\sum_{\substack{k=j_1\\k\neq i}}^{j_N}\sum_{\substack{k'=k+1\\k'\neq i}}^{j_N}\sin^2\theta_{ijk}\cdot\sin^2\theta_{ijk'}\cdot\hat{\beta}^2_{jk}(r_{jk})\cdot\hat{\beta}^2_{jk'}(r_{jk'})\cdot\cos(\Delta\psi_{kk'})+\\
& \frac{1}{2}\sum_{\substack{k'=i_1\\k'\neq j}}^{i_N}\sum_{\substack{k=j_1\\k\neq i}}^{j_N}\sin^2\theta_{jik'}\cdot\sin^2\theta_{ijk}\cdot\hat{\beta}^2_{ik'}(r_{ik'})\cdot\hat{\beta}^2_{jk}(r_{jk})\cdot\cos(\Delta\psi_{kk'})
\end{aligned}
\tag{16}
$$

where

$$
\hat{\beta}^2_{ik}(r_{ik}) = p_{\pi,i}\cdot\beta^2_{\sigma,ik}(r_{ik})-\beta^2_{\pi,ik}(r_{ik}),
\tag{17}
$$

$p_{\pi,i}$ is a species-dependent parameter of the central atom i, and $\Delta\psi_{kk'}$ is a four-body dihedral angle. The dihedral angular terms can be calculated using the relation

$$
\cos(\Delta\psi_{kk'}) = \begin{cases}
\dfrac{2(\cos\theta_{kik'}-\cos\theta_{jik'}\cdot\cos\theta_{jik})^2}{\sin^2\theta_{jik}\cdot\sin^2\theta_{jik'}}-1 & \text{for } k \text{ and } k' \text{ neighors of } i \text{ or},\\
\dfrac{2\left(\dfrac{\overrightarrow{ik'}\cdot\overrightarrow{jk}}{\left|\overrightarrow{ik'}\right|\cdot\left|\overrightarrow{jk}\right|}+\cos\theta_{ijk}\cdot\cos\theta_{jik'}\right)^2}{\sin^2\theta_{ijk}\cdot\sin^2\theta_{jik'}}-1 & \text{for } k' \text{ neighbor of } i \text{ and } k \text{ neighbor of } j
\end{cases}
\tag{18}
$$

III. PARAMETERIZATION

Our Cd-Te-Se BOP is parameterized first for the elemental Cd, Te, and Se, then for the binary Cd-Te, Cd-Se and Te-Se, and finally for the ternary Cd-Te-Se. A complete set of BOP parameters for the Cd-Te-Se system are listed in Tables 1-1 to 1-3. Here the ζ_1-ζ_4 constants are the same as the existing Cd-Zn-Te BOP [5,6] whereas the Cd-Te parameters are slightly modified to better capture the lattice constant of the zinc-blende CdTe. The unknown BOP parameters then include one point-dependent parameter p_π for the new element Se, 10 GSP pair parameters r_0, r_c, r_1, r_{cut}, n_c, m, n, ϕ_0, $\beta_{\sigma,0}$, $\beta_{\pi,0}$ and five additional pair parameters c_σ, f_σ, k_σ, c_π, a_π for each of the three new pairs SeSe, CdSe, TeSe, and three three-body-dependent parameters g_0, b_σ, u_σ for each of the 12 new three-bodies CdCdSe, TeCdSe, SeCdSe, CdTeSe, TeTeSe, SeTeSe, CdSeCd, CdSeTe, CdSeSe, TeSeTe, TeSeSe, SeSeSe. Thus, there are a total of 1×1 + 15×3 + 3×12 = 82 parameters to be determined. However, many parameters can be determined prior to the fitting process. In particular, the characteristic bond lengths r_0, r_c, r_1, r_{cut} are selected as shown in Table 1-2 based upon the criteria that r_0 approximately scales with the bond length of the corresponding atomic pair in the equilibrium structure, r_c equals r_0, r_{cut} roughly scales with r_0, and r_1 is midway between r_0 and r_{cut}. The pair parameters c_π and a_π are set to unity as were originally derived for the π bond-order [8,9]. The CdSe zb crystal structure has a half-full valence shell and does not make use of the symmetric and asymmetric σ bond-order terms; therefore, we set f_σ = 0.50 and k_σ = 0 for the Cd-Se bonds. Finally, we set the three-body parameter g_σ to be the normalized value of unity for all the triples as shown in Table 1-3. This leaves 50 parameters to be determined.

Table 1-1. Global and point-dependent BOP Parameters.

Symbol	ζ_1	ζ_2	ζ_3	ζ_4	$p_{\pi,Cd}$	$p_{\pi,Te}$	$p_{\pi,Se}$
Value	0.00001	0.00001	0.00100	0.00001	0.420000	0.460686	0.927195

Table 1-2. Pair-dependent BOP parameters.

Symbol	CdCd	TeTe	SeSe	CdTe	CdSe	TeSe
r_0	3.1276	3.1626	3.0251	2.9677	2.9201	3.0938
r_c	3.1276	3.1626	3.0251	2.9677	2.9201	3.0938
r_1	3.7303	3.8046	3.6392	3.8085	3.7475	3.7219
r_{cut}	4.3330	4.4465	4.2532	4.6494	4.5748	4.3498
n_c	2.800000	2.799998	2.799998	2.811251	2.399466	2.894572
m	3.263155	2.458846	2.372557	2.388647	2.775084	2.156644
n	1.553883	1.223306	1.189927	1.188381	1.460571	1.135076
ϕ_0	0.186369	0.876912	0.672666	0.654330	0.539105	0.675052
$\beta_{\sigma,0}$	0.238318	0.782635	0.524928	0.836402	0.779739	1.015496
$\beta_{\pi,0}$	0.097599	0.531205	0.505465	0.030748	0.108296	0.404592
c_σ	0.561130	1.014809	1.401177	1.196365	0.717742	1.583151
f_σ	0.431863	0.331227	0.446055	0.500000	0.500000	0.305203
k_σ	15.000000	-2.860190	-7.436736	0	0	-7.265823
c_π	1	1	1	1	1	1
a_π	1	1	1	1	1	1

Table 1-3. Three-body-dependent BOP parameters.

Symbol	Cd-centered triples *j*-Cd-*k*					
	CdCdCd	CdCdTe	CdCdSe	TeCdTe	TeCdSe	SeCdSe
g_0	1	1	1	1	1	1
b_σ	0.762039	0.208810	0.600000	0.200000	0.391552	0.388802
u_σ	-0.400000	-0.168759	-0.380000	-0.400000	-0.333334	-0.350000
Symbol	Te-centered triples *j*-Te-*k*					
	CdTeCd	CdTeTe	CdTeSe	TeTeTe	TeTeSe	SeTeSe
g_0	1	1	1	1	1	1
b_σ	0.259985	0.807985	0.200000	0.669623	0.600000	0.311637
u_σ	-0.400000	0.022436	-0.217561	-0.141521	0.000000	-0.345072
Symbol	Se-centered triples *j*-Se-*k*					
	CdSeCd	CdSeTe	CdSeSe	TeSeTe	TeSeSe	SeSeSe
g_0	1	1	1	1	1	1
b_σ	0.325924	0.810916	0.600000	0.427183	0.261943	0.381759
u_σ	-0.350000	-0.229874	-0.349551	-0.380000	-0.095495	0.000000

Parameterizing a BOP that is capable of growth simulations can be quite challenging, requiring a large number of iterations. For the Cd-Te-Se system, these iterations resulted in the following rules: (1) include a particular set of target structures as listed in Appendix A and impose appropriate weight factors for these structures in the fitting; (2) apply the particular

bounds for the parameters as shown in Appendix B that are motivated by physical intuition and parameterization results; (3) apply a two-step optimization algorithm as describe below with the key pair parameters first determined by fitting to the nearest-neighbor structures and the remaining parameters fitted to more complex structures; and (4) fully optimize the fitting functions.

Previous work [5] has proven that for the nearest neighbor structures (i.e., dimer, trimer, tetra, dc, sc, fcc, gra, zb, wz, NaCl, etc. where the second nearest neighbor distance is beyond cutoff distance of the potential), the following three relations hold:

$$E_{b,ij}\left(r_{ij,0}\right)=\phi_{ij}\left(r_{ij,0}\right)-\beta_{\sigma,ij}\left(r_{ij,0}\right)\cdot\frac{\phi_{ij}^{'}\left(r_{ij,0}\right)}{\beta_{\sigma,ij}^{'}\left(r_{ij,0}\right)} \tag{19}$$

$$E_{b,ij}^{''}\left(r_{ij,0}\right)=\phi_{ij}^{''}\left(r_{ij,0}\right)-\beta_{\sigma,ij}^{''}\left(r_{ij,0}\right)\cdot\frac{\phi_{ij}^{'}\left(r_{ij,0}\right)}{\beta_{\sigma,ij}^{'}\left(r_{ij,0}\right)} \tag{20}$$

$$2\cdot\beta_{\sigma,0,ij}\cdot\Theta_{\sigma,ij}+2\cdot\beta_{\pi,0,ij}\cdot\Theta_{\pi,ij}=\beta_{\sigma,0,ij}\cdot\frac{\phi_{ij}^{'}\left(r_{ij,0}\right)}{\beta_{\sigma,ij}^{'}\left(r_{ij,0}\right)} \tag{21}$$

where $E_{b,ij}$ and $E_{b,ij}^{''}$ are respectively the energy and the second derivative of the energy of the nearest neighbor bond in the structure at the equilibrium bond length $r_{ij,0}$, $\Theta_{\sigma,ij}$ and $\Theta_{\pi,ij}$ the equilibrium σ and π bond-orders, and subscript *ij* indicates the species of the pair. Note that $\Theta_{\sigma,ij}$ and $\Theta_{\pi,ij}$ are constant when the nearest neighbor structures are subject to the hydrostatic strain. The first step of, a two-step parameterization, determines the pair-wise GSP parameters ϕ_0, m, n, and n_c by fitting Eqs. (19) and (20) to the target values (experimental or DFT data) of bond energies (can be converted from cohesive energies) and second derivatives of bond energies (can be converted from bulk moduli) of a wide range of nearest-neighbor structures with different equilibrium bond lengths. The parameters determined in the first-step enable evaluating the right-hand side of Eq. (21) at the target equilibrium bond lengths for different nearest-neighbor structures. This creates a new set of target values for the combined bond-order term $2\cdot\beta_{\sigma,0,ij}\cdot\Theta_{\sigma,ij}+2\cdot\beta_{\pi,0,ij}\cdot\Theta_{\pi,ij}$. These new target values, along with target properties (cohesive energies, lattice constants, etc.) of non-nearest-neighbor structures, can then be fitted in a second-step to determine the remaining parameters, p_π, $\beta_{\sigma,0}$, $\beta_{\pi,0}$, c_σ, f_σ, k_σ, b_σ, u_σ.

With target properties defined, the potential is optimized using a series of computational tools [17,18,19,20, 21] as detailed previously [5]. Following each fitting iteration the parameters are

17 S. Wolfram, The Mathematica Book, 5th ed. (Wolfram Research, Inc., Champaign, IL, 2004), p. 106ff.
18 M. R. Hestenes, and E. Stiefel, J. Res. National Bureau Stand., 49, 409 (1952).
19 D. M. Olsson, and L. S. Nelson, Technometrics, 17, 45 (1975).
20 R. Storn, and K. Price, J. Global Opt., 11, 341 (1997).
21 S. Kirkpatrick, C. D. Gelatt, and M. P. Vecchi, Science, 220, 671 (1983).

tested for a larger collection of structures and vapor deposition simulations. If spurious results exist (for example, a structure has a lower cohesive energy than the ground-state phase, or vapor deposition simulations predict an amorphous growth of the equilibrium phase), the entire process is repeated with an appropriate adjustment of target structures, target properties, and parameter bounds. The iterations continue until a satisfactory set of potential parameters is obtained. Tables 1-1 – 1-3 list values of a complete set of BOP parameters thus determined for the Cd-Te-Se system including global/point-dependent, pair-dependent, and three-body-dependent parameters, respectively.

IV. EVALUATION OF THE POTENTIAL

Detailed studies [2,5,6] have been performed to compare literature SW [22,23] and Tersoff [24] types of Cd-Te potentials with BOP. These studies indicate that the literature SW potential [25,26] is sufficiently well parameterized for stoichiometric CdTe compound whereas the literature Tersoff-Rockett potential [27] is not sufficiently well parameterized for either Cd and Te elements or CdTe compound. The Cd-Te component of our Zn-Cd-Hg-S-Se-Te SW potential [4] slightly improves on the overall property trends and significantly improves on the Cd property trends over the literature Cd-Te SW potential [28,29]. Hence, the Zn-Cd-Hg-S-Se-Te SW potential [4] provides the most stringent standard for the quality of the Cd-Te-Se potential. Extensive comparisons are therefore made between the predictions by the Cd-Te-Se BOP and the published Zn-Cd-Hg-S-Se-Te SW potentials, the available experimental data, and our high-level DFT calculations on properties of a large number of phases. In particular, geometries and energies of numerous small clusters; lattice constants and cohesive energies of a variety of lattice structures; elastic constants, melting temperature, properties of common point defects (interstitials, vacancies, and antisites), and surface reconstructions of the lowest energy zinc-blende compounds; heat of formation of $Te_{0.25}Se_{0.75}$ and $Te_{0.75}Se_{0.25}$ alloys, and heat of formation of $CdTe_{1-x}Se_x$ alloyed compounds, are all studied. Finally, vapor deposition simulations of a variety of possible phases are explored.

IV.1 Small-Cluster Properties

Based on BOP, SW, and DFT, molecular statics energy minimization simulations are used to calculate relaxed cohesive energies and geometries of a variety of Cd, Te, Se, CdTe, CdSe, and TeSe clusters with different coordination numbers. To provide numerical reference for readers, the results of the calculations are summarized in Table 1-C-1 of Appendix C. To better examine the trends the data listed in Table 1-C-I are plotted in Fig. 1-1 for cohesive energy per atom, and in Fig. 1-2 for atomic volume. Because the volume for clusters is not well defined, we simply use hard sphere model to define atomic volume Ω from bond length r as $\Omega = \frac{4}{3}\pi\left(\frac{r}{2}\right)^3$. It should be noted that while the DFT method captures property trends well, it does not necessarily reproduce the absolute values of the energies and atomic volumes measured from experiments. To realistically compare the results, the DFT data displayed in Figs. 1-1 and 1-2 (as well in Figs. 1-3 and 1-4) are scaled to the experimental values for the Cd-hcp, Te-A8, Se-A8, CdTe-zb, and

22 Z. Q. Wang, D. Stroud, and A. J. Markworth, Phys. Rev. B, **40**, 3129 (1989).
23 Z. Zhang, A. Chatterjee, C. Grein, A. J. Ciani, and P. W. Chung, J. Elect. Mat. 40, 109, 2011.
24 J. Oh, and C. H. Grein, J. Cryst. Growth, **193**, 241 (1998).
25 Z. Q. Wang, D. Stroud, and A. J. Markworth, Phys. Rev. B, **40**, 3129 (1989).
26 Z. Zhang, A. Chatterjee, C. Grein, A. J. Ciani, and P. W. Chung, J. Elect. Mat. 40, 109, 2011.
27 J. Oh, and C. H. Grein, J. Cryst. Growth, **193**, 241 (1998).
28 Z. Q. Wang, D. Stroud, and A. J. Markworth, Phys. Rev. B, **40**, 3129 (1989).
29 Z. Zhang, A. Chatterjee, C. Grein, A. J. Ciani, and P. W. Chung, J. Elect. Mat. 40, 109, 2011.

CdSe-zb phases (for example, the energies and volumes of all the Cd structures are multiplied respectively by a constant energy scaling factor and a constant volume scaling factor so that the scaled DFT values match the experimental data for the equilibrium Cd-hcp phase).

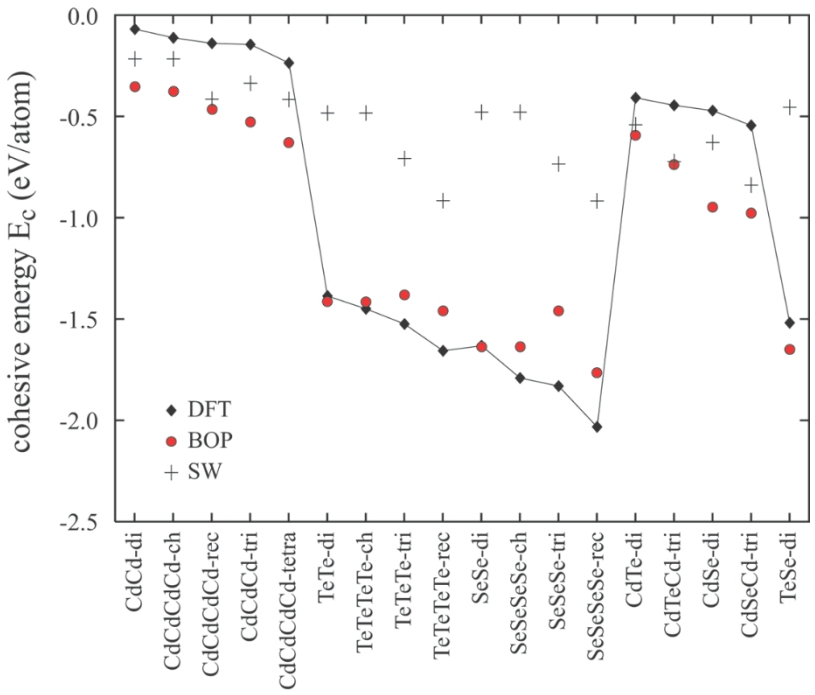

Figure 1-1. Cohesive energies per atom for selected clusters. DFT data are scaled to experimental values of observed phases. Note that the data represent discrete structure, and the line is only used to guide eyes without implying any continuity of the data.

Considering that the DFT data shown in Fig. 1-1 is ordered to give a decreasing energies for each material systems (Cd, Te, Se, CdTe, CdSe, and TeSe), the BOP does an excellent job reproducing the DFT trends from the high (less negative) to low (more negative) energy clusters with the only exceptions being TeTeTe-tri and SeSeSe-tri. This improves over the SW potential. In addition, the overall BOP trends are much closer to the DFT trends than the SW trends.

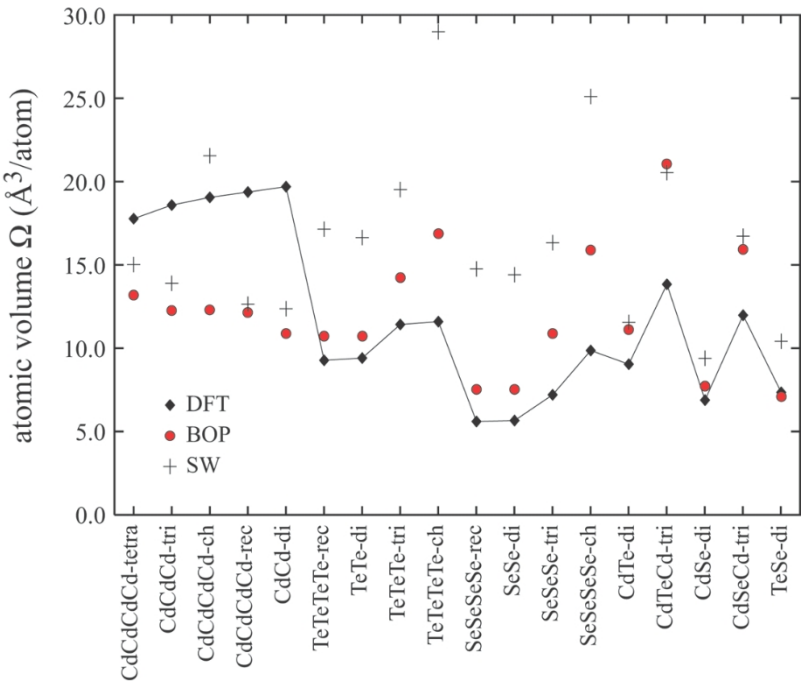

Figure 1-2. Atomic volumes for selected clusters. DFT data are scaled to experimental values of observed phases. Note that the data represent discrete structure, and the line is only used to guide eyes without implying any continuity of the data.

Fig. 1-2 indicated that the atomic volume trends (refers to relative volume between phases, but not the absolute volume) predicted by the BOP match the DFT trends very well except for the Cd clusters where opposite trends are seen. It should be noted, however, the bond energy specified by Eq. (19) monotonically increases as a function of bond length regardless of the parameters. In contrast, the DFT bond energy vs. bond length data is rather scattered. As a result, it is necessary that some differences exist between BOP and DFT. This is also true for Tersoff potentials (which have a similar bond energy vs. bond length relation) [30], and is even more obvious for SW potentials. For example, the angular term vanishes for both the dimer and dc structures in SW potentials. This means that the nearest-neighbor structures such as dime and dc would have the same bond energy, in contrast with the DFT data. When energies and volumes cannot be both captured, a tradeoff is made to capture the more important energies. On the other hand, it can be seen that the BOP values are overall closer to the DFT data than the SW predictions except for the Cd clusters where the BOP values deviate slightly more. Again, it should be noted that DFT does not necessarily represent experiments, and the trends are more important to be captured than the absolute values.

[30] K. Albe, K. Nordlund, J. Nord, and A. Kuronen, Phys. Rev. B, 66, 35205 (2002).

IV.2 Bulk Lattice Structures

Molecular statics energy minimization simulations with flexible volume [31] are also performed to determine the relaxed energies and lattice constants of a variety of Cd, Te, Se, CdTe, CdSe, TeSe, and lattices (see, e.g., Appendix A) with coordination numbers between four and twelve. For convenience of numerical reference, the calculated results are all listed in Table 1-C-2, Appendix C along with the available experimental data [32]. To clearly compare the models, the cohesive energies per atom are plotted in Figs. 1-3(a) and 3(b) for elements and compounds respectively, and the corresponding atomic volumes are plotted in Figs. 1-4(a) and 1-4(b). Again DFT data are scaled to the experimental phases.

Figs. 1-3(a) and 1-3(b) indicate that the cohesive energies of both elements and compounds as predicted by the BOP follow well the DFT trends for each material Cd, Te, Se, CdTe, CdSe, and TeSe. Most phases that deviate from the DFT trends are not the low energy phases and hence do not critically affect the potential. In addition, the absolute cohesive energies are seen to be close to the scaled DFT values, with almost exact match to the experimental energies of the equilibrium phases. Overall, a significant improvement over the SW potential is clear.

Figs. 1-4(a) and 1-4(b) indicate that the atomic volume of both elements and compounds as predicted by the BOP also follow well the DFT trends. Again the phases that deviate the DFT trends are not the low energy phases. The absolute values are also close the DFT data. For important low energy phases, the agreement is very good, and exact agreement with experimental values is achieved for the lowest energy equilibrium phases. Overall, a significant improvement over the SW potential can be clearly identified.

[31] M. Parrinello, and A. Rahman, J. Appl. Phys., 52, 7182 (1981).
[32] I. Barin, *Thermochemical data of pure substances*, (VCH, Weinheim, 1993).

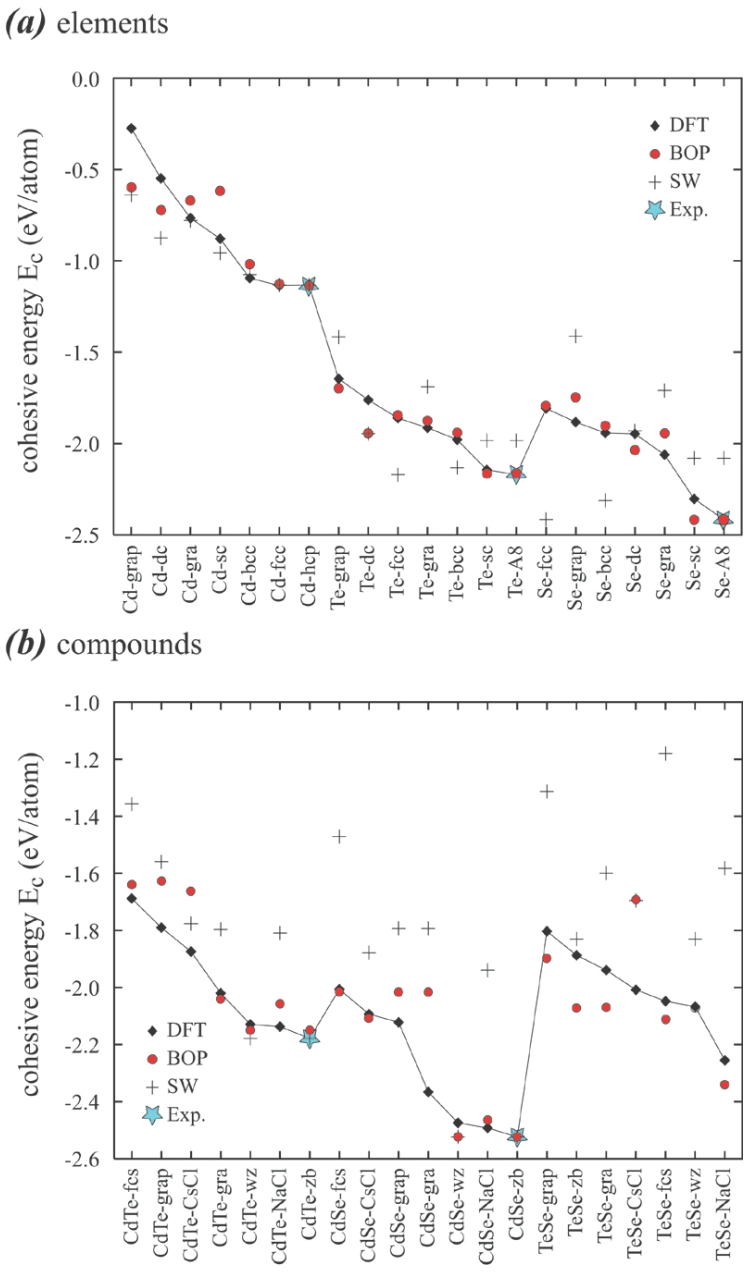

Figure 1-3. Cohesive energies per atom for selected lattices. DFT data are scaled to experimental values of observed phases as indicated by the blue stars. Note that the data represent discrete structure, and the line is only used to guide eyes without implying any continuity of the data.

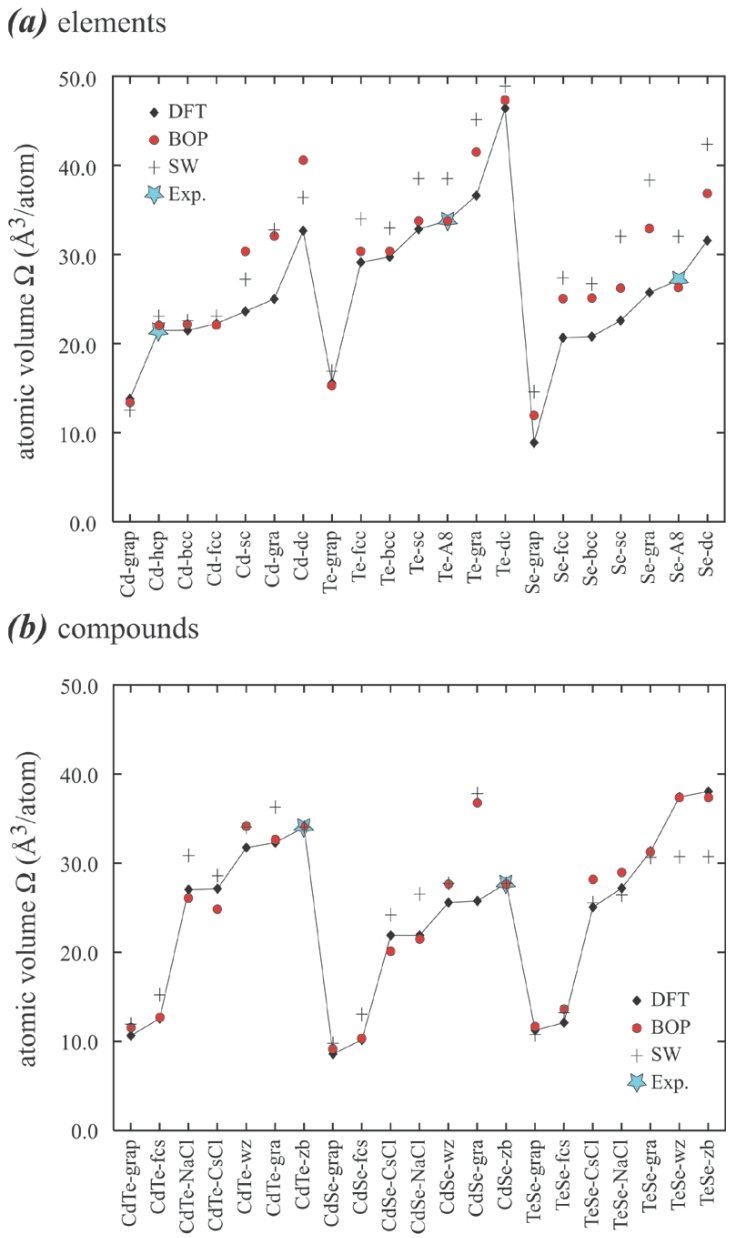

Figure 1-4. Atomic volumes for selected lattices. DFT data are scaled to experimental values of observed phases as indicated by the blue stars. Note that the data represent discrete structure, and the line is only used to guide eyes without implying any continuity of the data.

For multi-element systems, heat of formation is the most important property determining the formation of intermetallic compounds, solid solutions, or separated elements. Heat of formation represents the energy difference between an alloy or compound and its constituent elements. For an $A_{1-x}B_x$ binary alloy, for instance, the heat of mixing is defined as $\Delta H_f = E_{c,AB} - [(1-x)\cdot E_{c,A} + x\cdot E_{c,B}]$, where $E_{c,AB}$ is the cohesive energy of the alloy or the compound, and $E_{c,A}$ and $E_{c,B}$ refer to the cohesive energies of the lowest-energy structure of elements A and B, respectively. Because our BOP reproduces the experimental cohesive energies of the lowest energy elements Cd-hcp, Te-A8, and Se-A8,

and lowest energy compounds CdTe-zb, and CdSe-zb, the heat of formation of CdTe-zb and CdSe-zb is also exact. This means that the BOP can correctly predict the formation of the intermetallic compounds CdTe-zb and CdSe-zb.

Te-Se forms a continuous solid solution on an A8 lattice [13]. To check this, we calculated the heat of formation of two phases $Te_{0.25}Se_{0.75}$-A8 and $Te_{0.75}Se_{0.25}$-A8. The results are shown in Table 1-4. Table 1-4 indicates that they $Te_{0.25}Se_{0.75}$-A8 and $Te_{0.75}Se_{0.25}$-A8 significant negative heat of formation, and are therefore stable. We will demonstrate below that $Te_{0.50}Se_{0.50}$-A8 grows into a crystalline film in MD deposition simulation, more confidently verifying that $Te_{1-x}Se_x$-A8 is stable.

Table 1-4. BOP prediction of heat of formation ΔH_f (eV/atom) of various phases.

Phase	$Te_{0.25}Se_{0.75}$-A8	$Te_{0.75}Se_{0.25}$-A8	Cd_4Te_3Se	$Cd_4Te_2Se_2$	Cd_4TeSe_3
ΔH_f	-0.12	-0.09	-0.55	-0.61	-0.68

BOP-based energy minimizations are also used to calculate relaxed cohesive energies, lattice constants, and heats of formation of three ternary compounds, namely Cd_4Te_3Se, $Cd_4Te_2Se_2$, and $Cd_4Te_1Se_3$, with all atoms populate on an initial zb lattice. The results are compared in Tables 1-C-2 and 1-C-4. It can be seen that BOP predicts decreasing lattice constant and decreasing energy (more negative) with increasing Se content. In addition, BOP predicts negative heats of formation for all the three compounds, Table 1-4, correctly capturing these compounds as the stable structures.

IV.3 Elastic Constants

SW and BOP models are also used to calculate single crystal elastic constants of the CdTe-zb and CdSe-zb phases, and the results are compared with literature experiments [33,34] in Table 1-5. It can be seen that overall, the elastic constants predicted by the BOP are closer to the experimental values than those predicted by the SW potential.

Table 1-5. Elastic Constants C_{11}, C_{12}, C_{44} (GPa) and melting temperatures T_m (K) of CdTe-zb and CdSe-zb.

Structure	SW [4]				BOP				Exp. [33,34]			
	C_{11}	C_{12}	C_{44}	T_m	C_{11}	C_{12}	C_{44}	T_m	C_{11}	C_{12}	C_{44}	T_m
CdTe-zb	63	32	24	1570-1610	52	29	20	1360-1400	53	37	20	1365
CdSe-zb	88	37	36	2200-2300	72	44	24	1780-1790	67	46	22	1537

[33] B. Derby, Phys. Rev. B, 76, 054126 (2007).
[34] M. Gaith, and I. Alhayek, Rev. Adv. Mater. Sci., 21, 183 (2009).

IV.4 Melting Temperature

Melting temperature simulations test a large number of thermally-activated configurations and have implications on modeling thermodynamic properties. Thus, we calculated the melting temperature of the two zb phases CdTe and CdSe. Here the melting temperature is determined as the temperature at an equilibrated liquid / solid interface using the simulation approach developed previously [12]. The results are included in Table 1-5. It can be seen that the melting temperatures predicted by BOP is significantly closer to the experimental values than those predicted by the SW model. In particular, the experimental melting temperature for CdTe is within the predicted range. This is an extremely good agreement for properties like melting temperature.

IV.5 Point Defects

Studying defect properties in CdTe-zb and CdSe-zb crystals further tests the transferability of the Cd-Te-Se BOP potential. Various types of defects can be easily introduced in a zb computational crystal. The stoichiometry of the system containing the defects, however, does not necessarily equal the stoichiometry of the perfect crystal. Following the methodology of Zhang and Northrup [35,36], the defect energy Γ in an AB binary compound is calculated as a function of the chemical potential difference $\Delta\mu$ as

$$\Gamma = E_D^{'} - 0.5(n_A - n_B)\cdot\Delta\mu \tag{22}$$

where n_A and n_B are numbers of A and B atoms in the defective system, $E_D^{'}$ is an intrinsic defect energy at the stoichiometric condition, and $\Delta\mu$ is the chemical potential difference characteristic of the stoichiometry of the environment. $\Delta\mu$ is expressed as

$$\Delta\mu = (\mu_A - \mu_A^{bulk}) - (\mu_B - \mu_B^{bulk}) \tag{23}$$

where μ_A and μ_B are the chemical potentials of A and B in the AB compound, and μ_A^{bulk} and μ_B^{bulk} are the chemical potentials for the lowest energy A and B phases. In our work, all chemical potentials are approximated as cohesive energies per atom unit. Under the equilibrium condition, $\Delta\mu$ satisfies the condition $-\Delta H_f < \Delta\mu < \Delta H_f$ where ΔH_f is heat of formation [36]. In general, $\Delta\mu = 0$, $\Delta\mu > 0$, and $\Delta\mu < 0$ mean stoichiometric, A-rich, and B-rich conditions.

The intrinsic defect energy can be calculated as

$$E_D^{'} = E_D - 0.5(n_A + n_B)\cdot\mu_{AB}^{bulk} - 0.5(n_A - n_B)\cdot(\mu_A^{bulk} - \mu_B^{bulk}) \tag{24}$$

---

35 S. B. Zhang, and J. E. Northrup, Phys. Rev. Lett., 67, 2339 (1991).

36 J. E. Northrup, and S. B. Zhang, Phys. Rev. B, 47, 6791 (1993).

where E_D is the total energy of the system containing the defect, and μ_{AB}^{bulk} is the chemical potential of the lowest energy AB phase. Under the stoichiometric condition, $\Delta\mu = 0$ and $E_D' = \Gamma$. Under the A-rich or B-rich condition, $\Delta\mu \neq 0$ and thus $E_D' \neq \Gamma$.

The AB defects considered here include A vacancy (V_A), B vacancy (V_B), A at B anti-site (A_B), B at A anti-site (B_A), A interstitial surrounded by the B and A tetrahedron shells (notated as $A_{i,B}$ and $A_{i,A}$ respectively), B interstitial surrounded by the A and B tetrahedron shells (notated as $B_{i,A}$ and $B_{i,B}$ respectively).

Energy minimization simulations are performed to calculate the total energies E_D of the AB-zb systems (with about 512 atoms) containing the corresponding defects. The intrinsic defect energies are then calculated using Eq. (24), and the numerical results are given in Table 1-C-3 of Appendix C for reference. To facilitate analysis, these results also plotted in Figs. 1-5(a) and 1-5(b) for CdTe-zb and CdSe-zb respectively.

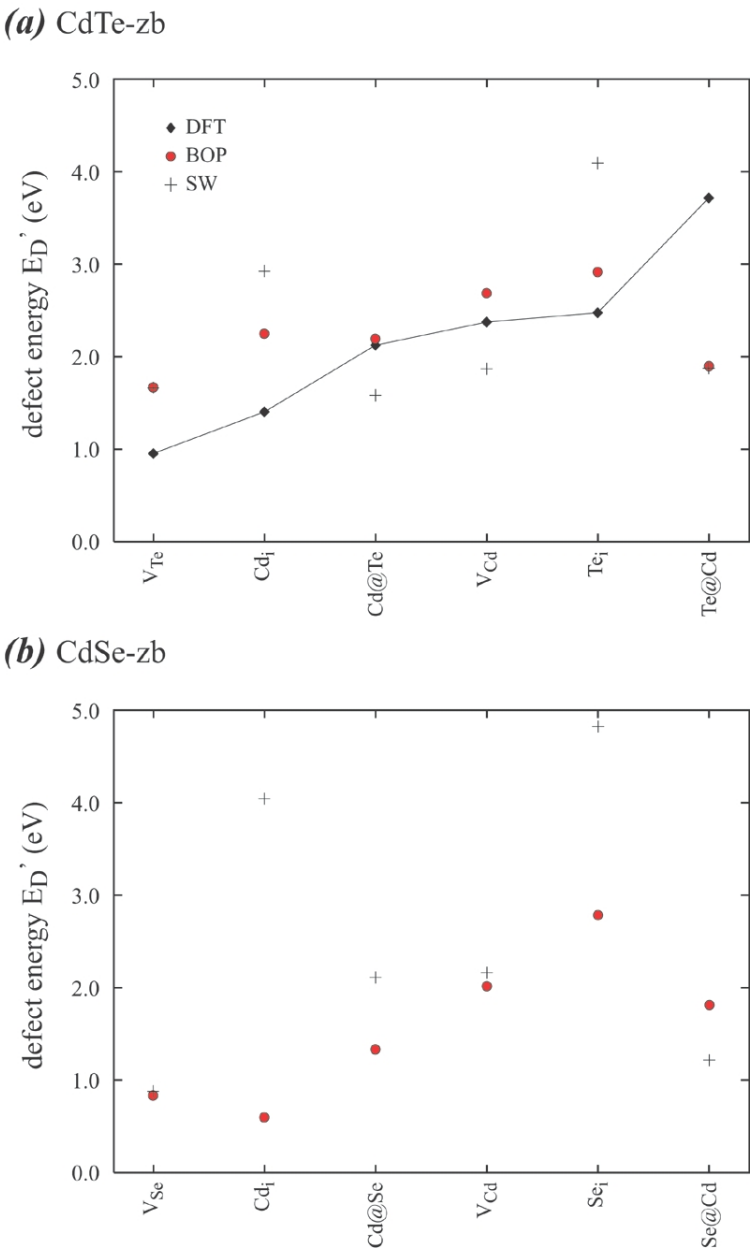

Figure 1-5. Defect energies obtained from different models for the CdTe-zb and CdSe-zb phases.

Fig. 1-5(a) indicates that under the stoichiometric condition, the lowest energy defect in the CdTe-zb crystal, as predicted by the BOP calculations, is the Te vacancy. This agrees with the DFT calculations. The SW potential does not predict Te vacancy as the lowest energy defect. The overall trends of defect energy predicted by the BOP are also seen to be much closer to the DFT trends than those of the SW potential. The only exception is the Te at Cd antisites, where the DFT energy is much higher than the BOP energy. It is noted, however, DFT does predict an abnormally high energy for the Te at Cd anti-site.

Similar BOP defect energy trends are obtained for CdSe as can be seen in Fig. 1-5(b). Overall, it is clear from Fig. 1-5 that BOP is superior to the SW potentials for defect studies.

IV.6 Surface Reconstructions

Surface reconfigurations provide additional tests of the transferability of interatomic potentials. To further evaluate our BOP, we study the (010) surface reconstructions of CdTe-zb and CdSe-zb. The (010) surface of a zb crystal exhibits a variety of surface reconstructions depending on the environment [37,38]. Fig. 1-6 illustrates six observed and postulated reconstructions for three coverage fraction ξ = 0.5, 1.0, and 1.5. Because in AB binary compounds, the surface atoms can be either A or B, Fig. 1-6 can be used to construct 12 surface reconstructions for binary compounds.

BOP- and SW-based energy minimization simulations are used to calculate total energies of the relaxed systems containing various surface reconstructions. The computational cell contains a block of zb crystal with ~600 atoms. The simulations employ periodic boundary conditions in the x and z directions with two parallel free surfaces created in the +/- y directions. The two surfaces are identical except that one is rotated 90° relative to the other. Based on the relaxed total energies, Eq. (22) is used to calculate surface energies as a function of the chemical potential difference $\Delta\mu$, Eq. (23), for all the 12 CdTe-zb (010) surface reconstructions and the 12 CdSe-zb (010) surface reconstructions. The calculated surface energies (per unit of surface cell), are summarized in Figs. 1-7 and 1-8 for BOP and SW potential, respectively, where (a) is for CdTe surfaces, and (b) for CdSe surfaces.

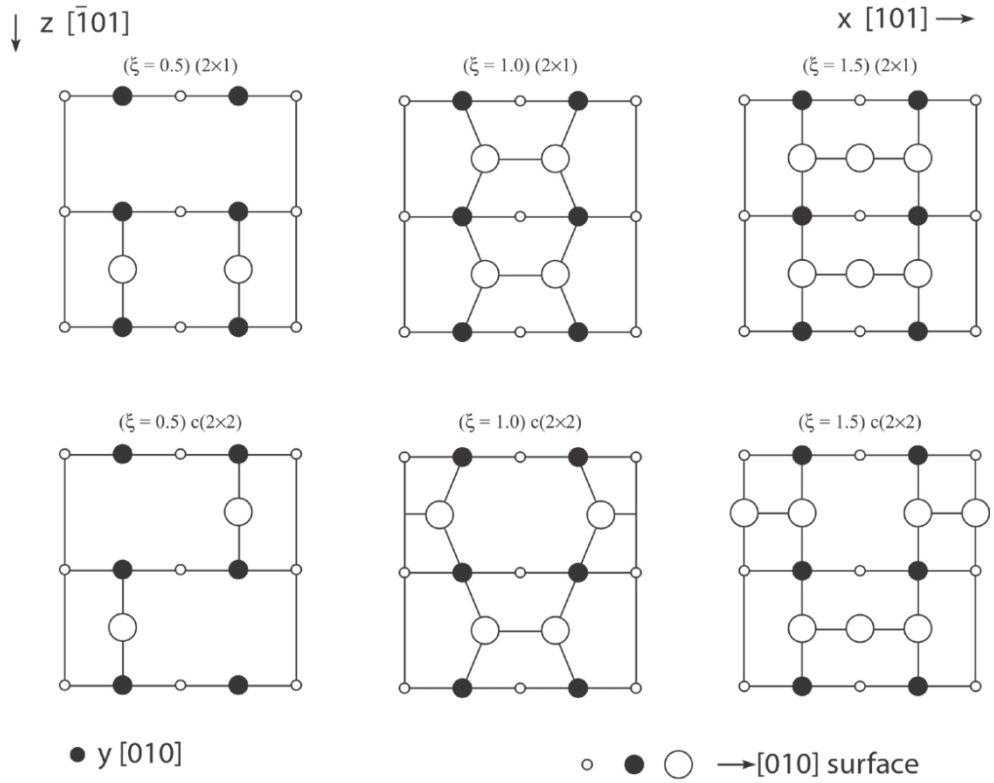

Figure 1-6. Possible surface reconstructions on (010) zb surface.

[37] R. D. Feldman, R. F. Austin, P. M. Bridenbaugh, A. M. Johnson, W. M. Simpson, B. A. Wilson, C. E. Bonner, J. Appl. Phys., 64, 1191 (1988).

[38] B. Daudin, S. Tatarenko, D. Brun-Le Cunff, Phys. Rev. B, 52, 7822 (1995)

Fig. 1-7(a) indicates that within the possible range of chemical potential difference between $-\Delta H_f$ and ΔH_f, the BOP predicts the preferred CdTe-zb (010) surfaces as Te (1×2) (coverage ξ = 1.0) in the Te-rich environments ($\Delta\mu$ near the $-\Delta H_f$ end) and Cd (1×2) (coverage ξ = 1.0) in the Cd-rich environments ($\Delta\mu$ near the ΔH_f end), in good agreement with experiments.

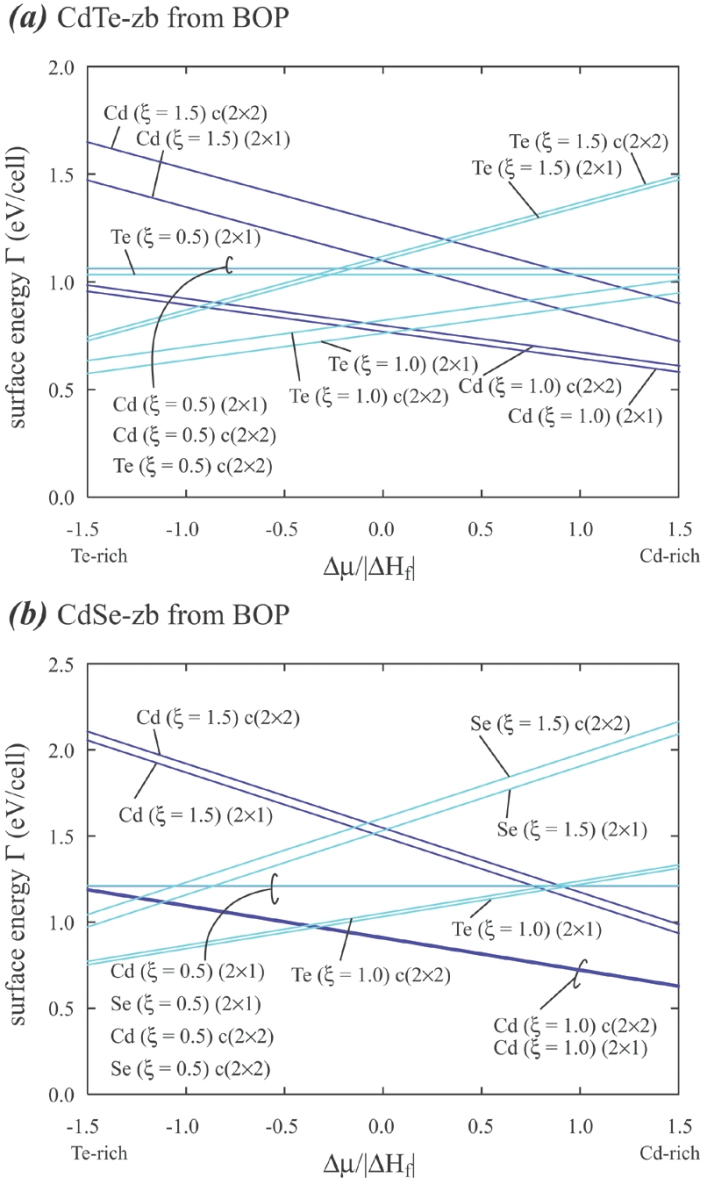

Figure 1-7. Surface energy phase diagrams predicted by the BOP.

Fig. 1-7(b) indicates that the BOP predicts the preferred CdSe-zb (010) surfaces as Te (1×2) (coverage ξ = 1.0) in the Te-rich environments and Cd (1×2) (coverage ξ = 1.0) in the Cd-rich condition, again in good agreement with the experiments for CdSe.

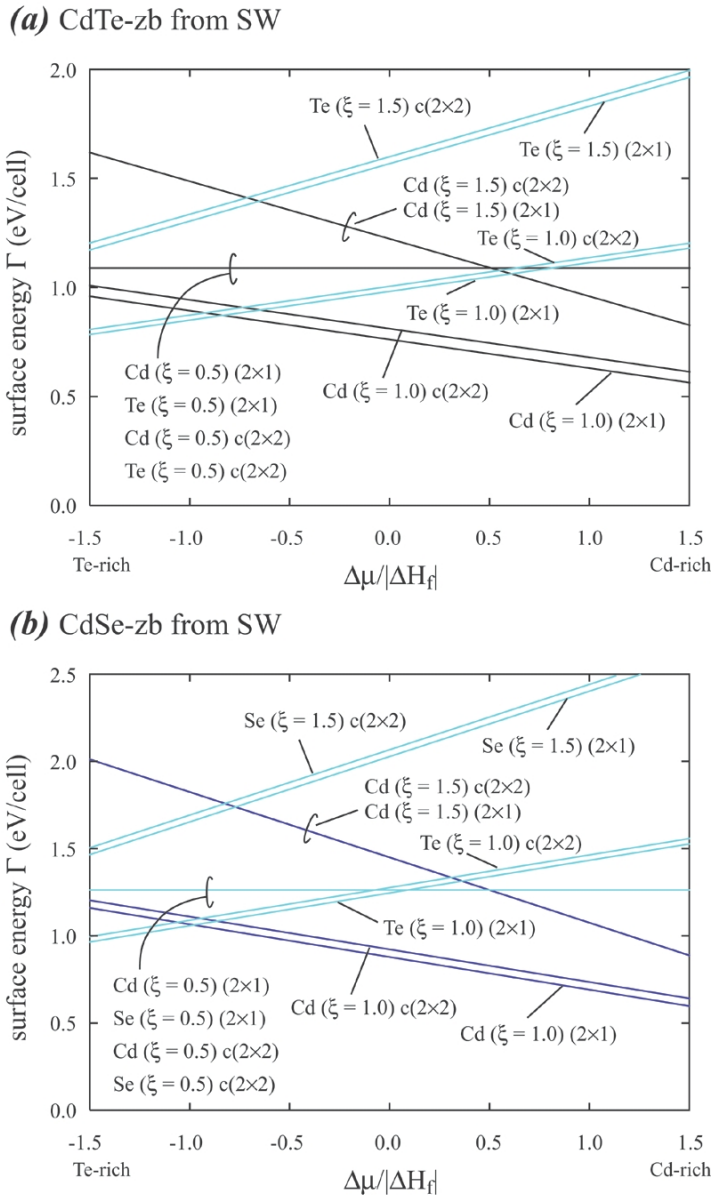

Figure 1-8. Surface energy phase diagrams predicted by the SW potential.

Fig. 1-8(a) and Fig. 1-8(b)… These observations, require that Δμ is strictly constrained between $-\Delta H_f$ and ΔH_f , which is true under experimental equilibrium condition. However, under highly non-equilibrium conditions typically used in MD, the Cd-rich condition may reach $|\Delta\mu| >> |\Delta H_f|$. Then the DFT calculations would predict Cd (1×2) (coverage ξ = 1.0) as the lowest energy surface, in agreement with the BOP. These are strong validation of the BOP, especially considering that even DFT cannot account for the experimentally observed surface reconstructions.

IV.7 Vapor Deposition Simulations

As mentioned above, vapor deposition simulations are extremely important because they test

configurations that cannot be tested otherwise. MD vapor deposition simulations have been performed to confirm that crystalline growth is achieved for Cd-hcp, Te-A8, and CdTe-zb with the present BOP. Detailed results of these simulations will be published separately [39], and hence will not be repeated here. Here we perform further MD vapor deposition simulations to validate Te-A8, $Te_{0.5}Se_{0.5}$-A8 alloy, CdSe-zb, and $CdTe_{0.5}Se_{0.5}$-zb growth. Our computational systems employ periodic boundary conditions in the x and z directions, and a free boundary condition in the y direction. The growth occurs in the +y direction, with a constant zero pressure maintained during simulations to relax the system dimensions.

For Se growth, an initial substrate of an A8 crystal containing 1320 Se atoms with 20 $(2\bar{1}\bar{1}0)$ layers in the x direction, 11 (0003) layers in the y direction, and 12 $(0\bar{1}10)$ layers in the z direction is used, where layers refer to crystallographic planes so that one (0001) layer is equivalent n (000n) layers etc. The substrate temperature is set at T = 300 K by assigning velocities to atoms according to the Boltzmann distribution. During simulations, the bottom (-y) 3 (0003) layers are held fixed to prevent crystal shift upon adatom impact on the top surface. The next 4 (0003) layers are isothermally controlled at the substrate temperature. This leaves the top 4 layers free where the motion of atoms is solely determined by Newton's law. Injection of Se adatoms from random locations far above the surface simulates the growth. All adatoms have an initial far-field incident kinetic energy E_i = 0.1 eV and an incident angle $\theta = 0^o$ (i.e., the moving direction is perpendicular to the surface). The adatom injection frequency is chosen to give a deposition rate of R = 3.2 nm/ns. To approximately maintain a constant thickness of the free surface region, the isothermal region expands upward during simulations. Since surface roughness might develop, the isothermal region expands at about 80% of the surface growth rate so that the upper boundary of the isothermal region never exceeds the surface even at the valley locations. Fig. 1-9 depicts the resulting configuration obtained after 0.42 ns deposition. Note that in Figs. 1-9 to 1-12, the original substrate is shaded in yellow. Fig. 1-9 shows that the BOP correctly captures the crystalline growth of the Se.

For $Te_{0.5}Se_{0.5}$ growth we create an initial substrate of an A8 $Te_{0.25}Se_{0.75}$ alloyed crystal containing 200 Te atoms and 600 Se atoms with 20 $(2\bar{1}\bar{1}0)$ layers in the x direction, 10 (0003) layers in the y direction, and 8 $(0\bar{1}10)$ layers in the z direction. This vapor deposition simulation utilizes the same approach as described above at a substrate temperature T = 300 K, an incident energy E_i = 0.1 eV, an incident angle $\theta = 0^o$, a deposition rate R = 2.5 nm/ns, and a vapor flux ratio Te:Se = 1:1 (while randomly chosen, the adatom species will eventually average to approximately 50% Te and 50% Se). Fig. 1-10 shows the resulting configuration obtained after 1.20 ns deposition. It can be seen that the BOP predicts an A8 crystalline growth of the $Te_{0.50}Se_{0.50}$ alloyed film on a $Te_{0.25}Se_{0.75}$ substrate with a different composition. Experimentally, Te and Se form a continuous solid solution with the A8 crystal structure over the entire composition range [13]. This means that the alloyed $Te_{0.50}Se_{0.50}$ A8 crystal is thermodynamically stable. The prediction of the crystalline growth of the $Te_{0.50}Se_{0.50}$ A8 crystal during direct MD simulations strongly validates that our BOP captures correctly the thermodynamic behavior of the Te-Se system.

[39] D. K. Ward, (2013).

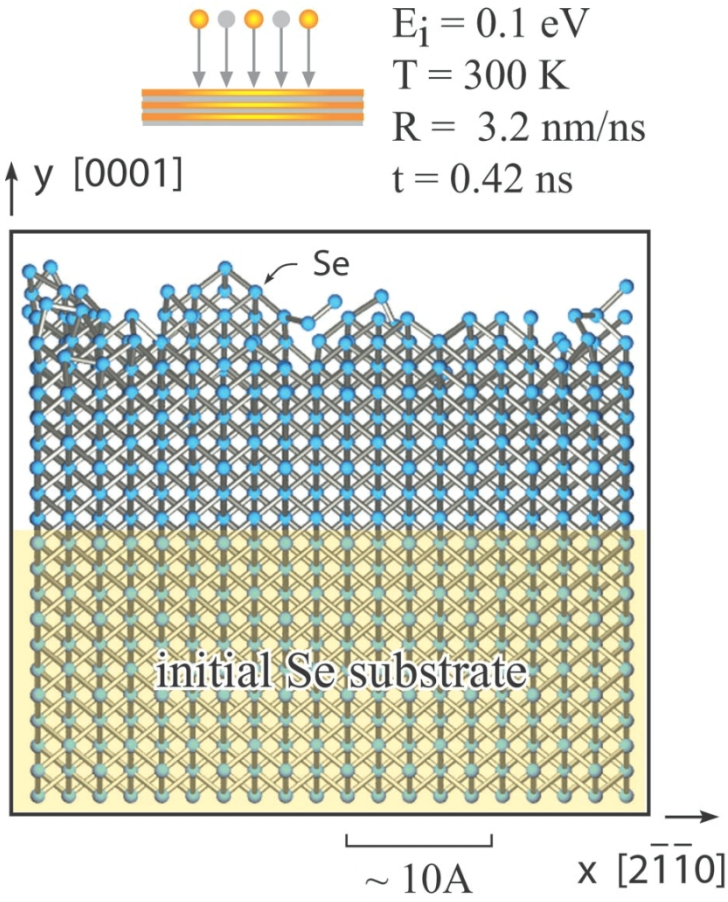

Figure 1-9. BOP prediction of the Se-A8 structure deposited in the [0001] direction (initial substrate is shaded in yellow).

For CdSe growth, an initial substrate of a zb CdSe crystal containing 648 Cd atoms and 648 Se atoms with 18 (101) layers in the x direction, 12 (040) layers in the y direction, and 6 ($\bar{1}$01) layers in the z direction is used. Initially, Cd terminates the top y surface. During simulations, the bottom 3 (040) layers are held fixed. To mimic the molecular beam epitaxy (MBE) growth condition commonly used for semiconductor growth, we expanded the isothermal region to include all atoms above the fixed region. To capture the adatom incident energy effects, however, the simulation does not isothermally control the newly added adatoms until they fully incorporate into the film and their initial kinetic and potential (latent heat release) energies fully dissipate. The growth simulation, has a substrate temperature T = 1200 K, an incident energy E_i = 0.1 eV, an incident angle $\theta = 0^o$, a deposition rate R = 2.8 nm/ns, and a stoichiometric vapor flux ratio Cd:Se = 1:1. Fig. 1-11 depicts the system configuration obtained at 1.2 ns deposition time. It is seen again that our BOP correctly captures the crystalline growth of the equilibrium CdSe-zb crystal.

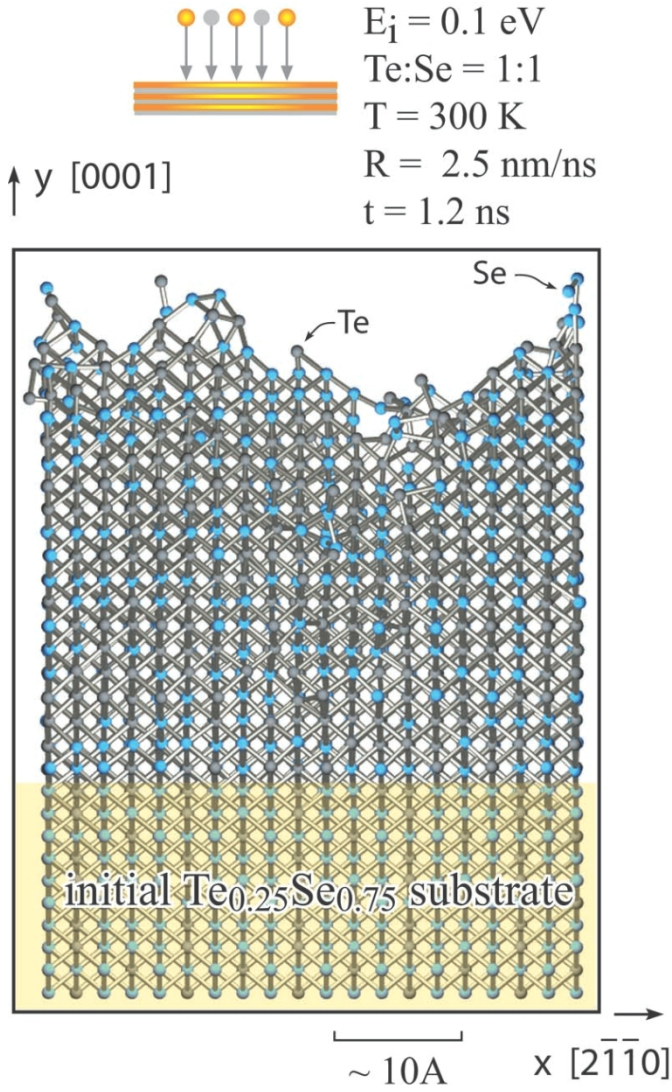

Figure 1-10. BOP prediction of the $Te_{0.50}Se_{0.50}$-A8 structure deposited in the [0001] direction (initial substrate is shaded in yellow).

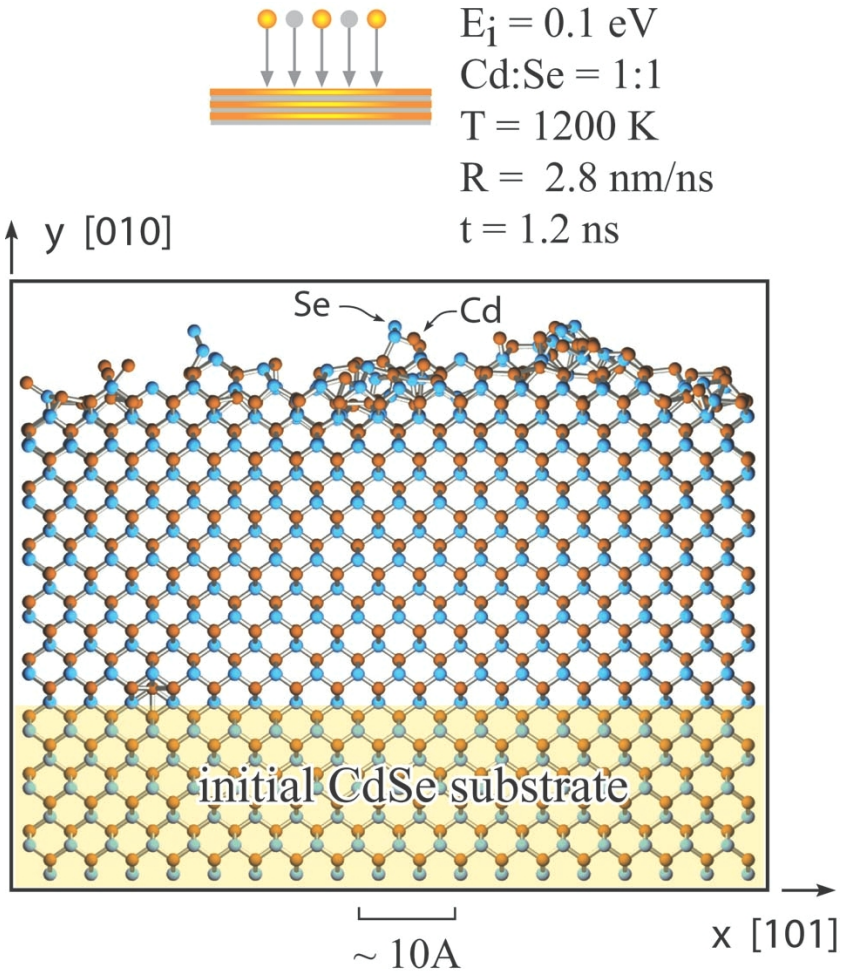

Figure 1-11. BOP prediction of the CdSe-zb structure deposited in the [010] direction (initial substrate is shaded in yellow).

For $CdTe_{0.5}Se_{0.5}$ growth, we begin with a zb CdTe substrate containing 648 Cd atoms and 648 Te atoms with 18 (101) layers in the x direction, 12 (040) layers in the y direction, and 6 ($\bar{1}01$) layers in the z direction. Initially, Te atoms terminated the surface. Following the same approach used for CdSe, the $CdTe_{0.5}Se_{0.5}$ growth is simulated at a substrate temperature T = 1200 K, an incident energy E_i = 0.1 eV, an incident angle $\theta = 0^o$, a deposition rate R = 2.5 nm/ns, and a vapor flux ratio Cd:Te:Se = 2:1:1. Fig. 1-12 shows the configuration obtained at 1.2 ns deposition time. It again validates that our BOP correctly captures the crystalline growth of the ternary zb $CdTe_{0.5}Se_{0.5}$ compound commonly achieved in experiments. Note that here we actually simulate a more complicated $CdTe_{0.5}Se_{0.5}$/CdTe multilayer growth.

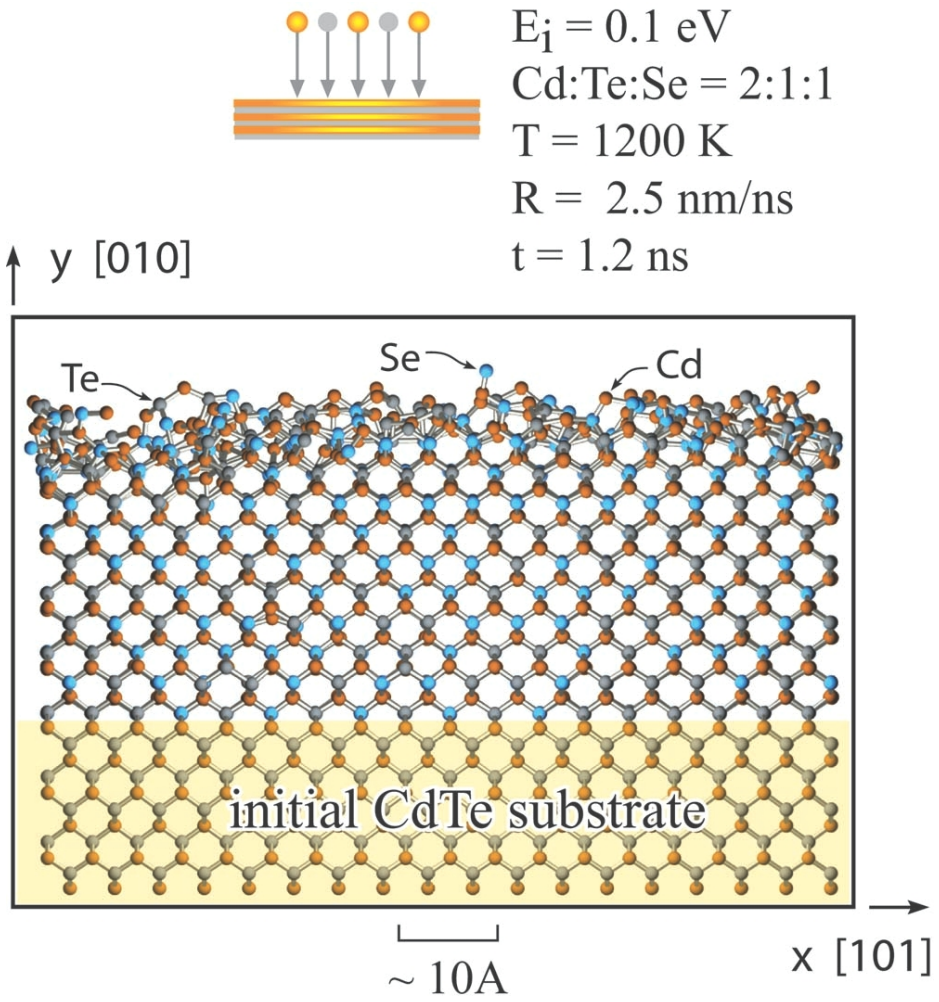

Figure 1-12. BOP prediction of the $CdTe_{0.5}Se_{0.5}$-zb structure deposited in the [010] direction (initial substrate is shaded in yellow).

The past successful MD simulations of crystalline growth of equilibrium semiconductor crystals are achieved primarily using SW potentials. The problem is that SW potentials only stabilize the tetrahedral structure without capturing the property trends of other configurations, and as a result they prediction of defect information is relatively inaccurate. Without including growth simulation tests in parameterizations, many literature Tersoff potentials do not predict crystalline growth [2,24,40]. This work develops Cd-Te-Se ternary BOP that is fundamentally more transferrable than Tersoff potentials. More importantly, a significantly iterative parameterization scheme is strictly followed to capture property trends of a variety of phases and crystalline growth of the equilibrium phases under a variety of chemical conditions. It is the improved property trends and crystalline simulation capability that enable our Cd-Te-Se BOP to be confidently applied for nano material problems.

[40] M. Nakamura, H. Fujioka, K. Ono, M. Takeuchi, T. Mitsui, and M. Oshima, J. Cryst. Growth, 209, 232 (2000).

V. CONCLUSIONS

We have developed a high-fidelity bond-order potential for the Cd-Te-Se ternary system. Unlike many other existing semiconductor potentials, this BOP is derived directly from quantum-mechanical theories and hence is fundamentally transferrable to environments that are not explicitly tested. In particular, it simultaneously meets two stringent criteria: (a) it accurately captures property trends of many configurations including defects and surfaces; and more importantly (b) it results in crystalline growth in MD vapor deposition simulations under a variety of chemical conditions. We achieved high quality parameterization by considering a large number of target structures with coordination ranging from 2 to 12; setting physically valid bounds for all parameters; applying the two-step fitting approach; using different minimization schemes; and iterating the parameterization with crystalline growth simulation tests.

The BOP approach will enable empirical MD simulations of semiconductors to achieve a new fidelity level approaching significantly toward the quantum-mechanical methods. As a demonstration in a ternary system, our Cd-Te-Se BOP enables accurate study of CdTe/CdSe core/shell structures. Equally important, our work builds a foundation for the expansion of BOP into other semiconductor compound systems. Currently, this type of BOP is only applied to GaAs [41] and CdZnTe [5,6] primarily due to the difficulties in BOP parameterization.

APPENDICES

APPENDIX 1-A Target Structures

To develop complex potentials such as the BOP, it is mandatory to use a larger number of carefully selected target lattices to remove all degrees of freedom of the parameters in a physically meaningful way. The target structures listed here were determined through extensive trials. Not all the structures are necessarily used in the fitting, but they must all be monitored in the iterative parameterization process to ensure the lowest energy for the equilibrium phases. The target clusters include dimer (di), trimer (tri), square (sq), rhombus (rhom), tetrahedron (tetra), and four-atom-chain (ch) for each of the six elemental and binary systems (Cd, Te, Se, Cd-Te, Cd-Se, and Te-Se). Note that in the binary systems studied here, the ratio of the two species necessarily does not equal 1:1 for trimers (e.g., Cd_2Te, $CdTe_2$, Cd_2Se, $CdSe_2$, etc.) but is assumed to be 1:1 for all other clusters. The target lattices for the three elemental systems (Cd, Te, Se) include diamond-cubic (dc), simple-cubic (sc), body-centered-cubic (bcc), face-centered-cubic (fcc), hexagonal-close-packed (hcp), graphene (grap), graphite (gra), face-centered-square (fcs), and γ-Se (A8) phases. Here the face-centered-square is essentially one sheet of a (100) fcc plane. The target lattices for the two intermetallic binary systems with a species ratio of 1:1 (i.e., CdTe, CdSe) include zinc-blende (zb), wurtzite (wz), NaCl (B1), CsCl (B2), binary-graphene (bgrap), binary-graphite (bgra), binary-face-centered-square (bfcs), AuCu ($L1_0$), CuPt ($L1_1$), NiAs ($B8_1$), CrB (B33), and AlSb (sc16). Here the binary-graphene is essentially a graphene sheet with neighboring atoms alternating between the two species, and binary-graphite is essentially a stack of binary-graphene sheets. The target lattices for the four intermetallic binary systems with an unequal species ratio (namely, Cd_2Te, $CdTe_2$, Cd_2Se, $CdSe_2$) include Ag_2O (cP4), and ZrO_2. The same target lattices for the intermetallic binary systems are also used for TeSe, Te_2Se, $TeSe_2$ despite that Te-Se only forms a continuous solid solution with Te and Se atoms populated in an A8 lattice [13]. To best capture this solid solution behavior, we also include two additional A8 target lattices corresponding respectively to $Te_{0.25}Se_{0.75}$ and $Te_{0.75}Se_{0.25}$ solid solutions (with Te and Se atoms fully mixed and atom environment highly symmetric). The target lattices for the ternary system include alloyed zinc-blende compounds $CdTe_{0.25}Se_{0.75}$, $CdTe_{0.50}Se_{0.50}$, and $CdTe_{0.75}Se_{0.25}$. The target defect structures include zinc-blende CdTe and CdSe with various vacancies, antisites, interstitials, and surfaces, which are described in more details in sections IV.E and IV.F.

APPENDIX 1-B Parameter Bounds

Constraining the parameters within physical ranges is necessary for BOP parameterization. Table 1-B-1 lists these constraints in seven groups representing parameterizations of Cd, Te, Se, Cd-Te, Cd-Se, Te-Se, and Cd-Te-Se systems, respectively.

Table 1-B-1. Bounds on BOP parameters.

Elemental Cd
$1.0 < 2.1 \cdot n_{CdCd} < m_{CdCd} < 2.2 \cdot n_{CdCd} < 4$
$n_{c,CdCd} \le 2.8$
$n_{CdCd} > \frac{\ln(\xi)}{\ln\left[\exp\left(1 - 1^{\,n_{c,CdCd}}\right)/1\right]}, \xi = 0.02, 1 = 1.5$
$0.42 \le p_{\pi,Cd} \le 1$
$\beta^2_{\pi,0,CdCd} \le p_{\pi,Cd} \cdot \beta^2_{\sigma,0,CdCd}$
$0 \le \beta_{\sigma,0,CdCd} \le 8$
$0 \le \beta_{\pi,0,CdCd} \le 8$
$0 \le c_{\sigma,CdCd} \le 3.65$
$0.2 \le f_{\sigma,CdCd} \le 0.8$
$-15 \le k_{\sigma,CdCd} \le 15$
$0 \le b_{\sigma,CdCdCd} \le 1$
$-0.4 \le u_{\sigma,CdCdCd} \le 0.2$
$\left(b_{\sigma,CdCdCd} + p_{\sigma,CdCdCd}\right)^2 \left(u^2_{\sigma,CdCdCd} - 1\right)^2 > 4\left[p_{\sigma,CdCdCd} - b_{\sigma,CdCdCd} + \left(p_{\sigma,CdCdCd} + b_{\sigma,CdCdCd}\right) u_{\sigma,CdCdCd}\right]^2$
Elemental Te
$0.8 < 1.99 \cdot n_{TeTe} < m_{TeTe} < 2.01 \cdot n_{TeTe} < 4$
$n_{c,TeTe} = 2.799998$
$n_{TeTe} > \frac{\ln(\xi)}{\ln\left[\exp\left(1 - 1^{\,n_{c,TeTe}}\right)/1\right]}, \xi = 0.05, 1 = 1.5$
$0.42 \le p_{\pi,Te} \le 1$
$\beta^2_{\pi,0,TeTe} \le p_{\pi,Te} \cdot \beta^2_{\sigma,0,TeTe}$
$0 \le \beta_{\sigma,0,TeTe} \le 8$
$0 \le \beta_{\pi,0,TeTe} \le 8$

$0 \le c_{\sigma,TeTe} \le 3.65$
$0.2 \le f_{\sigma,TeTe} \le 0.8$
$-15 \le k_{\sigma,TeTe} \le 15$
$0 \le b_{\sigma,TeTeTe} \le 1$
$-0.4 \le u_{\sigma,TeTeTe} \le 0.2$
$\left(b_{\sigma,TeTeTe} + p_{\sigma,TeTeTe}\right)^2 \left(u_{\sigma,TeTeTe}^2 - 1\right)^2 > 4\left[p_{\sigma,TeTeTe} - b_{\sigma,TeTeTe} + \left(p_{\sigma,TeTeTe} + b_{\sigma,TeTeTe}\right)u_{\sigma,TeTeTe}\right]^2$
Elemental Se
$0.8 < 1.99 \cdot n_{SeSe} < m_{SeSe} < 2.01 \cdot n_{SeSe} < 4$
$n_{c,SeSe} = 2.799998$
$n_{SeSe} > \frac{\ln(\xi)}{\ln\left[\exp\left(1 - l^{\,n_{c,SeSe}}\right)/l\right]}, \xi = 0.05, l = 1.5$
$0.42 \le p_{\pi,Se} \le 1$
$\beta_{\pi,0,SeSe}^2 \le p_{\pi,Se} \cdot \beta_{\sigma,0,SeSe}^2$
$0 \le \beta_{\sigma,0,SeSe} \le 8$
$0 \le \beta_{\pi,0,SeSe} \le 8$
$0 \le c_{\sigma,SeSe} \le 3.65$
$0.2 \le f_{\sigma,SeSe} \le 0.8$
$-15 \le k_{\sigma,SeSe} \le 15$
$0 \le b_{\sigma,SeSeSe} \le 1$
$-0.4 \le u_{\sigma,SeSeSe} \le 0.0$
$\left(b_{\sigma,SeSeSe} + p_{\sigma,SeSeSe}\right)^2 \left(u_{\sigma,SeSeSe}^2 - 1\right)^2 > 4\left[p_{\sigma,SeSeSe} - b_{\sigma,SeSeSe} + \left(p_{\sigma,SeSeSe} + b_{\sigma,SeSeSe}\right)u_{\sigma,SeSeSe}\right]^2$
Binary Cd-Te
$0.1 < 1.99 \cdot n_{CdTe} < m_{CdTe} < 2.01 \cdot n_{CdTe} < 4$
$n_{c,CdTe} = 2.811251$
$n_{CdTe} > \frac{\ln(\xi)}{\ln\left[\exp\left(1 - l^{\,n_{c,CdTe}}\right)/l\right]}, \xi = 0.05, l = 1.5$
$\beta_{\pi,0,CdTe}^2 \le p_{\pi,Cd} \cdot \beta_{\sigma,0,CdTe}^2$
$\beta_{\pi,0,CdTe}^2 \le p_{\pi,Te} \cdot \beta_{\sigma,0,CdTe}^2$
$0 \le \beta_{\sigma,0,CdTe} \le 2$
$0 \le \beta_{\pi,0,CdTe} \le 1$
$0.8 \le c_{\sigma,CdTe} \le 3.65$
$f_{\sigma,CdTe} = 0.5$
$k_{\sigma,CdTe} = 0.0$
$0.2 \le b_{\sigma,CdCdTe} \le 1$
$-0.4 \le u_{\sigma,CdCdTe} \le 0.1$

$(b_{\sigma,CdCdTe} + p_{\sigma,CdCdTe})^2 (u_{\sigma,CdCdTe}^2 - 1)^2 \geq 4[p_{\sigma,CdCdTe} - b_{\sigma,CdCdTe} + (p_{\sigma,CdCdTe} + b_{\sigma,CdCdTe}) u_{\sigma,CdCdTe}]^2$
$0.2 \leq b_{\sigma,TeCdTe} \leq 1$
$-0.4 \leq u_{\sigma,TeCdTe} \leq 0.1$
$(b_{\sigma,TeCdTe} + p_{\sigma,TeCdTe})^2 (u_{\sigma,TeCdTe}^2 - 1)^2 \geq 4[p_{\sigma,TeCdTe} - b_{\sigma,TeCdTe} + (p_{\sigma,TeCdTe} + b_{\sigma,TeCdTe}) u_{\sigma,TeCdTe}]^2$
$0.2 \leq b_{\sigma,CdTeCd} \leq 1$
$-0.4 \leq u_{\sigma,CdTeCd} \leq 0.1$
$(b_{\sigma,CdTeCd} + p_{\sigma,CdTeCd})^2 (u_{\sigma,CdTeCd}^2 - 1)^2 \geq 4[p_{\sigma,CdTeCd} - b_{\sigma,CdTeCd} + (p_{\sigma,CdTeCd} + b_{\sigma,CdTeCd}) u_{\sigma,CdTeCd}]^2$
$0.2 \leq b_{\sigma,CdTeTe} \leq 1$
$-0.4 \leq u_{\sigma,CdTeTe} \leq 0.1$
$(b_{\sigma,CdTeTe} + p_{\sigma,CdTeTe})^2 (u_{\sigma,CdTeTe}^2 - 1)^2 \geq 4[p_{\sigma,CdTeTe} - b_{\sigma,CdTeTe} + (p_{\sigma,CdTeTe} + b_{\sigma,CdTeTe}) u_{\sigma,CdTeTe}]^2$
Binary Cd-Se
$0.1 < 1.9 \cdot n_{CdSe} < m_{CdSe} < 2.1 \cdot n_{CdSe} < 4$
$0 < n_{c,CdSe} < 5.0$
$n_{CdSe} > \frac{\ln(\xi)}{\ln[\exp(1 - 1^{n_{c,CdSe}})/1]}, \xi = 0.05, 1 = 1.5$
$\beta_{\pi,0,CdSe}^2 \leq p_{\pi,Cd} \cdot \beta_{\sigma,0,CdSe}^2$
$\beta_{\pi,0,CdSe}^2 \leq p_{\pi,Se} \cdot \beta_{\sigma,0,CdSe}^2$
$0 \leq \beta_{\sigma,0,CdSe} \leq 2$
$0 \leq \beta_{\pi,0,CdSe} \leq 1$
$0.3 \leq c_{\sigma,CdSe} \leq 3.65$
$f_{\sigma,CdSe} = 0.5$
$k_{\sigma,CdSe} = 0.0$
$0.1 \leq b_{\sigma,CdCdSe} \leq 0.6$
$-0.38 \leq u_{\sigma,CdCdSe} \leq 0.0$
$(b_{\sigma,CdCdSe} + g_{0,CdCdSe})^2 (u_{\sigma,CdCdSe}^2 - 1)^2 \geq 4[g_{0,CdCdSe} - b_{\sigma,CdCdSe} + (g_{0,CdCdSe} + b_{\sigma,CdCdSe}) u_{\sigma,CdCdSe}]^2$
$0.2 \leq b_{\sigma,SeCdSe} \leq 0.6$
$-0.35 \leq u_{\sigma,SeCdSe} \leq 0.0$
$(b_{\sigma,SeCdSe} + g_{0,SeCdSe})^2 (u_{\sigma,SeCdSe}^2 - 1)^2 \geq 4[g_{0,SeCdSe} - b_{\sigma,SeCdSe} + (g_{0,SeCdSe} + b_{\sigma,SeCdSe}) u_{\sigma,SeCdSe}]^2$
$0.3 \leq b_{\sigma,CdSeCd} \leq 0.6$
$-0.35 \leq u_{\sigma,CdSeCd} \leq 0.0$
$(b_{\sigma,CdSeCd} + g_{0,CdSeCd})^2 (u_{\sigma,CdSeCd}^2 - 1)^2 \geq 4[g_{0,CdSeCd} - b_{\sigma,CdSeCd} + (g_{0,CdSeCd} + b_{\sigma,CdSeCd}) u_{\sigma,CdSeCd}]^2$
$0.2 \leq b_{\sigma,CdSeSe} \leq 0.6$
$-0.35 \leq u_{\sigma,CdSeSe} \leq 0.0$

$\left(b_{\sigma,CdSeSe}+g_{0,CdSeSe}\right)^2\left(u_{\sigma,CdSeSe}^2-1\right)^2 \geq 4\left[g_{0,CdSeSe}-b_{\sigma,CdSeSe}+\left(g_{0,CdSeSe}+b_{\sigma,CdSeSe}\right)u_{\sigma,CdSeSe}\right]^2$
Binary Te-Se
$0.1<1.90\cdot n_{TeSe}<m_{TeSe}<2.10\cdot n_{TeSe}<4$
$0<n_{c,TeSe}<5.0$
$n_{TeSe}>\frac{\ln(\xi)}{\ln\left[\exp\left(1-1^{n_{c,TeSe}}\right)/1\right]},\xi=0.05,1=1.5$
$\beta_{\pi,0,TeSe}^2 \leq p_{\pi,Te}\cdot\beta_{\sigma,0,TeSe}^2$
$\beta_{\pi,0,TeSe}^2 \leq p_{\pi,Se}\cdot\beta_{\sigma,0,TeSe}^2$
$0\leq\beta_{\sigma,0,TeSe}\leq 2$
$0\leq\beta_{\pi,0,TeSe}\leq 1$
$0.3\leq c_{\sigma,TeSe}\leq 3.65$
$0\leq f_{\sigma,TeSe}\leq 1$
$-20\leq k_{\sigma,TeSe}\leq 20$
$0.1\leq b_{\sigma,TeTeSe}\leq 0.6$
$-0.38\leq u_{\sigma,TeTeSe}\leq 0.0$
$\left(b_{\sigma,TeTeSe}+g_{0,TeTeSe}\right)^2\left(u_{\sigma,TeTeSe}^2-1\right)^2 \geq 4\left[g_{0,TeTeSe}-b_{\sigma,TeTeSe}+\left(g_{0,TeTeSe}+b_{\sigma,TeTeSe}\right)u_{\sigma,TeTeSe}\right]^2$
$0.1\leq b_{\sigma,SeTeSe}\leq 0.6$
$-0.38\leq u_{\sigma,SeTeSe}\leq 0.0$
$\left(b_{\sigma,SeTeSe}+g_{0,SeTeSe}\right)^2\left(u_{\sigma,SeTeSe}^2-1\right)^2 \geq 4\left[g_{0,SeTeSe}-b_{\sigma,SeTeSe}+\left(g_{0,SeTeSe}+b_{\sigma,SeTeSe}\right)u_{\sigma,SeTeSe}\right]^2$
$0.1\leq b_{\sigma,TeSeTe}\leq 0.6$
$-0.38\leq u_{\sigma,TeSeTe}\leq 0.0$
$\left(b_{\sigma,TeSeTe}+g_{0,TeSeTe}\right)^2\left(u_{\sigma,TeSeTe}^2-1\right)^2 \geq 4\left[g_{0,TeSeTe}-b_{\sigma,TeSeTe}+\left(g_{0,TeSeTe}+b_{\sigma,TeSeTe}\right)u_{\sigma,TeSeTe}\right]^2$
$0.1\leq b_{\sigma,TeSeSe}\leq 0.6$
$-0.38\leq u_{\sigma,TeSeSe}\leq 0.0$
$\left(b_{\sigma,TeSeSe}+g_{0,TeSeSe}\right)^2\left(u_{\sigma,TeSeSe}^2-1\right)^2 \geq 4\left[g_{0,TeSeSe}-b_{\sigma,TeSeSe}+\left(g_{0,TeSeSe}+b_{\sigma,TeSeSe}\right)u_{\sigma,TeSeSe}\right]^2$
Ternary Cd-Te-Se
$0.2\leq b_{\sigma,TeCdSe}\leq 1$
$-0.4\leq u_{\sigma,TeCdSe}\leq 0.1$
$\left(b_{\sigma,TeCdSe}+g_{0,TeCdSe}\right)^2\left(u_{\sigma,TeCdSe}^2-1\right)^2 \geq 4\left[g_{0,TeCdSe}-b_{\sigma,TeCdSe}+\left(g_{0,TeCdSe}+b_{\sigma,TeCdSe}\right)u_{\sigma,TeCdSe}\right]^2$
$0.2\leq b_{\sigma,CdTeSe}\leq 1$
$-0.4\leq u_{\sigma,CdTeSe}\leq 0.1$

$(b_{\sigma,CdTeSe}+g_{0,CdTeSe})^2(u_{\sigma,CdTeSe}^2-1)^2 \geq 4[g_{0,CdTeSe}-b_{\sigma,CdTeSe}+(g_{0,CdTeSe}+b_{\sigma,CdTeSe})u_{\sigma,CdTeSe}]^2$
$0.2 \leq b_{\sigma,CdSeTe} \leq 1$
$-0.4 \leq u_{\sigma,CdSeTe} \leq 0.1$
$(b_{\sigma,CdSeTe}+g_{0,CdSeTe})^2(u_{\sigma,CdSeTe}^2-1)^2 \geq 4[g_{0,CdSeTe}-b_{\sigma,CdSeTe}+(g_{0,CdSeTe}+b_{\sigma,CdSeTe})u_{\sigma,CdSeTe}]^2$

APPENDIX 1-C Complete List of Predicted Properties

Table 1-C-1. Cohesive energies E_c (eV/atom), bond length r (Å), and bond angle θ (deg.) for selected Cd, Te, Se, CdTe, CdSe, and TeSe clusters as determined from various models.

Cluster Type	SW [4]			BOP			DFT		
	E_c	r	θ	E_c	r	θ	E_c	r	θ
CdCd-di	-0.219	2.870	-----	-0.356	2.751	-----	-0.089	3.456	-----
CdCdCd-tri[a]	-0.339	2.983	60	-0.530	2.863	60	-0.183	3.390	60
CdCdCdCd-ch[b]	-0.219	4.616 2.870	-----	-0.381	2.935 2.828	-----	-0.142	3.402 3.426	-----
CdCdCdCd-rec[c]	-0.418	2.891 2.891	-----	-0.469	2.853 2.853	-----	-0.175	3.448 3.437	-----
CdCdCdCd-tetra	-0.419	3.061	-----	-0.633	2.932	-----	-0.295	3.340	-----
TeTe-di	-0.486	3.167	-----	-1.415	2.737	-----	-1.790	2.597	-----
TeTeTe-tri[a]	-0.710	3.340	60	-1.383	3.007	60	-1.969	2.770	60
TeTeTeTe-ch[b]	-0.486	5.095 3.167	-----	-1.417	4.070 2.738	-----	-1.872	3.147 2.602	-----
TeTeTeTe-rec[c]	-0.918	3.199 3.199	-----	-1.539	3.571 2.738	-----	-2.139	3.192 2.585	-----
TeTeTeTe-tetra	-0.846	3.455	-----	-1.345	3.158	-----	unstable	-----	-----
SeSe-di	-0.482	3.019	-----	-1.637	2.435	-----	-1.935	2.196	-----
SeSeSe-tri[a]	-0.737	3.148	60	-1.461	2.750	60	-2.171	2.379	60
SeSeSeSe-ch[b]	-0.482	4.857 3.019	-----	-1.637	4.487 2.435	-----	-2.124	3.530 2.195	-----
SeSeSeSe-rec[c]	-0.919	3.043 3.043	-----	-1.766	3.368 2.435	-----	-2.409	2.827 2.188	-----
SeSeSeSe-tetra	-0.904	3.235	-----	-1.423	2.905	-----	unstable	-----	-----
CdTe-di	-0.545	2.805	-----	-0.588	2.771	-----	-0.519	2.613	-----
CdTeCd-tri[a]	-0.726	2.805	109.5	-0.733	2.795	113.8	-0.561	2.809	76.4
CdSe-di	-0.631	2.620	-----	-0.951	2.456	-----	-0.573	2.388	-----
CdSeCd-tri[a]	-0.841	2.620	109.5	-0.979	2.552	113.1	-0.666	2.579	85.8
TeSe-di	-0.458	2.711	-----	-1.650	2.386	-----	-1.878	2.394	-----

[a]: For ABA trimer clusters, the bond length is between atoms A and B, and the bond angle centers at B.

[b]: For ABCD chain clusters, the first bond length is between the two middle atoms B and C, and the second bond length is between the two outer atoms A and B or C and D.

[c]: For rectangular clusters, the bigger and smaller bond lengths refer respectively to the longer and shorter edges. Equal bond lengths mean square clusters.

Table 1-C-2. Cohesive energies E_c (eV/atom), lattice constants a, b, c (Å) for selected Cd, Te, Se, CdTe, CdSe, TeSe, and CdTeSe lattices as determined from various models.

Structure	SW [4]		BOP		DFT		Exp.	
	E_c	a-c[a]	E_c	a-c[a]	E_c	a-c[a]	E_c [32]	a-c[a] [42]
Cd-grap	-0.642	4.989	-0.599	5.098	-0.340	5.314	-----	-----
Cd-dc	-0.876	6.627	-0.725	6.871	-0.679	6.595	-----	-----
Cd-gra	-0.780	5.016 6.016	-0.671	5.053 5.793	-0.946	4.887 5.308	-----	-----
Cd-sc	-0.958	3.008	-0.618	3.120	-1.086	2.959	-----	-----
Cd-bcc	-1.075	3.559	-1.019	3.539	-1.351	3.613	-----	-----
Cd-hcp	-1.133	3.195 5.217	-1.135	3.152 5.124	-1.398	3.122 5.585	-1.133	2.974 5.606
Cd-fcc	-1.133	4.518	-1.128	4.452	-1.402	4.605	-----	-----
Te-grap	-1.417	5.514	-1.697	5.334	-2.122	5.314	-----	-----
Te-dc	-1.945	7.314	-1.943	7.234	-2.272	7.123	-----	-----
Te-gra	-1.689	5.553 6.763	-1.873	5.384 6.652	-2.468	5.210 6.063	-----	-----
Te-sc	-1.983	3.377	-2.163	3.232	-2.765	3.174	-----	-----
Te-bcc	-2.131	4.040	-1.941	3.930	-2.551	3.868	-----	-----
Te-hcp	-2.169	3.636 5.937	unstable	-----	-----	-----	-----	-----
Te-fcc	-2.169	5.142	-1.846	4.951	-2.399	4.840	-----	-----
Te-A8	-1.983	4.776 5.849	-2.163	4.572 5.590	-2.798	4.340 6.045	-2.169	4.447 5.915
Se-grap	-1.412	5.250	-1.745	4.910	-2.230	4.412	-----	-----
Se-dc	-1.930	6.973	-2.034	6.657	-2.306	6.268	-----	-----
Se-gra	-1.709	5.281 6.353	-1.942	4.956 6.219	-2.442	4.581 5.524	-----	-----
Se-sc	-2.079	3.176	-2.414	2.972	-2.728	2.803	-----	-----
Se-bcc	-2.310	3.766	-1.902	3.689	-2.300	3.435	-----	-----
Se-hcp	-2.414	3.383	unstable	-----	-----	-----	-----	-----

[42] J. D. H. Donnay, and H. M. Ondik, *Crystal data, determinative tables*, 3rd ed., Vol. 2 (inorganic compounds) (U. S. Department of Commerce, National Bureau of Standards, and Joint Committee on Power Diffraction Standards, U.S.A., 1973).

		5.524						
Se-fcc	-2.414	4.784	-1.792	4.645	-2.142	4.319	-----	-----
Se-A8	-2.079	4.491 5.501	-2.414	4.208 5.149	-2.861	4.232 5.113	-2.414	4.355 4.950
$CdTe_2$-Ag_2O	-1.213	6.715	-1.335	6.538	-----	-----	-----	-----
Cd_2Te-Ag_2O	-1.213	6.715	-1.375	6.517	-----	-----	-----	-----
$CdTe_2$- ZrO_2	-1.855	7.453	-1.778	7.113	-----	-----	-----	-----
Cd_2Te-ZrO_2	-1.628	7.214	-1.617	6.959	-----	-----	-----	-----
CdTe-CsCl	-1.776	3.850	-1.664	3.674	-2.006	3.810	-----	-----
CdTe-fcs	-1.357	4.344	-1.639	4.090	-1.807	4.103	-----	-----
CdTe-grap	-1.559	4.904	-1.627	4.851	-1.916	4.753	-----	-----
CdTe-L10	-1.776	5.445 3.850	-1.664	5.198 3.669	-----	-----	-----	-----
CdTe-L11	-1.809	4.433 10.859	-2.055	4.198 10.211	-----	-----	-----	-----
CdTe-NiAs	-1.811	4.444 7.212	-1.964	4.154 7.067	-----	-----	-----	-----
CdTe-CrB	-1.827	4.354 4.671 11.290	-1.853	4.131 4.180 15.390	-----	-----	-----	-----
CdTe-gra	-1.796	4.949 6.832	-2.041	4.990 6.042	-2.162	4.813 6.566	-----	-----
CdTe-NaCl	-1.809	6.269	-2.056	5.928	-2.287	6.041	-----	-----
CdTe-wz	-2.178	4.581 7.480	-2.149	4.585 7.491	-2.279	4.520 7.318	-----	-----
CdTe-zb	-2.178	6.478	-2.149	6.480	-2.331	6.524	-2.178	6.478
$CdSe_2$-Ag_2O	-1.368	6.315	-1.628	6.068	-----	-----	-----	-----
Cd_2Se-Ag_2O	-1.368	6.315	-1.532	6.116	-----	-----	-----	-----
$CdSe_2$- ZrO_2	-1.982	7.022	-1.999	6.662	-----	-----	-----	-----
Cd_2Se-ZrO_2	-1.760	6.925	-2.089	6.519	-----	-----	-----	-----
CdSe-CsCl	-1.878	3.641	-2.108	3.423	-2.139	3.556	-----	-----
CdSe-fcs	-1.471	4.124	-2.015	3.815	-2.051	3.830	-----	-----
CdSe-grap	-1.793	4.588	-2.016	4.487	-2.169	4.435	-----	-----
CdSe-L10	-1.878	5.150 3.641	-2.108	4.866 3.414	-----	-----	-----	-----
CdSe-L11	-1.786	3.463 14.617	-2.463	3.938 9.537	-----	-----	-----	-----
CdSe-NiAs	-1.934	4.175 7.066	-2.372	3.874 6.738	-----	-----	-----	-----
CdSe-CrB	-2.027	4.315	-2.227	3.907	-----	-----	-----	-----

		4.327 10.591		3.854 13.933				
CdSe-gra	-1.793	4.589 8.279	-2.016	4.488 8.421	-2.419	4.504 6.023	-----	-----
CdSe-NaCl	-1.939	5.961	-2.463	5.558	-2.547	5.645	-----	-----
CdSe-wz	-2.523	4.278 6.986	-2.523	4.271 6.975	-2.529	4.212 6.838	-----	-----
CdSe-zb	-2.523	6.050	-2.523	6.044	-2.579	6.108	-2.523	6.050
$TeSe_2$-Ag_2O	-1.028	6.468	-1.728	6.471	-----	-----	-----	-----
Te_2Se-Ag_2O	-1.028	6.468	-1.515	6.596	-----	-----	-----	-----
$TeSe_2$- ZrO_2	-1.727	7.012	-1.926	7.164	-----	-----	-----	-----
Te_2Se-ZrO_2	-1.721	7.253	-1.656	7.353	-----	-----	-----	-----
TeSe-CsCl	-1.695	3.708	-1.691	3.832	-2.481	3.653	-----	-----
TeSe-fcs	-1.180	4.145	-2.111	4.183	-2.530	3.989	-----	-----
TeSe-grap	-1.313	4.736	-1.897	4.870	-2.227	4.766	-----	-----
TeSe-L10	-1.723	4.759 4.721	-1.865	4.313 6.812	-----	-----	-----	-----
TeSe-L11	-1.757	3.498 15.562	-2.340	4.343 10.633	-----	-----	-----	-----
TeSe-NiAs	-1.757	3.498 10.375	-2.148	4.287 7.565	-----	-----	-----	-----
TeSe-gra	-1.599	4.744 6.277	-2.071	4.912 5.971	-2.395	4.970 5.698	-----	-----
TeSe-NaCl	-1.582	5.953	-2.340	6.140	-2.786	5.958	-----	-----
TeSe-wz	-1.830	4.427 7.228	-2.072	4.727 7.715	-2.554	4.624 7.866	-----	-----
TeSe-zb	-1.830	6.260	-2.072	6.681	-2.331	6.665	-----	-----
$Te_{0.75}Se_{0.25}$-A8	-1.538	4.568 5.595	-2.321	4.440 5.435	-----	-----	-----	-----
$Te_{0.25}Se_{0.75}$-A8	-1.755	4.400 5.389	-2.477	4.222 5.171	-----	-----	-----	-----
Cd_4Te_3Se-zb	-2.254	6.371	-2.233	6.371	-----	-----	-----	-----
$Cd_4Te_2Se_2$-zb	-2.335	6.247 6.299	-2.327	6.295 6.214	-----	-----	-----	-----
Cd_4TeSe_3-zb	-2.424	6.158	-2.425	6.155	-----	-----	-----	-----

[a:] One number refers to one lattice constant a, two numbers refer to two lattice constants a and c, three numbers refer to three lattice constants a, b, and c.

Table 1-C-3. Intrinsic defect energy $E_D^{'}$ (eV) obtained from different models for CdTe-zb and CdSe-zb.

Defect C: Cd; A: Te, Se	CdTe-zb			CdSe-zb		
	SW [4]	BOP	DFT	SW [4]	BOP	DFT
V_C	1.86	2.68	2.37	3.16	3.02	
V_A	1.66	1.66	0.95	1.88	1.84	
C_A	1.58	2.19	2.12	2.22	2.81	
A_C	1.87	1.90	3.71	3.11	2.33	
$C_{i,A}$	2.92	2.24	1.40	5.04	1.61	
$A_{i,C}$	4.09	2.91	2.47	5.82	3.78	

CHAPTER 2: THERMODYNAMIC PROPERTIES OF MODEL CDTE/CDSE MIXTURES.

Frank van Swol, Xiaowang W. Zhou, Sivakumar R. Challa[2], James E. Martin

Sandia National Laboratories
P.O. Box 5800 Albuquerque, New Mexico 87185

[2]Chemical and Biological Engineering Department
The University of New Mexico Albuquerque, NM 87131

November 15, 2014

ABSTRACT

We report on the thermodynamic properties of binary compound mixtures of model group II-VI semiconductors. We use the recently introduced Stillinger-Weber hamiltonian to model binary mixtures of CdTe and CdSe. We use molecular dynamics simulations to calculate the volume and enthalpy of mixing as a function of mole fraction. The lattice parameter of the mixture closely follows Vegard's Law: a linear relation. This implies that the excess volume is a cubic function of mole fraction. A connection is made with hard sphere models of mixed fcc and zincblende structures. The potential energy exhibits a positive deviation from ideal soluton behavior; the excess enthalpy is nearly independent of temperatures studied (300K and 533K) and is well described by a simple cubic function of the mole fraction. Using a regular solution approach (combining nonideal behavior for the enthalpy with ideal solution behavior for the entropy of mixing) we arrive at the Gibbs free energy of the mixture. The Gibbs free energy results indicate that the CdTe and CdSe mixtures exhibit phase separation. The upper consolute temperature is found to be 335K. Finally, we provide the surface energy as a function of composition. It roughly follows ideal solution theory, but with a negative deviation (negative excess surface energy). This indicates that alloying increases the stability, even for nano-particles.

ACKNOWLEDGEMENTS

We are grateful to Dr. James E. Miller for bringing reference [4] to our attention and for helpful discussions. This research was supported by the United States Department of Energy, Office of Basic Energy Sciences, Division of Materials Sciences and Engineering and Sandia's LDRD program. Sandia National Laboratories is a multi-program laboratory managed and operated by Sandia Corporation, a wholly owned subsidiary of Lockheed Martin Corporation, for the U.S. Department of Energy's National Nuclear Security Administration under contract DE-AC04-94AL85000.

VI. INTRODUCTION

Ternary systems, such as mixtures of CdTe and CdSe, or $CdTe_{1-x}Se_x$ for short, are commonly used in the semiconductor applications to help modify properties such as the lattice parameter and the size of the band gap. Our motivation for studying the thermodynamic properties of $CdTe_{1-x}Se_x$ stems from our interest in core/shell quantum dots (QD) such as CdTe/CdSe, a nanoparticle consisting of CdTe core surrounded by a shell of CdTe. It is well known that the considerable lattice mismatch (about 6%) between these two binary compounds can lead to defect formation that is believed to negatively impact the QD luminescence efficiency. A potential remedy may be found in alloying the interface (heterojunction) where the two phases meet. Without introducing other cations, one can consider the mixing of Te and Se, i.e., replacing some of the anions inside the CdTe phase with Se anions and vice versa in the CdSe phase. To assess the efficacy of such an alloying strategy one requires the thermodynamic mixing properties. In particular, one needs the lattice parameter, the free energy of mixing, and the surface energy over the entire range of composition.

Although there are some experimental results for the lattice parameter of $CdTe_{1-x}Se_x$, the thermo- dynamic mixing properties are not readily available. It is natural then to use a molecular simulation approach to determine the basic thermodynamic properties of mixtures of binary II-VI compounds such as CdTe and CdSe. To facilitate this program we have recently developed an interaction model approach based on the Stillinger-Weber(SW) potential[1, 2]. This potential includes both two-body and three-body interactions. It is, of course, an empirical potential, originally developed for Si. However, it has been shown to possess a versatile functional form that lends itself to a generalization applicable to compounds as well [2].

In a recent paper we introduced a set of two-body and three-body SW potential parameters for any combination of the major II-VI elements Zn, Cd, Hg, S, Se, and Te [2]. The goal of reference [2] was to enable efficient atomistic simulations of defect mechanisms. The potential's fidelity was achieved by optimizing pertinent model parameters with respect to cohesive energy, lattice constants and bulk moduli of all binary compounds. We showed that our intermolecular potential correctly predicted crystalline growth of all binary compounds during molecular dynamics simulations of vapor deposition. We demonstrated that our potential is applicable to a variety of compound configurations involving all the six elements mentioned. We employed the potential to demonstrate a successful MD simulation of crystalline growth of alloyed compounds $(Cd_{0.28}Zn_{0.68}Hg_{0.04})(Te_{0.20}Se_{0.18}S_{0.62})$ onto a ZnS substrate. In addition, it was demonstrated that we could capture a variety of defects such as misfit dislocations, stacking faults, and sub-grain nucleation during a complex growth simulation of ZnS/CdSe/HgTe multilayers that contained all the six elements listed above.

We report on a modeling study of the mixing properties of $CdTe_{1-x}Se_x$. As a function of composition, x, we determine the lattice parameter, volume per particle, and the potential energy (enthalpy), Gibbs free energy as well as the surface energy. We compare the lattice parameter results with Vegard's Law, and make the connection with ideal solution theory.

Table 2-1. The Stillinger-Weber potential parameters for the ternary $CdTe_{1-x}Se_x$.. See Zhou et al. [2]. Also, $Cos\theta_0 = 1/3, p = 4$ and $q = 0$.

	E[eV]	σ[A]	a	λ[eV]	γ	A	B
Cd-Cd	1.182358	2.663951	1.527956	32.5	1.2	7.9170	0.767446
Cd-Te	1.385284	2.352141	1.810919	32.5	1.2	7.0496	0.886125
Cd-Se	1.352371	2.045165	1.953387	32.5	1.2	7.0496	1.116149
Te-Te	1.849775	2.905254	1.594353	32.5	1.2	7.9170	0.73072
Te-Se	1.295053	2.231716	1.809645	32.5	1.2	7.0496	1.005396
Se-Se	2.400781	2.789002	1.544925	32.5	1.2	7.9170	0.76721

VII. SIMULATION METHODS

We use molecular dynamics simulations to study the thermodynamic properties of binary mixtures. The natural choice is to perform these simulations at constant pressure, p, as this corresponds to the typical experimental conditions under which mixtures are most easily studied. Thus, we employ the constant pressure, constant temperature ensemble (i.e. NpT), which we simulate using the standard Nose-Hoover algorithm [3]. We use a cubic simulation cell with periodic boundary conditions (pbc) applied in all three directions. Most simulations were performed with N=1728 atoms (Cd, Te, and Se) arranged in the cubic zincblende structure, which corresponds to $6 \times 6 \times 6 = 216$ cubic unit cells of 8 atoms (4 cations, 4 anions) each. Typically simulations started by generating a pure sample of either CdTe or CdSe. From these samples configurations of $CdTe_{1-x}Se_x$ mixtures were generated by changing the identity of the anions randomly or otherwise. All systems were equilibrated over at least 20,000 time steps of 1.32×10^{-15}s. Averages were taken over runs of 20,000- 40,000 time steps.

To simulate group II-VI semiconductors, we employ the Stillinger-Weber hamiltonian to represent the atomic interactions [1]. This is a versatile functional form, originally developed for Si, that includes both pair and three-body interactions, viz.,

$$\begin{aligned} V &= \sum_{i<j} v_2(r_{ij}) + \sum_{i<j<k} v_3(\mathbf{r}_i, \mathbf{r}_j, \mathbf{r}_k) \\ &= \sum_{i<j} v_2(r_{ij}) + \sum_{i<j<k} h_{jik} + h_{ijk} + h_{ikj} \end{aligned} \tag{1}$$

and h_{jik} is shorthand for the energy contribution associated with angle θ_{jik},

$$h(r_{ij}, r_{iik}, \theta_{jik}) = \lambda g(r_{ij}) g(r_{ik}) (\cos\theta_{jik} - \cos\theta_0)^2 \tag{2}$$

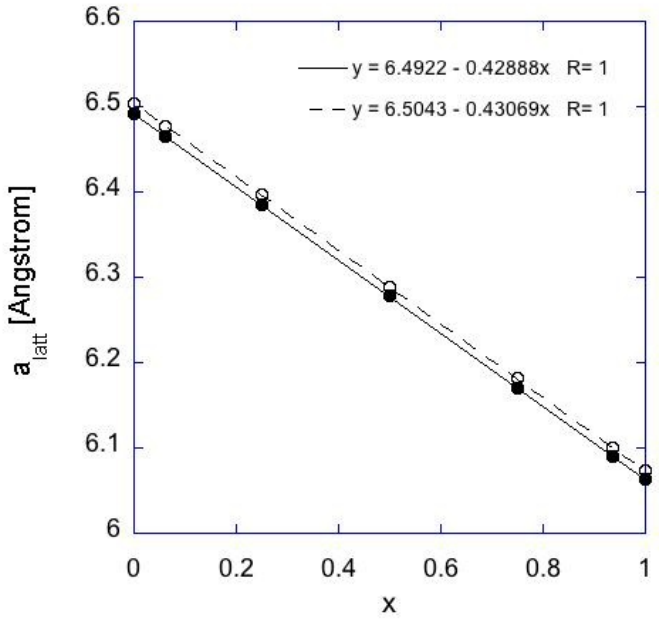

Figure 2-1. The lattice parameter as a function of composition (mole fraction of Se) for two tem- peratures: 300K (solid circles) and 533K (open circles). The lattice parameter for a mixture is calculated from the average volume as $a_{latt} = (< V > /216)^{1/3}$, for a system consisting of 216 unit cells. The typical standard error for each data point is 0.0014A. Also shown are the perfect linear fits to the data; the mean deviation from the linear fit is 0.0005 A, for both temperatures.

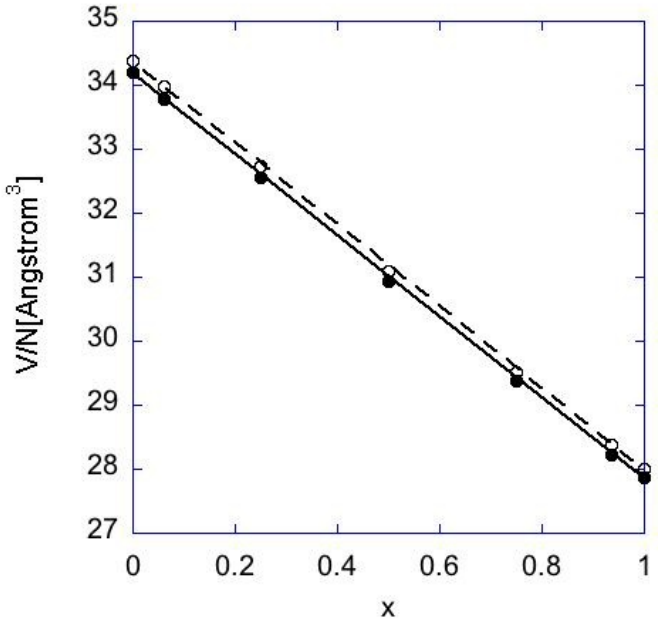

Figure 2-2. The volume per particle as a function of composition for two temperatures: 300K (solid circles) and 533K (open circles). The mole fraction of Se is denoted by *x*. The typical standard error for each data point is 0.011 A^3. The straight lines are the linear relationship that constitutes ideal solution behavior for the volume, i.e., $v^{id}(x) = xv_2 + (1 - x)v_1$. For both temperatures, the simulation data indicate that there is a slight negative deviation from ideality, in accordance with the results of figure 1 (see Appendix A).[12]

Here, λ is a constant with units of energy, and θ_{jik} the angle subtended at particle i, formed by the ij bond and the ik bond. The cosine of θ_{jik} expressed in terms of distance vectors is,

$$\cos\theta_{jik} = \frac{\mathbf{r}_{ij}\mathbf{r}_{ik}}{r_{ij}r_{ij}} = \hat{\mathbf{r}}_{ij}\hat{\mathbf{r}}_{ik} \qquad (3)$$

$cos\theta_0 = 1/3$, and $g(r)$ is a decay function with a cutoff between the first- and the second-neighbor shell. The decay function used by Stillinger and Weber is:

$$g(r) = \exp(\gamma\sigma/(r - a\sigma)) \qquad (4)$$

Finally, the pair-potential contribution is strictly of finite range, a, and is of the form

$$v_2(r) = \varepsilon A(B(\sigma/r)^p - (\sigma/r)^q)e^{1/(r-a\sigma)}; \quad r \le a\sigma \qquad (5)$$

It has a depth of $-E$ at the minimum, and conveniently has a vanishing slope at $r = a\sigma$. In all cases, here and below, $p = 4$ and $q = 0$.

To extend the Stillinger-Weber approach to atomically mixed systems, such as CdTe, CdSe and $CdTe_{1-x}Se_x$, Zhou et al.[2] generalized the expressions above, such that the parameters reflect the nature of the particular atoms that are involved in the 2- or 3-body interaction. Denoting the species with capital indices I, J and K we generalized the three-body term as follows,

$$h_{IJK}(r_{ij}, r_{iik}, \theta_{jik}) = \sqrt{\lambda_{IJ}\lambda_{IK}}\, g_{IJ}(r_{ij}) g_{IK}(r_{ik})(\cos\theta_{jik} - \cos\theta_0)^2 \tag{6}$$

where

$$g_{IJ}(r) = \exp(\gamma_{IJ}\sigma_{IJ} / (r - a_{IJ}\sigma_{IJ})) \tag{7}$$

Similarly, for the pair potential part, the parameters E, A, B, σ and a become dependent on the type of atom pair,

$$v_{IJ}(r) = \varepsilon_{IJ} A_{IJ}(B_{IJ}(\sigma_{IJ} / r)^p - (\sigma_{IJ} / r)^q)\exp(\sigma_{IJ}(r - a_{IJ}\sigma_{IJ}); \quad r \le a_{IJ}\sigma_{IJ} \tag{8}$$

Earlier, we introduced a potential parameter set for a large range of group II-VI compounds and their mixtures (see Zhou et al.[2]). This set of parameters allows for an accurate representation of the semiconductor crystals and their alloys. For convenience, we have collected the parameter values needed for $CdTe_{1-x}Se_x$ in Table 2-1.

VIII. RESULTS

Our simulations are performed at (constant) zero pressure and at (constant) room temperature (T = 300K) and one elevated temperature similar to what QDs would experience in applications (i.e., 260°C, or T = 533K). We start with the lattice parameters of zincblende crystals of the compound mixtures, $CdTe_{1-x}Se_x$, as a function of composition. To report the composition we will use the mole fraction of the Se anion, that is, $x \equiv NSe/(NSe + NTe)$.

We have collected the basic simulation results for the *pure* compounds in Table 2-2, where we list the lattice parameter, volume per particle, potential energy per particle and the surface energy per unit area. Below we provide the data for the mixed crystals in the form of excess functions of mole fraction x which, when combined with the tabulated data, allow for the calculation of all the quantities addressed in this paper.

Table 2-2: Basic simulation results for the structure and energies of the pure compounds CdTe and CdSe, at two temperatures.

	T[K]	a_{latt}[A]	V/N [A^3]	U_{pot}/N[eV]	U_s[eV/nm^2]
Cd-Te	300	6.491918	34.2002	-2.138597	4.211947
Cd-Te	533	6.503747	34.3875	-2.107696	4.207991
Cd-Se	300	6.063162	27.8617	-2.483526	5.758274
Cd-Se	533	6.073452	28.0038	-2.452310	5.745397

Nearly a century ago Vegard [4] noticed that for several compounds, such as ionic salts, the lattice parameter is a near-linear function of x. This relationship is now known as Vegard's law, and it is a widely-used approximation for estimating the lattice parameter of various classes of compounds. Thus,

$$a_{12}(x) = xa_2 + (1-x)a_1 \tag{9}$$

where aj denotes the lattice parameter of compound j. In figure 1 we plot the lattice parameter as a function of composition, x. For both temperatures we observe perfectly linear behavior. The linear thermal expansion coefficients is small (4.4×10^{-5}A/K at x = 0 and 5.1×10^{-5}A/K at x = 1), as the solid is nearly harmonic.

Ideal solution theory is an alternative mixture theory, with great application in fluid state theory [5]. It too is defined by a linear relationship for thermodynamic properties (e.g., enthalpy, free energy). For example, the volume per particle, $v = V/N$, for an ideal solution is given by

$$v_{12}^{id}(x) = xv_2 + (1-x)v_1 \qquad (10)$$

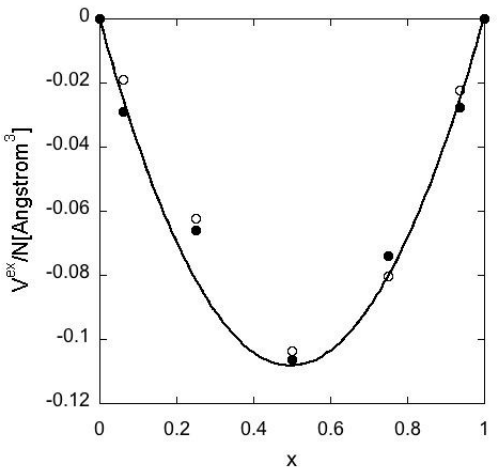

Figure 2-3. The lattice excess volume per particle, $v^{ex}_{12} \equiv v_{12} - v^{id}_{12}$, as a function of composition, for a compound mixture of $CdTe_{1-x}Se_x$. We show two temperatures, 300K(solid circles) and 533K (open circles). The black curve is expression 11, and is indistinguishable for the two temperatures. For more details, see the discussion in appendix A.

The volume per particle is displayed in Fig. 2-2 together with fits based on relationship 10. Clearly, the volume per particle as measured for the compound mixture is very close to the ideal solution. It shows only a very slight negative deviation. As we used the *NpT* ensemble the volume of the simulation cell fluctuates. The distribution of the instantaneous volume per particle over time is characterized by a standard deviation of about $0.03A^3$.

The fact that the lattice parameter, rather than *v*, more closely follows linear behavior is significant [6]. One can easily convince oneself that perfect linear behavior of the lattice parameter (Vegard's law), and perfect linear behavior for the volume (ideal solution theory) cannot both be satisfied at the same time (unless, trivially, $a_1 = a_2$ and, hence, $v_1 = v_2$). Moreover, we can show that Vegard's law implies a *negative* deviation from ideal behavior for the volume. This deviation grows with the disparity of the lattice parameters of the pure crystals. This is demonstrated in Appendix A.

Thermodynamic properties, Y, of nonideal solutions are commonly expressed in terms of excess properties, i.e, $Y^{ex}_{12} \equiv Y_{12} - Y^{id}_{12}$, to facilitate the development of approximate thermodynamic models [5]. For the volume the ideal solution value is a linear combination of the pure component volumes, V_i, i.e., $V^{id} = \sum_i V_i$, and similarly for the energy and enthalpy. Further, the excess volume equals the volume change of mixing, ΔV, and similarly the excess enthalpy equals the enthalpy change of mixing, ΔH.

Given that $v_{12} = V_{12}/N = a^3_{12}$ for an 8-atom zincblende unit cell, it follows that

$$8v^{ex}_{12}(x) = \left[xa_2 + (1-x)a_1\right]^3 - xa_2^3 - (1-x)a_1^3. \qquad (11)$$

From this we see that, apart from a trivial case (i.e., $a_2 = a_1$), $v_{12}^{ex} \neq 0$. In other words, Vegard's law implies nonideal behavior and, moreover, it leads to an expression for the excess volume that is a simple cubic function of x. The results for our compound mixtures, $CdTe_{1-x}Se_x$, are shown in Fig. 2-3, together with estimations based on expression 11, with the coefficients determined by Vegard's law (see Appendix A). The latter expression provides an excellent approximation, reconfirming the accuracy of Vegard's law for this compound mixture.

There have been other reports in the literature regarding the lattice parameter as a function of composition. In particular, Denton and Ashcroft [7] studied binary mixtures of hard spheres (HS) of different diameter. They report an adherence to Vegard's law, but for thermodynamic states along the solid-fluid coexistence line, as opposed to keeping both p and T constant. In Appendix B we revisit those results and also introduce results for a HS system of *nonadditive* spheres that closely mimics our SW model.

There appears to be only a limited number of reports in the literature on measurements of the lattice parameter of ternary compounds, such as $CdTe1-xSex$. In his review Williams [8] cites the work of Ben-dor and Yellin [9] and reports the lattice constant for x= 0.05 (0.6462 nm) and x=0.3 (0.6353 nm). Our values are 0.6470 and 0.6363 nm respectively, in excellent agreement.

We now turn to the potential energy, $Upot$, as a function of x, which we note is related to enthalpy, H, by

$$H / N = \frac{3}{2} kT + U_{pot} / N + pv \qquad (12)$$

where k is Boltzmann's constant. For our simulations at zero pressure, we find that H/N simply differs from U_{pot}/N by a constant equal to 1.5×0.025852 eV (T = 300K) or equal to 1.5×0.045930 eV (T = 533K). Given that the simulations are run at constant p and T, and p = 0, the standard error in H/N is equal to the standard error in $Upot/N$, or 0.00005 eV. The results for $Upot$ are depicted in Fig. 2-4, showing a nearly linear relationship. More detail is shown in Fig. 2-5, where we subtracted the ideal solution behavior and plotted the excess value, $U^{ex}_{pot} = \Delta H$, where the latter

quantity is the enthalpy of mixing. We notice that ΔU^{ex}_{pot} is a very weak function of T. Thus all the T-dependence of H comes from the ideal gas contribution. We will make use of this observation below, when we discuss phase behavior. As was the case in Fig. 2-3 for the excess volume, the excess potential energy can be represented accurately by a simple cubic function (see the fits in Fig. 2-5).

VIII.1 Phase behavior

To determine the free energy of mixing, $\Delta G = \Delta H - T\Delta S$, we require the entropy of mixing. In principle, one can calculate this quantity from a simulation using a variety of thermodynamic integration methods, see for instance reference [10]. Here, however, we will follow Hildebrand [11] and estimate the entropy of mixing by assuming ideal mixing, i.e.,

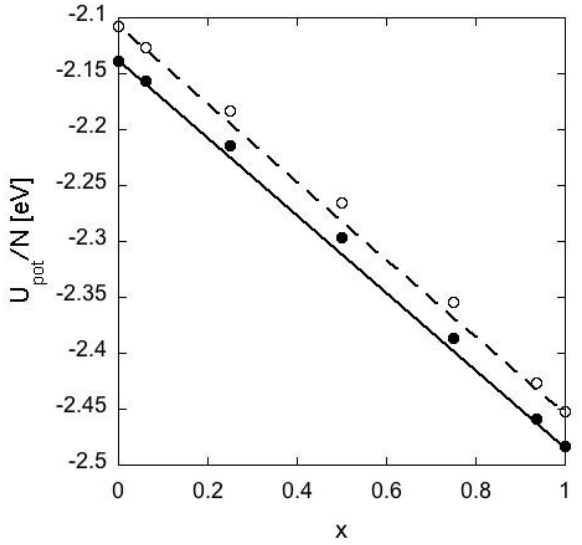

Figure 2-4. The potential energy per particle as a function of composition, for a compound mixture of $CdTe_{1-x}Se_x$. Two sets of data are shown: T = 300K (solid circles, solid line), and T = 533K (open circles, dashed line). The typical standard error for each data point is 0.00005 eV. The straight lines indicate ideal solution behavior. The data indicate a positive deviation from ideal solution behavior, see Fig. 2-5.

$$-\Delta S^{id}/Nk = x\,lnx + (1-x)\,ln(1-x), \tag{13}$$

and we obtain the Gibbs free energy of mixing as

$$\Delta G \approx \Delta H - T\Delta S^{id}. \tag{14}$$

In 1927 Hildebrand [11] coined the phrase "regular solution" for a solution that combines

nonideal behavior for the enthalpy with an ideal entropy of mixing. We show the results for the free energy of mixing in figure 2-6, where we plotted the dimensionless quantity $\Delta G/NkT$ for the two temperatures for interest. As we have seen above, the enthalpy of mixing (i.e., the excess potential energy, plotted in figure 2-5) is positive, but the entropy term is sufficiently large to make mixing favorable [12]. At the high temperature (T = 533K), a single mixed phase is always the stable phase and, thus, there exists complete miscibility over the entire range. However, the room temperature curve displays two points of inflection, and thus over the mole fraction range $0.298 < x < 0.815$, a linear combination of two phases is slightly lower in free energy. Thus, in that range phase separation might occur. From figure 2-5 we see that the excess potential energy is nearly independent of T. If we assume U_{pot}^{ex} is indeed constant with temperature then it is straightforward to determine an upper consolute temperature of T = 335K (or 62°C). The composition at the consolute point is x = 0.575. Within the analysis presented, the two phases coexisting below T = 335K are both randomly substituted lattices. One phase is rich in Te, the other is rich in Se. Above T = 335K there exists just a single randomly substituted phase. For a nanoparticle of $CdTe_{1-x}Se_x$, the phase separation we just identified might be suppressed, if the associated positive interfacial free energy contribution were to outweigh the free energy gain from a phase separation.

VIII.2 Simulations of Finite Samples

As stated, the results presented above concern bulk phase simulations performed in the NpT ensemble, using periodic boundary conditions in all three directions. It is of interest to investigate the behavior of a finite block of material (see figure 2-7), surrounded by vapor (i.e., near vacuum given the low vapor pressure). One question to address concerns whether alloying (the replacement of Te atoms by Se atoms) can produce any noticeable effect due to site percolation. For example, in lattice models of conductivity, populating a lattice with a certain fraction of filled sites can lead to a sudden onset of breakthrough conduction when a certain threshold of site occupancy is reached. For the diamond lattice this occurs when the occupancy fraction reaches a threshold of 0.4299870. In an infinite lattice, above this occupancy threshold there is always at least one cluster that spans the entire system, providing conduction across the sample.

According to the data in Table 2-1, replacing one Te atom by Se in a finite sample of CdTe reduces the bond lengths around the Se guest atom. Locally, there is a slight contraction of the lattice that is resisted by the surrounding CdTe solid. It is conceivable that, as the concentration of Se is

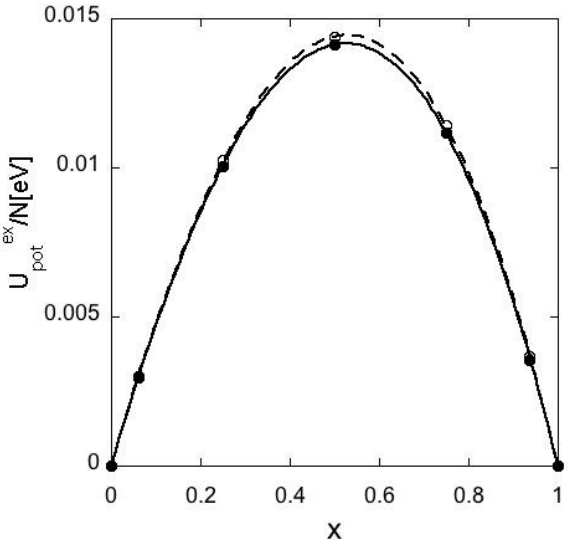

Figure 2-5. The excess potential energy per particle, or enthalpy of mixing ($\Delta H/N$), as a function of composition for a compound mixture of $CdTe_{1-x}Se_x$. We show two temperatures: T = 300K results are shown by solid circles and a solid line, while T = 533K are denoted by open circles and a dashed line. The curves are near perfect cubic fits (constrained to pass through (0,0) and (1,0)) to the excess potential energy: the solid line is $0.050645x - 0.038916x^2 - 0.011729x^3$, the dashed line corresponds to $0.051111x - 0.038149x^2 - 0.012962x^3$.

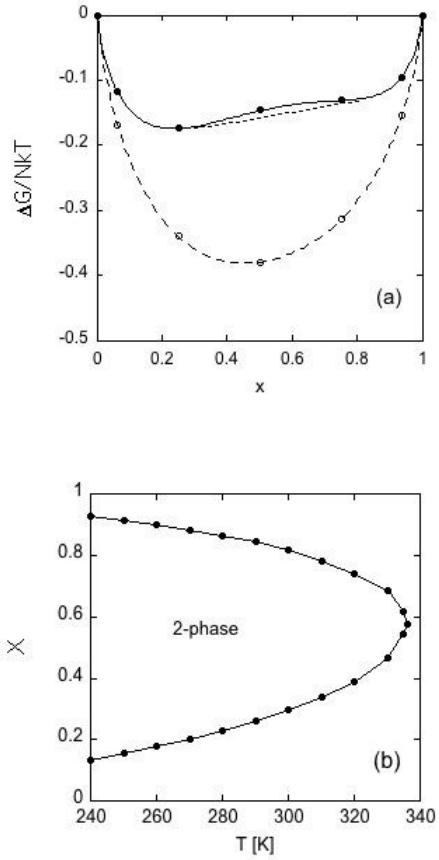

Figure 2-6. (a) The excess Gibbs free energy per particle as a function of composition, for a compound mixture of $CdTe_{1-x}Se_x$. We show two temperatures: T = 300K results are shown by solid circles and a solid line, while T = 533K are denoted by open circles and a dashed line. The curves represent regular solution theory: combining the excess enthalpy with the ideal entropy of mixing. For T = 533K the system is miscible over the entire range. For T = 300K the presence of the inflection points in ΔG suggest incomplete miscibility: two stable phases exist in the composition range $0.298 < x < 0.815$, as indicated by the dotted line, which represents the common tangent. Assuming a temperature independent excess potential energy (see figure 2-5) allows us to estimate the upper consolute temperature as T = 335K. (b) The coexistence composition envelope as a function of temperature. The coexisting phases consist of two randomly-substituted lattices, and are determined from the common tangent construction indicated in (a). One phase is rich in Te (small values of x), the other is rich in Se (large values of x). The consolute temperature is T = 335K and at x = 0.575.

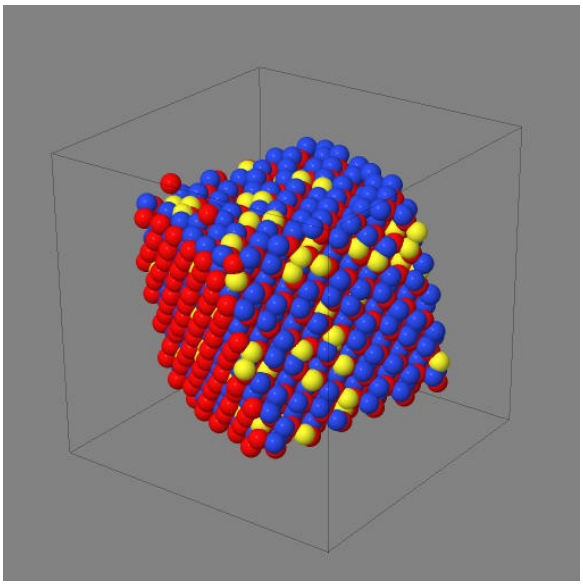

Figure 2-7. Image of the cubic nanoparticle of $CdTe_{1-x}Se_x$, x = 0.2 used in the MD simulation. The edge length is approximately 3.83 nm. Cd is shown in red, Te in blue and Se atoms are drawn in yellow. Three (100) faces are terminated by Cd while the opposing (100) faces are terminated by a mixture of Te and Se

increased from zero, a critical mole fraction of Se is reached above which the lattice can no longer maintain the CdTe lattice spacing and a marked change in volume occurs. To investigate this effect we prepared a cube of CdTe (216 unit cells, 1728 atoms total) surrounded by a vacuum, and performed NVT simulations. Because the vapor pressure is negligible, this simulation corresponds to simulations at a constant vapor pressure, which happens to be essentially zero. Strictly speaking, the volume for the finite-sized relaxed crystalline particle is not well defined, but a good objective measure of its size can be obtained from 1) the average next-nearest neighbor distance between two Cd atoms, R_{CdCd}, or 2) from the radius of gyration, $R_G = \left[N^{-1} \sum_i \left(\mathbf{r}_i - \mathbf{r}_{cm} \right)^2 \right]^{1/2}$ of the entire cube. Here $\mathbf{r}_{cm} = N^{-1} \sum_i \mathbf{r}_i$ represents the center of mass position of the cube.

We present the results for R_{CdCd} in figure 2-8, and the radius of gyration results are shown in the inset to that figure. Both constitute linear measures of the structure of the compound mixture. The bond length shown is an average over all $CdCd$ pairs in the cube, which necessarily includes atoms that are close to the (100) surface where there is some relaxation of the bond lengths. Despite this effect the bond length follows a near perfect linear behavior. This is expected on the basis of Vegard's law, and indicates that there is no appreciable mechanical response that can be attributed to site-percolation. In a zincblende crystal the Cd-Cd distance is related to the lattice parameter, i.e., $R_{CdCd} = R_{TeTe} = \sqrt{2} a_{latt}$, and thus the slopes of of the fits shown in figures 2-1 and 2-8 are related by a factor of $\approx \sqrt{2}$ also. The radius of gyration, R_G, of a cube of length L is equal to $L/2$.

Our cube contains 6 unit cells on the side thus the slope of the fit in the inset to figure 2-8

should approximately be $6/\sqrt{2}$ times that of the slope of the fit in figure 8. This is indeed the case, c.f., 0.1269 nm vs 0.1284 nm, respectively.

We have determined the deviation from linear behavior of the bond length with composition by calculating $R^{ex} \equiv R - R^{id}$. The dimensionless ratio, R^{ex}/R^{id} exhibits a maximum deviation from zero $\approx 0.1\%$ and occurs near $x = 0.5$.

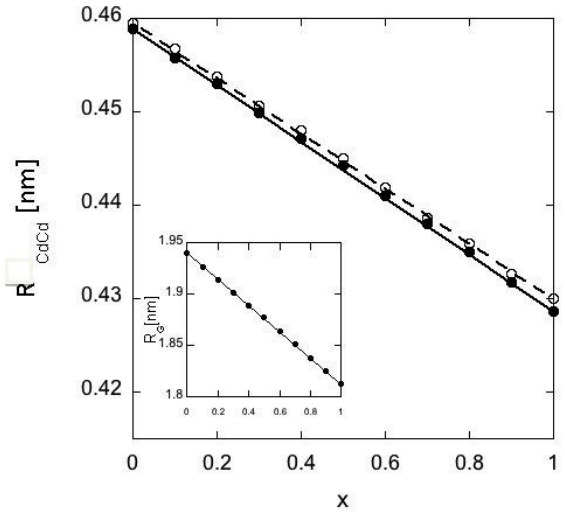

Figure 2-8. The bond length R_{CdCd} as a function of composition (i.e., mole fraction of Se). Two temperatures are shown: T = 300K (solid circles, solid line) and T = 533K (open circles, dashed line). The straight line corresponds to ideal solution behavior for the bond length, i.e., a linear combination of R_{CdCd} in pure CdTe and pure CdSe. The inset shows the radius of gyration, R_G, as a function of composition for T = 300K. The straight line corresponds to ideal solution behavior for the radius of gyration, i.e., a linear combination of R_G of a cube of pure CdTe and that of pure CdSe.

VIII.3 Surface energy

The results of the previous two sections, the bulk and a finite cubical particle, allow us to make an estimate of the surface energy as a function of composition. The cubical particle has six (100) faces. Three of these are terminated by Cd atoms, while the remaining three are terminated by the anion (Te or Se). The surface energy, U_S, is defined as

$$U_s = \frac{N_p}{A_p}\left(U_p / N - U_b / N\right) \qquad (15)$$

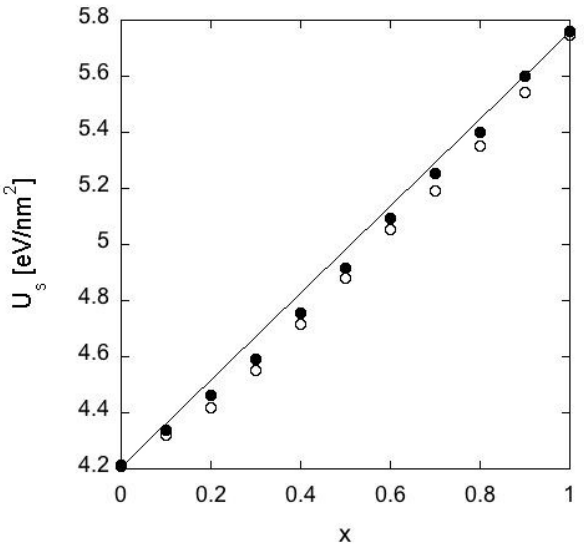

Figure 2-9. The surface energy versus the mole fraction of Se for a cube of edge length ≈ 3.6 nm. We show the results for two temperatures: T = 300K (solid circles, solid line) and T = 533K (open circles, dashed line). The typical standard error of the data points is 0.005 eV/nm^2. The straight line indicates ideal solution behavior for the surface energy.

where the subscript "p" denotes a property of the finite particle (e.g., cube), while the subscript "b" denotes a bulk property. $Ap = Ap(x)$ denotes the total surface area of the particle. We note that U_S is not a pure surface quantity, as the particle's edges and vertices must also make a contribution that is included in the difference on the right hand side. In principle, by studying particles of different sizes one could potentially extract the edge and vertex contributions. The first scales as $(Ap)^{1/2}$ and the other is constant.

The results for U_S as a function of composition are shown in figure 2-9, which shows that the surface energy is positive and is mostly a linear function of the mole fraction. Following the discussion above, it is natural to apply ideal solution theory and define a surface excess energy as the deviation from ideal behavior, viz.,

$$U_s^{ex} = U_s - U_s^{id} \tag{16}$$

The results for the excess surface energy are shown in figure 2-10 for T = 300K and T = 533K, together with a cubic fit. We see that the excess surface energy is negative over the entire range, and appears to be slightly asymmetric. The negative sign indicates that mixing inside a nano- particle helps to lower the energy per unit area, and hence the surface free energy per unit area. This implies that for $CdTe_{1-x}Se_x$ the mixed state is stabilized by the presence of free surfaces.

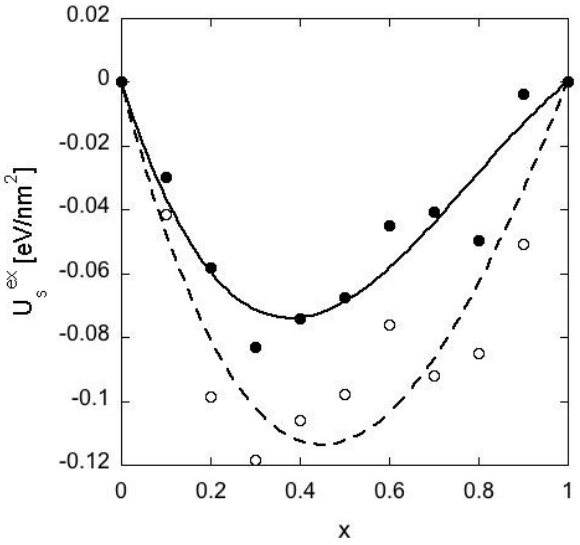

Figure 2-10. The excess surface energy versus the mole fraction of Se for a cube of edge length ≈ 3.6 nm. We show the results for two temperatures: T = 300K (solid circles, solid line) and T = 533K (open circles, dashed line). The data show a negative deviation from ideal solution behavior that increases with temperature. The curves are simple cubic fits, constrained to go through (0,0) and (1.0), to the excess surface energy: the solid line is $-0.43606x + 0.75778x^2 - 0.321720x^3$, and the dashed line corresponds to $-0.54056x + 0.72157x^2 - 0.181010x^3$.

IX. DISCUSSIONS AND CONCLUSIONS

We have investigated the behavior of mixed crystals of CdTe and CdSe, type II-IV compounds. In particular, we have studied $CdTe_{1-x}Se_x$ over the entire range of x, using molecular simulation. We employed our recently developed set of Stillinger-Weber potentials [1, 2], which provide an accurate intermolecular model for this kind of study.

Crystals of $CdTe_{1-x}Se_x$ obey Vegard's law perfectly. For the two temperatures studied, room temperature (300K) and an elevated temperature (260°C, 533K) that QDs might experience during operations, combined with zero pressure, the lattice parameter is a perfect linear function of mole fraction. This behavior was first observed for salt crystals by Vegard. We showed that perfect linear behavior implies a cubic function of x for the excess volume. We compared the observed behavior with that of two simple geometric models, binary hard spheres mixtures and a nonadditive hard sphere model of a zincblende mixture. Both these models show deviations of Vegard's law, indicating that simple geometric models cannot explain all the behavior we observe.

We also examined the thermodynamic properties of $CdTe_{1-x}Se_x$. In particular, we obtain the potential energy (enthalpy) and compare with ideal solution theory. There is a positive excess enthalpy that is essentially independent of T over the temperature range studied. By combining, a cubic excess enthalpy with an ideal solution entropy of mixing we calculated the Gibbs free energy of mixing. We find that at room temperature there is a phase separation into two phases, each randomly mixed. For T = 533K there is complete miscibility.

The phase segregation behavior is expected to be even more pronounced when CdTe is combined with CdS. This is indicated by an inspection of potential parameters for II-VI elements

Zn-Cd-Hg- S-Se-Te [2]. It shows that for a Cd compound the largest difference in lattice parameter as well as the potential energy occurs between CdTe and CdS. This most likely will produce a larger deviation in nonideality for the enthalpy and a higher upper consulate temperature, predicting stronger phase segregation. Similarly, when CdSe is combined with CdS, one has the smallest differences in lattice parameter and potential energy, and consequently one would expect their mixtures to show most mixing and be most like an ideal solution.

Finally, by performing simulations of finite samples, cubic nanoparticles, we obtained an estimate for the surface energy as a function of composition. The excess surface energy is negative, indicating that a finite particle is stabilized by a mixed phase.

APPENDICES

Appendix 2-A

Expanding equation 11 for the excess volume, we obtain a cubic equation in x, viz.,

$$8v_{12}^{ex}(x) = c_0 + c_1 x + c_2 x^2 + c_3 x^3 \quad (17)$$

where the coefficients ci in terms of $a1$ and $a2$ are given by

$$\begin{aligned} c_0 &= 0 \\ c_1 &= 3a_1^2 a_2 - 2a_1^3 - a_2^3 \\ c_2 &= 3a_1 a_2^2 - 6a_1^2 a_2 + 3a_1^3 \\ c_3 &= 3a_1^2 a_2 - 3a_1 a_2^2 + a_2^3 - a_1^3 \end{aligned} \quad (18)$$

vanish for $x = 1$. Thus,

$$\begin{aligned} 8v_{12}^{ex} &= c_1 x + c_2 x^2 - (c_1 + c_2)x^3 \\ &= c_1 x\left(1 + \frac{c_2}{c_1}x - (1 + \frac{c_2}{c_1})x^2\right) \end{aligned} \quad (19)$$

where the last line is included to show that v^{ex}_{12} is reduced to the familiar form $Ax(1-x)$ under $c1$. That is, the excess volume of the mixture has a symmetric parabolic conditions where $c_2 \approx -c_1$. That is, the excess volume of the mixture has a symmetric parabolic form, with an extremum at $x = 1/2$. This form is often encountered in the description of nonideal liquid mixtures [5].

We can also show that v^{ex}_{12} is negative (or zero) for all compositions. Thus, Vegard's law implies that the volume of the mixture exhibits negative deviations from ideality. To demonstrate this, note that

$$c_1 = a_1^3\left[3\frac{a_3}{a_1} - 2 - (\frac{a_2}{a_1})^3\right] \quad \text{for } a_1, a_2 \geq 0$$

Specializing to the case of $CdTe_{1-x}Se_x$ at $T = 300K$ for which $a_1 = 6.49192$ A and $a_2 = 6.06316$ A at $T = 300K$, we find that $c_1 = -0.437680\ A^3$, $c_2 = 0.447533\ A^3$ and $c_3 = -9.8524 \times 10^{-3}\ A^3$. For $T = 533K$ the values are very similar, $a_1 = 6.50375$ A and $a_2 = 6.07345$ A, which gives $c_1 = -0.441614\ A^3$, $c_2 = 0.451573\ A^3$ and $c_3 = -9.9588 \times 10^{-3}\ A^3$

For both temperatures we conclude that $c_2 \approx -c_1$, and we see that the excess volume is indeed nearly a symmetric parabola,

$$8v_{12}^{ex}(x) \approx c_1 x(1-x) \tag{21}$$

as is confirmed in figure 2-A-1.

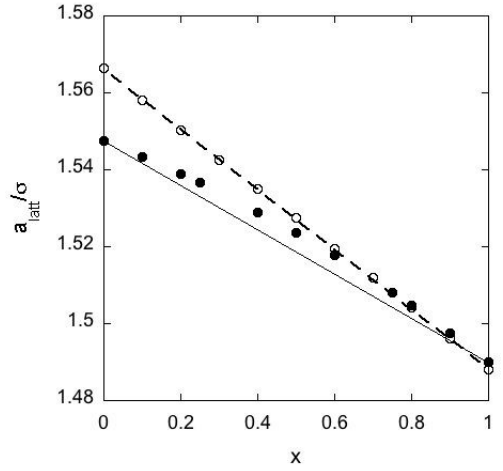

Figure 2-A-1. The lattice parameter as a function of mole fraction for a substitutional fcc crystal of binary additive HS mixture, with $\sigma_2/\sigma_1 = 0.95$(c.f., [7, 10]). The abscissa, x, denotes the mole fraction of species 2, that is, $x \equiv N_2/(N_1 + N_2)$. We consider two cases: the first measures the lattice parameter at constant p and T (solid circles). We observe significant (positive) deviations from Vegard's law (represented by the dotted straight line). A similar conclusion applies to the volume per particle (not shown), thus the excess volume is positive. For the second case, following Denton and Ashcroft [7], the open circles show the lattice parameter along the solid-fluid coexistence line, using the coexistence data of Kranendonk and Frenkel [10] to determine the pressures and compositions. Remarkably, the coexistence data display perfectly linear behavior of the lattice parameter.

Appendix 2-B

In this appendix we explore Vegard's law for binary and ternary hard sphere systems, applying both aditive and nonadditive collision rules. Some years ago, Denton and Ashcroft [7] reported on the applicability of Vegard's law for hard sphere systems. In particular, they used density functional theory (DFT) to study substitutional fcc crystals of binary hard sphere mixtures. They were motivated to determine if simple geometric effects, e.g., the size difference between hard spheres, could play a significant role in determining the crystalline structures of alloys, expanding on previous studies of solids of binary hard sphere mixtures [10, 13]. The authors chose to make the comparison by looking at systems under conditions of solid-fluid coexistence, and concluded that for a size ratio $\sigma_2/\sigma_1 = 0.95$, close to unity, Vegard's law is a good prediction. Significant deviations were observed for size ratios σ_2/σ_1 deviating more from unity.

Notice that, by choosing to follow the coexistence line, one does *not* follow a constant T and p path. Although a valid choice, it is not clear that this is the appropriate condition to use if we seek to make contact with our semi-conductor compounds. Therefore, in figure 2-B-1 we deviate from Denton and Ashcroft [7], and return to the common approach and show the lattice parameter for constant T and p. We see that the data appear fairly linear, but clearly exhibit a positive deviation from

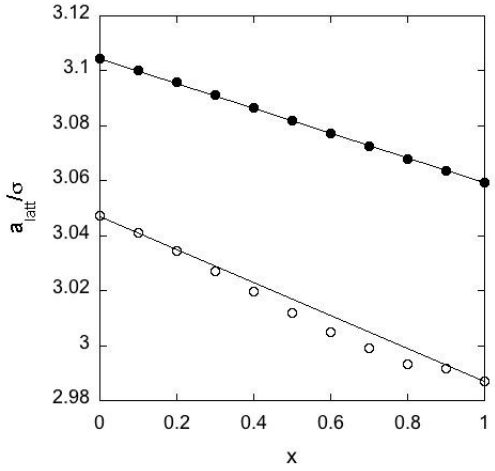

Figure 2-B-1. The lattice parameter as a function of mole fraction for a substitutional zincblende crystal of a nonadditive HS mixture where species 2, with $\sigma_2/\sigma_1 = 1$ is replaced by species 3. The abscissa x denotes the mole fraction of species 3, i.e., $x \equiv N_3/(N_2 + N_3)$. We show the results for two size ratios. The solid circles correspond to a nonadditive mixture where $\sigma_3/\sigma_1 = 0.95$, and $\beta p\sigma^3 = 3.0977$, while open circles are the results for $\sigma_3/\sigma_1 = 0.90$, and $\beta p\sigma^3 = 4.0481$. We observe that for the size ratio closer to unity Vegard's law is obeyed, while for $\sigma_3/\sigma_1 = 0.90$ there are significant (negative) deviations.

Vegard's law, to be contrasted with the conclusions of Denton and Ashcroft. The same

conclusion applies to the volume per particle (not shown), which also exhibits a positive deviation from ideal solution behavior.

As mentioned above, Denton and Ashcroft [7] used DFT to determine fluid-solid coexistence. Un- fortunately, the DFT coexistence results are markedly different from the molecular simulation prediction of Kranendonk and Frenkel [10] (c.f., figures 1 of reference [7] and [10]). Since the latter authors do not supply the lattice parameter, we ran our own molecular dynamics simulations to determine the lattice parameter of the solid phase. To this end we extracted [14] the coexistence mole fractions and pressure data of figure 1 of [10], and ran molecular dynamics calculations for these conditions. The resulting coexistence lattice parameter versus x is shown in figure 2-B-1. It clearly follows Vegard's law. Somewhat surprisingly, our simulation lattice parameter coincides with the DFT lattice parameter of Denton and Ashcroft [7]. This implies that the DFT and simu- lation agree on the packing fraction and mole fraction relationship of the solid phase at coexistence, despite large discrepancies in the $p-x$ coexistence diagram.

The compound lattices discussed for $CdTe_{1-x}Se_x$ differ form the binary HS mixtures in that the zincblende structure of $CdTe_{1-x}Se_x$, the arrangement of the Cd atoms is a constant feature. That is, one of the two fcc sub-lattices that make up the zincblende structure is not subject to alloying, only the anion fcc sub-lattice is. To investigate whether geometric considerations alone could explain the $CdTe_{1-x}Se_x$ compound adherence to Vegard's law, we investigate a ternary mixture of non-additive hard spheres. A nonadditive HS system is defined by specifying the cross collision diameter for spheres of species i colliding with spheres of species j as

$$\sigma_{ij} = \alpha_{ij}\left(\sigma_i + \sigma_j\right)/2 \qquad (22)$$

From this definition we see that the traditional additive HS mixture is recovered by setting $\alpha_{ij} =$
$\alpha_{ji} = 1$ for all $\{i,j\}$ pairs.

We know that a binary system with $\alpha_{ij} = 1$ if $i \neq j$, and $\alpha_{ij} = 2$ if $i = j$ will result in a zincblende structure when the packing fraction is sufficiently big (e.g., for a packing fraction [15] $\eta > 0.135$, say). This is a direct result of the "charge ordering" that is induced by this particular choice of parameters. That is, species 1 prefers to be surrounded by species 2, and each species prefers to increase the distance between like partners. For other parameter combinations, the NaCl or CsCl structures are found to be the stable crystal structures. Thus, even though the non-additive HS model is purely repulsive and short-ranged, it shares the charge ordering and crystal structures with the ionic systems.

To facilitate the comparison with our $CdTe_{1-x}Se_x$ simulations we extended the binary non-additive HS mixture to a ternary mixture, and performed molecular dynamics simulations for a mixture where $\sigma_2/\sigma_1 = 1$; $\sigma_3/\sigma_1 = 0.95$ or 0.9. This choice of parameter values was combined with the following non-additivity parameters: $\alpha_{12} = \alpha_{13} = 1$; $\alpha_{ij} = 2$ for $i = j$; and $\alpha_{23} = 2$. The latter choice ensures that species 2 and 3 repel each other as other like species. We can think of this model as equivalent to a ternary ionic salt such as $KCl_{1-x}Br_x$, which is one of the salts originally studied by Vegard [4].

Results for the lattice parameter of the non-additive ternary model are compiled in figure 2-B-1, where we plot the results for two size ratios, i.e., σ_3/σ_1 = 0.95 and 0.9. We observe that for a size ratio of 0.95 the ternary non-additive HS model follows the linear Vegard predication, just as it does for $CdTe_{1-x}Se_x$. However, there is a very slight negative deviation for the larger mole fractions. This system also closely follows ideal solution behavior. In contrast, for a size ratio of 0.9 there is a noticeable (*negative*) deviation from Vegard's law, as there is from ideal solution behavior. The results presented in this appendix illustrate that Vegard's law is not generally obeyed and, moreover, simple geometric models such as binary HS, or ternary non-additive HS are not more likely to exhibit linear behavior for the variation lattice parameter with mole fraction.

---

[1] Stillinger, F.H., and Weber, T. A., *Computer simulation of local order in condensed phases of silicon* , Phys. Rev. B., **31**, 5262 (1985)

[2] Zhou,X., Ward,D. K., Martin, J. E., van Swol, F. B. , Cruz-Campa,J. L. , and Zubia, D. *Stillinger-Weber potential for the II-VI elements Zn-Cd-Hg-S-Se-Te* , Phys. Rev. B., **88**, 085309 (2013)

[3] Allen, M.P., and Tildesley, D.J., *Computer simulation of Liquids* , Clarendon Press, Ox- ford(1987)

[4] Vegard, L., *Die Konstitution der Mischkristalle und die Raumfllung der Atome*, Zeitschrift fur Physik **5** 1726 (1921)

[5] Hildebrand, J.H., and Scott, R. L. *Regular Solutions*, Prentice Hall, (1962); Prausnitz, J.M., *Molecular Thermodynamics of Phase-Equilibria*, 3rd Edition, Prentice Hall (1998)

[6] It is interesting to note that Vegard [4], analyzing the results for mixed crystals of KBr and KCl, commented on the fact that the lattice parameter follows the linear relationship more closely than the volume.

[7] Denton, A.R., and Ashcroft, N. W., *Vegard's law*, Phys. Rev. A., **43**, 3161 (1991)

[8] Williams, D. J., in "*Properties of Narrow Gap Cadmium-based Compounds*, Emis DataReviews Series, The Institution of Engineering and Technology, Ed., Clapper, P. (1994).

[9] Ben-dor, L., and Yellin, N. *Vertical unseeded vapor growth and characterization of* $Cd_{0.95}Zn_{0.05}Te$ *Crystals*, J. Cryst. Growth, **71**, 519-524 (1985)

[10] Kranendonk, W.G. T., and Frenkel, D., *Computer simulation of solid-liquid coexistence in binary hard sphere mixtures*, Mol. Phys., **72**, 679-697 (1991)

[11] Hildebrand, J. H., Nature, **168**, 868 (1951), Proc. US Nat. Acad. Sci., **13**, 267 (1927)

[12] Small changes in volume will produce small changes in the entropy. These can be calculated through thermodynamic integration of the Maxwell relation $(\partial S/\partial V)_T = (\partial p/\partial T)_V$, see [11]. For our system, the largest correction in $\Delta S/Nk$ is small enough to be neglected: -0.0085 at $x = 0.5$.

[13] Jackson., G., van Swol, F., And Rowlinson, J.S., J. Phys. Chem., **91**, 4907 (1987)

[14] The fluid(f) and solid(s) coexistence data of figure 1 of reference [10] can conveniently be fitted by simple cubic expressions: $p_f = 13.635 - 0.09461x - 3.2366x^2 + 1.3976x^3$ and $p_S = 13.635 - 0.2585x - 1.8775x^2 + 0.19629x^3$

[15] The packing fraction is given by $\eta = (\pi/6)\sum_i N_i\sigma_i^3/V$

i

CHAPTER 3: HETEROJUNCTIONS of MODEL CdTe/CdSe MIXTURES.

Frank van Swol, Xiaowang W. Zhou, Sivakumar R. Challa[2], James E. Martin

Sandia National Laboratories
P.O. Box 5800 Albuquerque, New Mexico 87185

[2]Chemical and Biological Engineering Department
The University of New Mexico Albuquerque, NM 87106

December 11, 2014

ABSTRACT

We report on the strain behavior of compound mixtures of model group II-VI semiconductors. We use the Stillinger-Weber hamiltonian that we recently introduced, specifically developed to model binary mixtures of group II-VI compounds such as CdTe and CdSe. We employ molecular dynamics simulations to examine the behavior of thin sheets of material, bilayers of CdTe and CdSe. The lattice mismatch between the two compounds leads to a strong bending of the entire sheet, with about a 0.5 to 1° deflection between neighboring planes. To analyze bilayer bending, we introduce a simple one-dimensional (1D) model and use energy minimization to find the angle of deflection. The analysis is equivalent to a least-squares straight line fit. We consider the effects of bilayers which are asymmetric with respect to the thickness of the CdTe and CdSe parts. From this we learn that the bending can be subdivided into four kinds depending on the compressive/tensile nature of each outer plane of the sheet. We use this approach to directly compare our findings with experimental results on the bending of CdTe/CdSe rods. To reduce the effects of the lattice mismatch we explore diffuse interfaces, where we mix (i.e., alloy) Te and Se, and estimate the strain response.

ACKNOWLEDGEMENTS

We are grateful to Dr. Jim Miller for many helpful discussions and suggestions. This research supported by the United States Department of Energy, Office of Basic Energy Sciences, Division of Materials Sciences and Engineering and Sandia's LDRD program. Sandia National Laboratories is a multi-program laboratory managed and operated by Sandia Corporation, a wholly owned subsidiary of Lockheed Martin Corporation, for the U.S. Department of Energy's National Nuclear Security Administration under contract DE-AC04-94AL85000.

X. INTRODUCTION

Semiconductors based on nanocrystalline materials of CdSe/CdTe mixtures have been found to have novel electronic and optical properties that could benefit photovoltaic, display, and medical imaging technologies [1, 2]. Optoelectronic and photovoltaic behavior of these semiconductors can be tuned to specific applications by engineering nanostructures with various compositions, shapes, and morphologies. Semiconductor compounds, such as CdTe, CdSe, and mixtures thereof (or $CdTe_{1-x}Se_x$ for short) [2], are often used in configurations that produce interfaces (or heterojunc- tions) between the two phases. Effects of strain arising from lattice mismatch at heterojunctions in the binary compound mixtures on band structure has been studied in crystalline solids and nanocrystals [1, 3, 4, 5, 6, 7, 8]. A compressive or tensile stress is understood to lead to an increased or decreased band gap energy, respectively.

A familiar example is that of core/shell quantum dots (QDs) where the core may consist of CdTe and the surrounding shell of CdSe. Other examples include rod shaped particles [9] and layered materials. Even though the crystal forms of the two phases may be the same (e.g., zincblende or the hexagonal form: wurtzite), the lattice mismatch between the two pure phases, i.e., the difference in lattice parameter, makes for an interface that displays strain and stress. The existence of the strain a nd/or stress is believed to affect the performance of the semiconductor materials, for instance through the radiationless recombination of electrons and holes. Strain could also lead to a gradual transition from type-I to type-II semiconductor behavior by designing carefully controlled heterojunction size/structure or composition [3, 7]. So, it becomes necessary to study how lattice mismatch at heterojunctions can lead to structure relaxations and shape modifications.

It has been proposed that alloying of the interfacial region may help to relieve some of the stress and or strain. Experimentally, it is difficult to measure the stress and strain behavior at the nanoscale. Microscopy techniques such as TEM and SEM (tunneling and scanning microscopy) can image individual atoms but it is still hard to determine the full 3D structure and the identity of each atom. Stress measurements would appear to be even more challenging. At the same time, these are situations where simulations can be usefully employed to explore the behavior of heterojunctions, and provide a fundamental understanding of the phenomena.

In this paper we report on molecular dynamics (MD) simulations of a thin finite-sized bilayer sheet with a heterojunction where CdTe meets CdSe (or, in some cases, CdS). The bilayer sheet responds to the lattice mismatch with a pronounced curvature that corresponds to neighboring crystal planes to adapting a wedge shape with a 0.5 to 1° angle between them. Shim and McDaniel [2] have observed bending of the heterojunction of CdTe and CdSe by HAADF-STEM (High angle annular dark field scanning transmission electron microscopy imaging). Their high-resolution images show that the bending is the result of an actual deflection of the crystal planes. The authors call the extent of the deflection surprising. Specifically, the angle of deflection was found to be larger than what was expected if the lattice spacing simply varied from the bulk CdSe value on one side of the bilayer to the bulk CdTe value on the opposing side. Instead, the crystal plane spacing on the outer edge of the CdSe layer was *smaller* than that in a bulk CdSe phase,

while on the opposing side it was *equal* to that of bulk CdTe.

We introduce a simple 1D model to help explain the nature of the observed curvature, and apply it to predict the angle of deflection. This simple model helps in providing an explanation as to why the crystal bending for symmetric bilayers is larger than expected based on the bulk lattice parameters. In addition, the 1D model can be used to generalize to the richer class of asymmetric bilayers as well as predict bending responses to alloying of the bilayer.

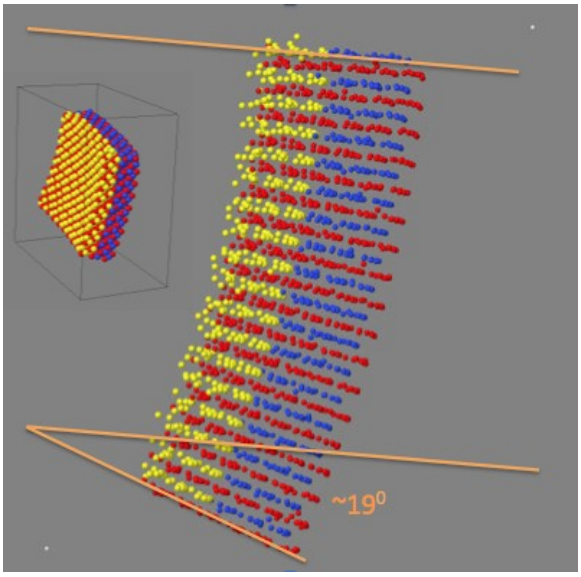

Figure 3-1. Curved minimum energy configuration of a bilayer sheet of CdSe (left layer) and CdTe (right layer). The dimensions of the sheet are approximately 56.5*A* ×56.5*A* ×18.8*A*. Cd, Se and Te, are denoted by red, yellow and blue respectively. The dots are not drawn to scale, to highlight the layers. The image presents a side-on view of a three-dimensional bilayer zincblende structure (see the inset), highlighting the alternating stacking between layers of Cd and layers of Se and Te. Each layer contains 54 atoms. The orange construction lines help to determine the degree of bending (here expressed as an angle) for a sheet of 36 layers. The deflection angle between two layers is $\sim 0.54^{\circ}$.

XI. RESULTS

To model group II-VI materials we use the three-body potenial we recently developed [10, 11], which is based on the well-known Stillinger-Weber potential [12]. We performed molecular dynamics (MD) simulations of N=1944 particles, arranged in a zincblende structure of 9 by 9 unit cells in a sheet of 3 unit cells. Each cubic unit cell contains 8 atoms. Half the group VI atoms were Te while the other half were Se (and in some runs S). The sheets consist of 12 atomic (100) planes parallel to the heterojunction. Initially, the entire starting sample generated consisted of CdTe. All the Te atoms on one side of the sheet were then replaced by Se. MD simulations were performed at room temperature, i.e. $T = 300K$, which is far below the melting point and, hence, the sample remains in the crystalline state. The sheet is surrounded by vacuum, and periodic boundary conditions were applied in all directions. For some of the samples we use steepest descent to obtain energy- minimized structures to facilitate quantifying the degree of bending.

Given that the lattice parameters are significantly different (i.e. 6.46A for CdTe, 6.06A for CdSe and 5.84A for CdS) the sheet initially exhibits considerable stress, which is then released by pronounced

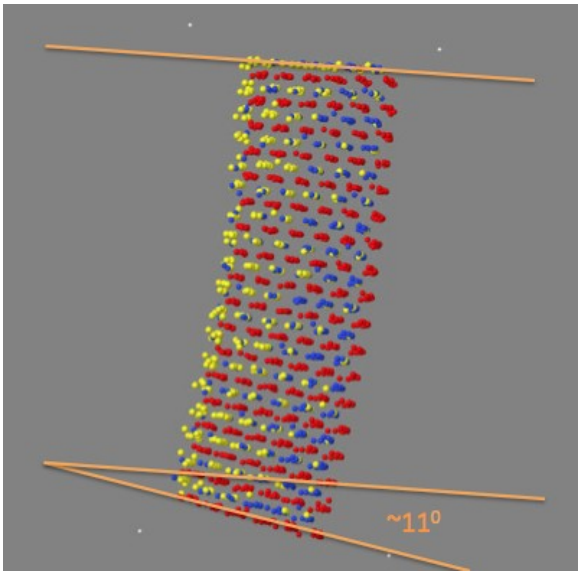

Figure 3-2. Curved minimum energy configuration of a bilayer sheet of CdSe (left layer) and CdTe (right layer), see also caption of figure 1. This image shows the result of performing 800 swaps between Se and Te atoms, thereby alloying the heterojunction. This results in a reduction of the sheet's curvature. The deflection angle between two layers is $\sim 0.31^{\circ}$.

deformation of the sheet. In figure 3-1 we show a typical example of a relaxed bilayer sheet. The final appearance of the sheet is a strongly bent bilayer with the CdTe side a convex surface (positive radius of curvature) while the CdSe side is concave (a negative radius of curvature), see the inset to figure 3-1. The entire sheet is still locally in a zincblende structure, but a highly distorted one. In the zincblende structure there are alternating (100) planes of Cd and planes of Se/Te atoms. In the figure, the sheet is angled in such a way as to highlight the relative position of the planes. We note that all the atoms are still organized in planes, but that neighboring

planes exhibit a deflection from the parallel configuration into a wedge-like structure. We quantified the bending by
simply measuring the angle of the two outer atomic planes (perpendicular to the heterojunction), as indicated in the figure. The angle is found to be $\sim 19^{\circ}$, which corresponds to a deflection angle of $\sim 0.54^{\circ}$ for each neighboring pair of atomic planes.

In figure 3-2 we present the MD results for a slightly alloyed sample, where some Se atoms appear to the right of the heterojunction and the same number of Te atoms have moved to the left. This was accomplished by performing 800 pair swaps or interchanges, where a pair swap is executed by randomly selecting one Se atom and one nearby Te atom, and then swapping their positions.

Alloying reduces the curvature. The measured bending angle of the entire sheet is $\sim 11^{\circ}$, which corresponds to a deflection angle of $\sim 0.31^{\circ}$ for each neighboring pair of planes. By symmetry, a fully randomly mixed bilayer has zero bending, of course.

Shim and McDaniel [2] reported on a very similar experimental system involving CdTe domains grown beyond the tips of a seed CdSe nanorod. The authors used a HAADF-STEM image to illustrate [13] the nonparallel arrangement of the crystal planes, and measured the angles of deflection between two neighboring crystal planes. As suggested by the lattice parameters, the layers were closer together on the CdSe side of the rod, and wider on the CdTe side. The authors noted, however, that the narrowest part of the interlayer distance was noticeably smaller than that in pure

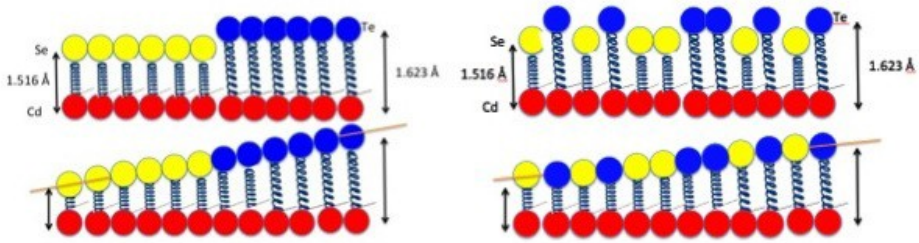

Figure 3-3. Sketch of the one-dimensional model used to analyze the crystal plane deflections observed in the curved bilayer sheets shown in figures 3-1 and 3-2. We show the Cd atoms in red, Se in yellow, and Te in blue. Each Se and Te is connected to a Cd atom. We approximate the interaction potential by a harmonic potential, illustrated by a spring. On the left (top) is an unconstrained fully segregated bilayer configuration, whereby each atomic pair is at an equilibrium distance of $a_{latt}/4$, which leads to a larger distance for CdTe. The bottom left diagram illustrates the effect of constraining the Se and Te to a crystal plane (as observed in figures 3-1 and 3-2), and minimizing the total energy. The result is a deflection of the crystal plane. On the top right we show an alloyed bilayer configuration that has two Te atoms swapped for two Se atoms (in a symmetric fashion). The panel on the bottom right shows the constrained, energy minimized configuration for the alloyed bilayer, at a reduced slope.

CdSe. However, the widest part was about the same as in pure CdTe. In their figure (i.e., figure 7) they label the CdSe side as "in compression" and the CdTe side as "in tension". The authors further reported that there was variation in the results among the different rods, some had larger deviations from the bulk spacings.

We will now show that a quantitative treatment for the crystal plane deflection and the size of the observed angle can be obtained from a simple model. In addition this approach can be readily used to explore the behavior of asymmetric bilayers as well as the effects of alloying. A schematic of our model is depicted in figure 3-3. We consider one Cd crystal plane interacting with one crystal plane made up of equal amounts of Se and Te (we will consider unequal amounts later in this paper).

The left panels show a completely segregated bilayer structure that has all the Se atoms on the left hand side and all the Te on the right. Each Se or Te atom interacts with a Cd atom in the layer below. We approximate the interaction by a simple harmonic potential, and in the figure we illustrate its equilibrium position by the extent of the spring. The Se-Cd equilibrium distance is equal to one quarter of the lattice parameter of pure CdSe at T = 300K, i.e, $a_1 \equiv a_{latt}/4$ = 1.51579 A. Similarly, the Te-Cd equilibrium distance is denoted $a_2 \equiv a_{latt}/4$ = 1.62298 A. For the horizontal spacing we choose a constant distance equal to the average of a_1 and a_2, so that the thickness of the bilayer sheet is equal to that of the simulated structure.

The total energy of the model structure is defined as the sum of the harmonic pair energies, i.e.,

$$U = \frac{1}{2}\sum_{i=1}^{2N} \varepsilon_i \left(y_i - a_i\right)^2 \qquad (1)$$

where index i denotes the pairs, N is the number of Se atoms (equal to the number of Te atoms), and $a_i = a_1$ for a Se-Cd pair and a_2 for a Te-Cd pair. The separation (i.e., extension of the spring) of pair i is denoted by y_i, the horizontal position of the pair is x_i. The strength of the interaction of pair i is E_i. For simplicity we set $E_1 = E_2 = 1$.

To represent the structures observed in figures 3-1 and 3-2, we require that the positions of all the Se and all the Te atoms fall onto one plane. In our one-dimensional model that requirement is equivalent to stating all the positions y_i fall onto a straight line. The application of this constraint is illustrated in the bottom panels of figure 3-3.

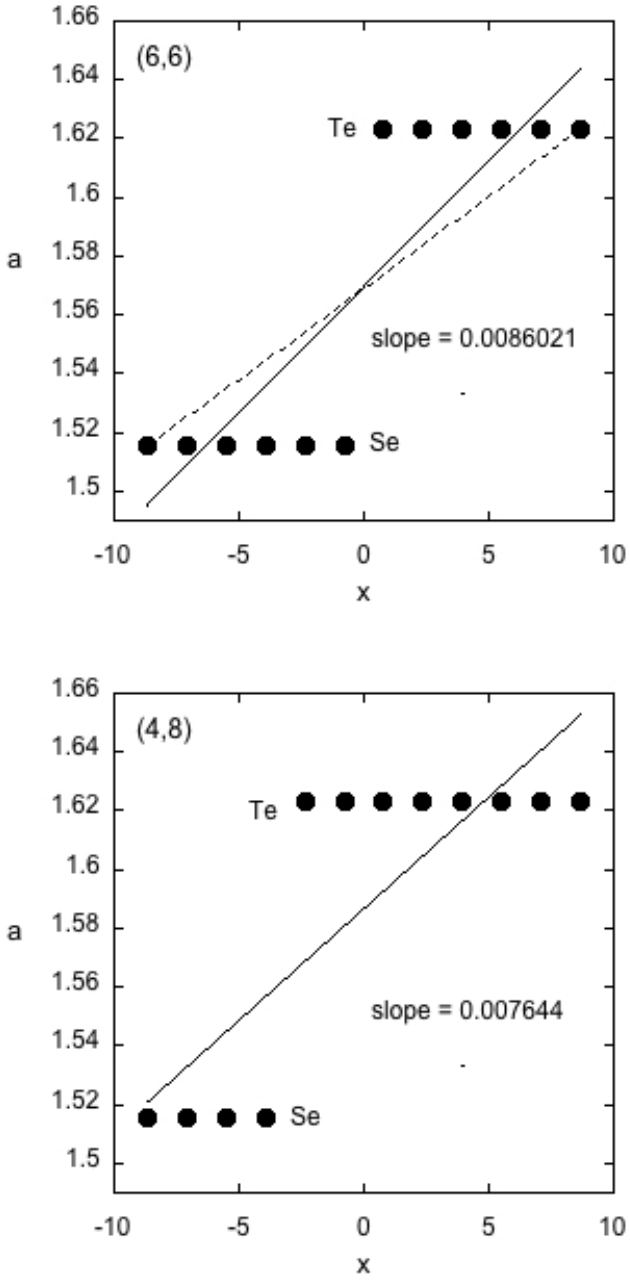

Figure 3-4. One-dimensional model of the layer deflection for a bilayer sheet. In the top panel the bilayer is symmetric, 6 planes each (labeled (6,6)), while in the bottom panel we show an asymmetric bilayer (i.e., (4,8)). We plot the distance, *a* (in A), between atoms in neighboring crystal planes. One plane (not shown) consists of 12 Cd atoms, the other layer has *m* Se atoms (on the left) and *n* Te atoms (on the right). The solid line shows the result of a energy minimization which is equivalent to a least-squares fit of a straight line. The slopes correspond to 0.49° (top panel) and 0.44° . For the (6,6) bilayer the left hand side is in compression, while the other end is in tension. In contrast, for the (4,8) bilayer both sides are in tension.

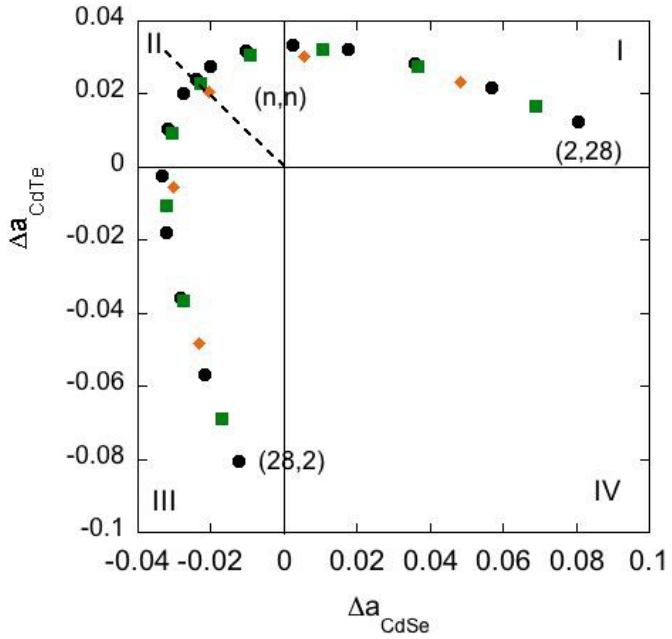

Figure 3-5. The effects of asymmetry in a CdSe/CdTe bilayer. We use the simple 1D model to explore the distortion response of segregated (*n, m*) bilayers, consisting of *m* planes of CdSe next to *n* planes of CdTe. We have plotted the distortion $\Delta a = a_i - a_2$, in Angstroms, at the outer edge of the CdTe layer versus the $a_i - a_1$ at the outer edge of the CdSe layer. The circles, squares and diamonds refer to bilayers composed of a total of 30, 20 and 12 planes respectively. The dashed line indicates the thickness trend of *symmetric* films for which $m = n$. The data fall into three of four quadrants. In quadrant I both deviations are positive indicating that both outer edges of the bilayer are in tension, while in III both are in compression. Quandrant II signifies compression of the CdSe side combined with tension on the CdTe side (see figure 3-4). No segregated bilayers can end up in quadrant IV. However, alloyed bilayers can.

The equilibrium configuration of our model is defined as the straight-line configuration that minimizes the total energy U , see equation 1. Writing $y_i = b + mx_i$, the problem then is to determine the slope m and intercept b that minimizes U. This is in fact a very familiar problem, as it is identical to performing a least-squares fit of a straight line to 2N measured data points $\{x_i, y_i\}$. For the latter problem one minimizes the chi-square merit function,

$$X^2(m,b) = \sum_{i=1}^{2N} \left(\frac{a_i - b - mx_i}{\sigma_i} \right)^2 \qquad (2)$$

where σ_i is the uncertainty associated with measurement $y_i = b + mx_i$. Thus, setting $\sigma_i = E_i = 1$, $U = \chi^2/2$.

In figure 3-4, top panel, we illustrate the results of the energy minimization of a perfectly segregated *symmetric* bilayer of CdSe and CdTe. This (n,m) bilayer has $n = 6$ crystal planes parallel to the heterojunction containing Se, and $m = 6$ planes containing Te. The slope of the plane (perpendicular to the heterojunction) that minimizes U is 0.008602 and, as pointed out, it can be most easily obtained by performing a least-square straight-line fit to the data points shown.

Also indicated in figure 3-4 is the result of a linear interpolation between a_1 and a_2, indicated by the dashed line. The slope of this line is a measure of the crystal plane deflection if one naively assumes that the plane spacing across the bilayer varies from that of bulk CdSe phase (on the outer left of the bilayer) to that of bulk CdTe phase (on the outer right of the bilayer). That assumption always leads to an underestimation the angle of deflection between two neighboring planes. Instead, the outer side of the CdSe is found to be in compression, while the outer side of the CdTe part of the bilayer is in tension, as the solid line ends below the Se atoms on the left and above the Te atoms on the right.

Our simple model demonstrates why this has to be the case mathematically. In physical terms, given the imposed constraint that the Se and Te atoms must be co-planar, typically none of the individual pairs i (Se-Cd or Te-Cd) can adopt their equilibrium distance a_i (a_1 or a_2). Instead, for symmetric bilayers, the total energy of the distortion is minimized by over-compressing the outer Se-Cd pairs and over-stretching the outer Te-Cd pairs, such that the inner Se-Cd and Cd-Te pairs can adopt a separation that is closer to the equilibrium distance of the isolated pair.

The results of our simple model are quantitatively correct as well. From the slope found in figure 3-4, $0.008602 \equiv \tan\theta$, we identify the angle of deflection (between [100] atomic planes of a CdSe/CdTe bilayer of 3 unit cells thick) as $\theta = 0.49^\circ$, in good agreement with the MD value of $\sim 0.54^\circ$. Similarly, for a bilayer of CdS/CdTe the MD result is $\theta \sim 0.83^\circ$, while our simple model predicts $\theta = 0.76^\circ$.

By restricting ourselves to symmetric bilayers, we have not presented a complete story of the bending phenomenon. To explore the richness of bilayer response to lattice mismatch we must turn to consider asymmetric bilayers, i.e., $n \neq m$. The bottom panel of figure 3-4 shows the results of a (4,8) bilayer. Here the energy minimization leads to a situation where *both* outer

layers are in tension. Conversely, an (8,4) bilayer has both outer layers in compression. For a given number of planes (i.e. bilayer thickness) there are various combinations m and n to be considered. In figure 3-5 we have collected results for $n+m = 12, 20$ and 30. The last set is thought to correspond to the rod diameter in the work of Shim and McDaniel [2] while the first set is similar to our MD simulations (see figures 3-1 and 3-2). To avoid clutter we generally only plot the data for even values of n and m.

We plot the deviations from the bulk crystal plane spacing on the CdTe side (outer edge) versus the corresponding deviation on the CdSe side (outer edge). We will start with the results of a symmetric (n, n) bilayer. These bilayers all fall onto a straight (dashed) line through the origin, with a negative deviation for the CdSe layer (compression) and a positive deviation for the CdTe layer (tension), c.f., figure 3-4. It can be shown that the angle of deflection of the symmetric bilayers decreases with n, varying as n^{-1}. As we have seen, if we deviate from the symmetric layer and consider a (4,8) layer then we obtain *positive* deviations for both the outer CdSe and CdTe layers. Hence this state lies in the first quadrant of figure 3-5. Larger deviations from the symmetric case produce states placed farther from the origin in quadrant I; maximum amount of strain, therefore, could be expected for severely asymmetric systems. All states in quadrant I exhibit tension on both sides of the bilayer.

An (8,4) bilayer produces a state in the third quadrant, which corresponds to compression on both sides of the bilayer. By varying the values n and m for constant $n + m$ we trace out an envelope of points that populate three of the four quadrants. The data are symmetric around $y = -x$, due to the symmetrical nature of the 1D model. The absence of data in quadrant IV implies that the bilayer cannot combine expansion of CdSe side (which has the smaller lattice parameter) with compression of CdTe side. We will see later that points in quadrant IV can only result from alloying the bilayers.

We now return to the experimental results of Shim and McDaniel who report $\Delta a_{\mathrm{CdSe}} = 0.09$A and $\Delta a_{\mathrm{CdTe}} = 0$. This places their state point on the border of quadrant II and III. Note that Shim and McDaniel report on the spacings between (111) planes, while we have considered (100) planes. Now, the ratio of these two sets of plane spacings is equal to $4/\left(\sqrt{3}/3\right) = 2.31$. Thus, the corresponding Shim-McDaniel estimate for the (100) spacing would be 0.04A, which lies very close to the envelope of points in the phase diagram of figure 3-5. From the estimated thickness, $n + m$=30. We identify the state point which most closely matches $\Delta a_{\mathrm{CdSe}} = 0.04$A and $\Delta a_{\mathrm{CdTe}} = 0$ as $n = 22, m = 8$. This is certainly consistent with the information provided in figure 3-7 of [2], but that work does not report on the specific values for n and m. In addition, we point out that we have used a planar sheet while the experiments were performed with rod-shaped nanoparticles.

Although they observe $\Delta a_{\mathrm{CdTe}} = 0$, Shim and McDaniel label the CdTe as in tension, whereas we consider this side to be in a neutral, unstrained state. It is possible that the authors simply assumed that if the CdSe side was clearly in compression then the other side had to be in tension.

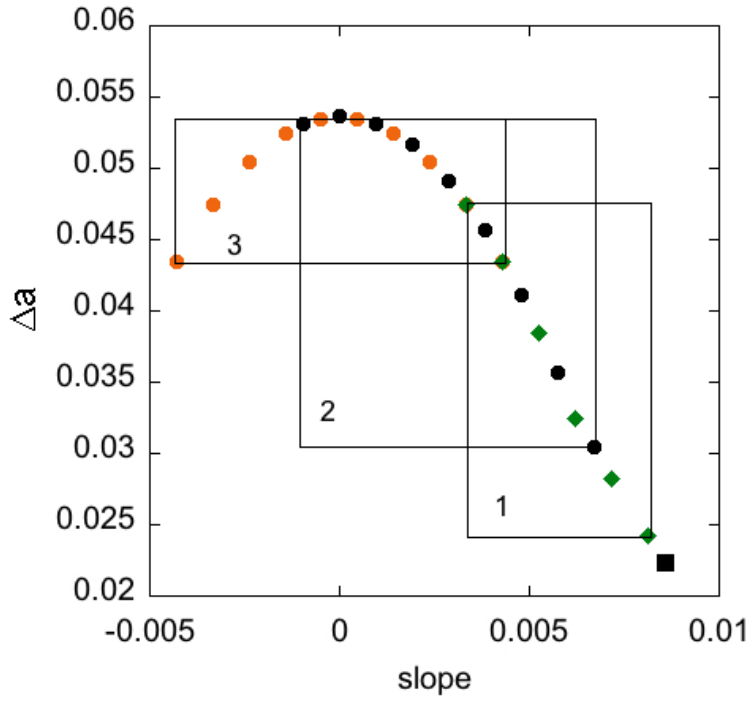

Figure 3-6. The displacement per particle as a function of the slope for all possible symmetric permutations of 1, 2, and 3 particles swaps; $\Delta a \equiv (2N)^{-1}\sum_i |y_i - a_i|$. The black solid square indicates the perfectly segregated configuration. The green diamonds denote one-particle swaps; the solid black circles denote two-particle swaps; while the orange circles are the three-particle swaps. The boxes drawn indicate the range of slope-displacements relationship outcomes for a particular number of swaps, and highlight that there is considerable overlap between 2- and 3-particle swaps, say. There are more permutations than symbols visible in the plot. This is a reflection of degeneracy, the occurrence of which increases with the number of swaps. The loci of the points shown form a quartic, i.e., $y = 0.053785+0.13197x-624.17x^2-11634x^3+3.8058\times10^6x^4$

Although this may appear as a natural assumption, our discussion here clearly demonstrates that bent bilayers can, in fact, exhibit three combinations of tension and compression, as indicated by the three quadrants in figure 3-5. Thus, observing the state of one side of a bent bilayer does not uniquely determine state of the opposite side.

Finally, we use the simple one-dimensional model to study the effect of alloying, limiting ourselves to symmetric bilayers. A schematic of alloying is shown in the one-dimensional representation in figure 3-3, which illustrates the effect of swapping two Se atoms with two Te atoms. For simplicity we will restrict ourselves to the 'symmetric' swaps shown in the panels on the right hand side of figure 3-3, where we swapped Se positions 2 and 4 with Te positions $2N-2$ and $2N-4$. For $N = 6$ one only needs to consider swapping 1, 2, or 3 atoms, as swapping more atoms merely results in reversing the identities of the left and right hand side of the bilayer. In figure 3-6 we have collected the results of alloying. We plot the average displacement per particle, $\Delta a \equiv (2N)^{-1}\sum_i |y_i - a_i|$, versus the slope. We note that all the data fall onto a quartic curve. Alloying reduces the bending of the bilayer (i.e., smaller slope of deflection), while increasing the value of Δa. For our 12 layer sheet, entirely eliminating the bending (i.e., zero slope), can be accomplished with certain two- or three-particle swaps, but not with one-particle swaps.

XII. CONCLUSIONS

The MD simulations of thin bilayers of group II - VI compounds, i.e., CdTe/CdSe structures, that we have presented show that the lattice mismatch produces pronounced bending of the bilayer sheet. The angle of deflection between two neighboring (100) planes is of the order of one degree. Alloying the bilayers produces less bending or smaller angles of deflection. We presented a simple 1D model to help explore the details of this phenomenon. The energy minimization of the 1D model structure is mathematically identical to a simple straight-line least-squares fit, and hence easy to interpret. It gives an accurate prediction of the MD simulation result, and we have used it to explore more details of the bent bilayer structures. For symmetric (*n, n*), fully segregated, bilayers the angle of deflection scales as n^{-1}. More generally, asymmetric bilayers show a variety of outcomes. These are characterized by the distortion on either end of the sheet. Three types of outcomes are found: plane separation reductions on both sides produce a bilayer that is in compression on both sides. Similarly, plane separation increases lead to bilayers that are in tension on both sides. The last type of outcome consists of compression on the CdSe side and tension of the CdTe. The reverse of this latter state is not possible. Finally, all symmetric bilayers lie in quadrant II.

We compared our predictions for the deflection angle, and the compression/tension state of the bilayer, to experimental findings for bilayer CdSe/CdTe rods, as reported by Shim and McDaniel [2] and find good agreement with their high resolution TEM results. Our simple model predicts that the parts of the rods used in these measurements had 27% of the diameter consisting of CdTe. A refinement of our simple model, which uses weighted points to account for the rod shape could potentially produce more accurate results. Our current model also enables a simple assessment of the results of alloying around the heterojunction with an eye on reducing the strain (i.e., the angle of deflection). The model calculations indicate that at a given mole fraction, guest atoms (i.e, Se in CdTe or Te atoms in a CdSe) are most effective in reducing the angle of plane deflection if they are located far from the location of the heterojunction.

[1] Smith, A. M. and Nie, S. M. "Semiconductor nanocrystals: Structure, properties, and band gap engineering", *Acc. Chem. Res.* **43** 190–200 (2010).

[2] Shim M., and McDaniel, H., *Anisotropic nanocrystal heterostructures: Synthesis and lattice strain*, Curr. Op. Solid St. and Mat. Sci., **14**, 83-94 (2010)

[3] Smith, A. M., Mohs, A. M., and Nie, S. M. "Tuning the optical and electronic properties of colloidal nanocrystals by lattice strain", *Nat. Nanotechnol.* **4** 56–63 (2009).

[4] Wei, S. H., Zhang, S. B. and Zunger, A. "First-principles calculation of band offsets, optical bowings, and defects in CdS, CdSe, CdTe, and their alloys", *J. Appl. Phys.* **87** 1304–1311 (2000).

[5] Sadowski, T. and Ramprasad, R. "Core/Shell CdSe/CdTe heterostructure nanowires under axial strain", *J. Phys. Chem. C* **114** 1773–1781 (2010).

[6] McDaniel, H., Zuo, J.-M., and Shim, M. "Anisotropic strain-induced curvature in type-II CdSe/CdTe nanorod heterostructures", *J. Am. Chem. Soc.* **132** 3286–3288 (2010).

[7] Shim, M., McDaniel, H., and Oh, N. "Prospects for strained type-II nanorod heterostructures", *J. Phys. Chem. Lett.* **2** 2722–2727 (2011).

[8] McDaniel, H., Oh, N., and Shim, M. "CdSe–CdSe$_x$Te$_{1-x}$ nanorod heterostructures: Tuning alloy composition and spatially indirect recombination energies", *J. Mater. Chem.* **22** 11621– 11628 (2012).

[9] Saunders, A.E., Koo, B., Wang, X., Shih, C-K, and Korgel, *Structural Characterization and Temperature-Dependent Photoluminescence of Linear CdTe/CdSe/CdTe Heterostructure Nanorods*, ChemPhysChem, **9**, 1158 1163 (2008)

[10] Zhou,X., Ward,D. K., Martin, J. E., van Swol, F. B. , Cruz-Campa,J. L. , and Zubia, D. *Stillinger-Weber potential for the II-VI elements Zn-Cd-Hg-S-Se-Te* , Phys. Rev. B., **88**, 085309 (2013)

[11] van Swol, F., Zhou,X., Challa, S. R., Martin, J. E., *Thermodynamic properties of Model CdTe/CdSe Mixtures*, Mol. Simulat., *in press* (2014)

[12] Stillinger, F.H., and Weber, T. A., *Computer simulation of local order in condensed phases of silicon* , Phys. Rev. B., **31**, 5262 (1985)

[13] See figures 6 and 7 of footnote [2].

CHAPTER 4: RADIATIVE LIFETIMES OF ZINCBLENDE CdSe/CdS QUANTUM DOTS

Ke Gong[a], James E. Martin[b], Lauren E. Shea-Rohwer[b], Ping Lu[b] and David F. Kelley*[a]

[a] Chemistry and Chemical Biology
University of California Merced
5200 North Lake Road, Merced, CA 95343

[b] Sandia National Laboratories
P.O. Box 5800, MS-0892
Albuquerque, NM 87185-0892

ABSTRACT

Recent synthetic advances have made available very monodisperse zincblende CdSe/CdS quantum dots having near-unity photoluminescence quantum yields. Because of the absence of nonradiative decay pathways, accurate values of the radiative lifetimes can be obtained from time-resolved PL measurements. Radiative lifetimes can also be obtained from the Einstein relations, using the static absorption spectra and the relative thermal populations in the angular momentum sublevels. One of the inputs into these calculations is the shell thickness, and it is useful to be able to determine shell thickness from spectroscopic measurements. We use an empirically-corrected effective mass model to produce a "map" of exciton wavelength as a function of core size and shell thickness. These calculations use an elastic continuum model and the known lattice and elastic constants to include the effect of lattice strain on the band gap energy. The map is in agreement with the known CdSe sizing curve and with the shell thicknesses of zincblende core/shell particles obtained from TEM images. If selenium-sulfur diffusion is included and lattice strain is omitted then the resulting map is appropriate for wurtzite CdSe/CdS quantum dots synthesized at high temperatures, and this map is very similar to one previously reported (Embden*, et al.*, *J. Am. Chem. Soc.* **2009,** 131, 14299). Radiative lifetimes determined from time resolved measurements are compared to values obtained from the Einstein relations, and found to be in excellent agreement. Radiative lifetimes are found to decrease with shell thickness, similar to the size dependence of one-component CdSe quantum dots and in contrast to the size dependence in type-II quantum dots.

XIII. INTRODUCTION

Quantum dots (QDs) are of great interest because of their tunable and intense photoluminescence (PL). Very high PL quantum yields and photostability are often obtained from CdSe/CdS core/shell QDs, making them of particular interest. CdSe/CdS core/shell nanocrystals have optical properties that are unique amongst semiconductor QDs and have been extensively studied. Most of these particles are synthesized at high temperatures and have a wurtzite crystal structure, which is the most stable form. Although these core/shell QDs typically have high PL quantum yields when shells are thin (a few CdS layers), the quantum yields drop with increasing shell thickness.[1] Recently Nan *et al*. reported a low temperature synthesis of very high quality zincblende CdSe/CdS core/shell QDs.[2] The PL quantum yields of these QDs is very high and remains high for relatively thick shells. The reason for the differences in the optical properties is that the "synthetic philosophy" for these particles is entirely different than that underlying previous syntheses giving wurtzite particles.

In most syntheses of wurtzite core/shell particles, shell growth is done using a SILAR procedure at fairly high temperatures, > 200 C°.[3-5] There are two reasons for this: first, the high temperatures are needed for the reaction of the cadmium and sulfur precursors to proceed at a reasonable rate; and second, the higher temperatures permit in-situ particle annealing, resulting in better crystallinity. Successive addition of cadmium and sulfur precursors can produce very thick CdS shells, the so-called "giant" nanocrystals.[6, 7] The main problem with this approach is that there is a 4% lattice mismatch between CdSe and CdS that results in considerable lattice strain at the core-shell interface.[8] This strain can be relieved by shell surface reconstruction which readily proceeds above about 200 °C. The result is that the shells are typically irregular and have many surface defects.[9] These defects can act as electron-hole recombination centers, lowering the PL quantum yield.

In contrast, in the recent zincblende synthesis, shell deposition proceeds from a very reactive single CdS precursor[2] at relatively low temperatures, < 160 °C. Surface reconstruction is an activated process and does not readily occur at such low temperatures.[9] The result is that the zincblende core/shell particles are metastable with respect to lattice-strain-induced shell defects and have much more uniform and closer to defect free shells than the corresponding wurtzite particles. This results in very high PL quantum yields, even for particles with comparatively thick shells. The original reports give the PL quantum yields of about 85%. We have optimized this synthesis and get quantum yields of about 95%. Zincblende CdSe/CdS QDs are also quite stable and it seems that these particles hold great promise for applications in photovoltaics and especially light emitting diodes.

Having accurate radiative lifetimes is fundamental to understanding the luminescence of any type of QD. Radiative lifetimes are, in principle, easy to obtain. One simply measures the PL decay kinetics, and in the absence of non-radiative decay pathways, the measured decay time is the radiative lifetime. However, the observed PL QYs of most types of QDs are far below unity, indicating that non-radiative processes compete with luminescence and cannot be ignored. The observed PL decay rate is the sum of the radiative and non-radiative rates, and different

fractions of the sample having different non-radiative rates can make the interpretation of multi-exponential PL decay kinetics ambiguous and problematic.[10]

Radiative rates can also be calculated from absorption spectra using the Einstein relations.[11, 12] Specifically, for a II-VI QD the relation is

$$A = \frac{8\pi\, 0.2303 C_{fs} n_f^3}{N_a c^2 n_a} \left\langle \nu_f^{-3} \right\rangle^{-1} \int \frac{\varepsilon(\nu)}{\nu} d\nu \approx 2.88x10^{-9} C_{fs} n^2 \left\langle \nu_f^2 \right\rangle \int \varepsilon(\nu) d\nu \qquad (1)$$

where N_a is Avogadro's number, c is the speed of light, $\varepsilon(\nu)$ is the molar extinction coefficient (L mol^{-1} cm^{-1}) at frequency ν, ν_f (ν_f) is the fluorescence frequency (wavenumber), brackets denote an averaged quantity, C_{fs} is a factor related to the relative populations in the dark and bright fine structure levels (discussed below) and n_a and n_f are the refractive indices of the surrounding solvent at the absorption and luminescence wavelengths, respectively. In the case where the absorption and luminescence spectra are narrow and there is minimal Stokes shift, the left part of equation 1 simplifies to the right part, with $n = n_a = n_f$. Alternatively, the radiative rate may be given in terms of the oscillator strength of the transition,

$$f_A = \frac{2\pi n e^2 \nu^2}{\varepsilon_0 m c^3} C_{fs} f \qquad (2)$$

where f is given by

$$f = \frac{4m\nu}{e^2} \frac{0.2303 nc\varepsilon_0}{N_a} \int \frac{\varepsilon(\nu)}{\nu} d\nu \qquad (3)$$

These expressions ignore local field effects, which enter into expressions for the absorption and luminescence in the same way, and therefore cancel.

Equations 1 – 3 are the usual expressions for the radiative lifetime, except for the inclusion of the factor that takes into account thermal populations in the angular momentum fine structure, C_{fs}. This factor is given by[10]

$$C_{fs} = \frac{\sum_i f_i \exp(-E_i / k_B T)}{\sum_i \exp(-E_i / k_B T)} \qquad (4)$$

where k_B is the Boltzmann constant, E_i and f_i are the energy and fraction of the total absorption oscillator strength in the *i-th* transition, respectively. There are eight thermally accessible angular momentum sublevels in the $1S_e$-$1S_{3/2}$ exciton. Rapid equilibration with the population of the dark states effectively increases the radiative lifetime compared to the case of a single absorbing and emitting oscillator. This is not a small effect; in the absence of crystal field or

shape anisotropy mixing, five of the eight fine structure sublevels are dark. Following photon absorption, rapid relaxation occurs amongst the bright and dark states and luminescence comes from a temperature-dependent distribution of states, each having its own radiative rate. The energies and oscillator strengths of these different angular momentum sublevels depend of the size, shape and crystal structure of the QD. These energy separations are comparable to kT at room temperature and there is a Boltzmann distribution of populations in these different states, complicating the evaluation of C_{fs}. Accurate calculation of radiative lifetimes requires that the values of the PL energy, the integrated extinction coefficient and C_{fs} be considered.

In this paper we examine the radiative lifetimes of a series of CdSe/CdS core/shell particles having different shell thicknesses. These values are obtained directly from time-resolved measurements and compared to values obtained from static spectra and the evaluation of equation 1 or 2. Agreement between values obtained from these completely different approaches is very good, indicating that the factors controlling the radiative lifetime are well understood.

XIV. RESULTS AND DISCUSSION

Absorption (molar extinction coefficient) and PL spectra of the zincblende CdSe core and CdSe/CdS core/shell QDs are shown in figures 4-1 and 4-2. The extinction coefficient spectra shown in figure 4-1 are determined from raw absorption spectra.

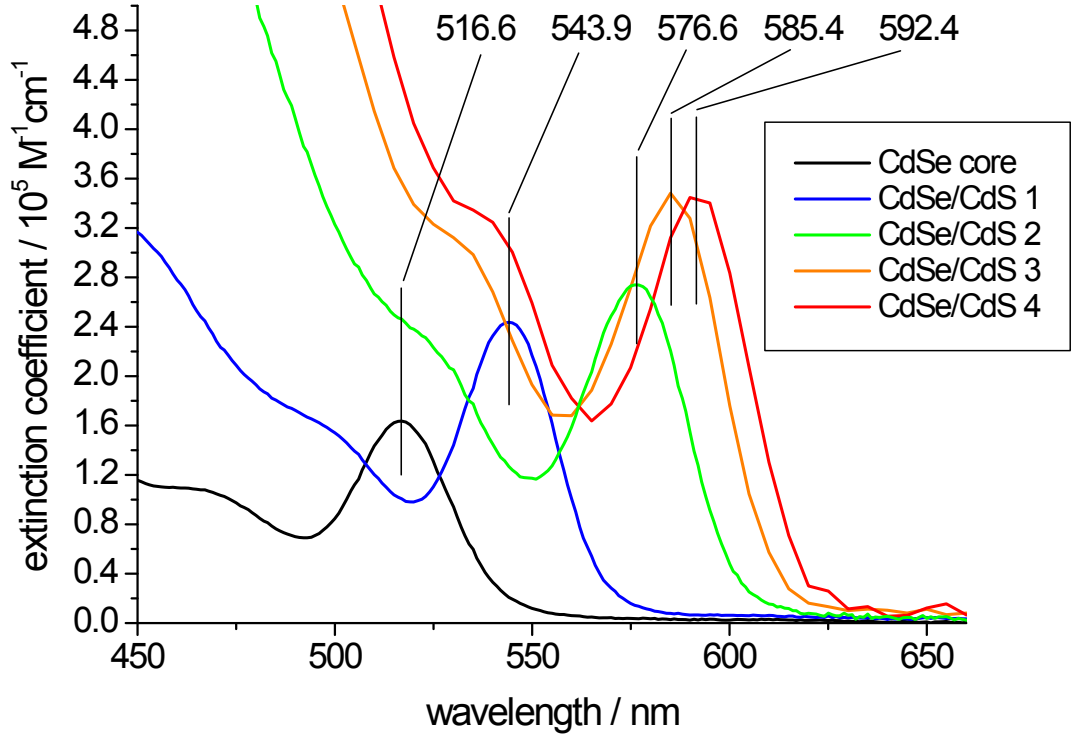

Figure 4-1. Absorption spectra of 2.64 nm zincblende CdSe QDs and corresponding core/shell particles having shell thicknesses of 0.00, 0.39, 1.10, 1.52, and 2.00 nm, as indicated.

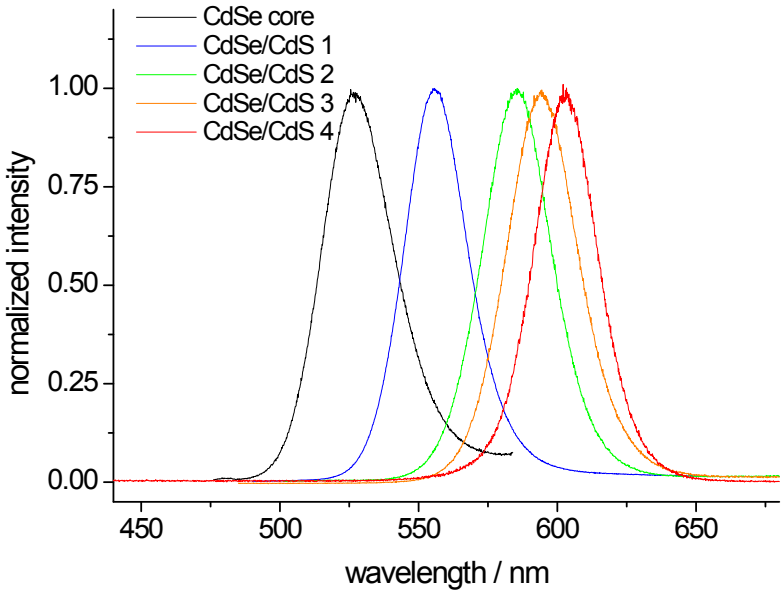

Figure 4-2. Normalized photoluminescence spectra of the same QDs as in figure 4-1.

The outline of the procedure for doing this in the absence of direct concentration determinations is the following. We initially determine exciton energy as a function of core size and shell thickness, making a "map" of exciton wavelength for CdSe/CdS core/shell particles. This is useful because it enables spectroscopic determination of shell thickness for particles for which TEM data are not available. The core diameter and shell thickness results are used along with the known bulk CdSe, CdS and solvent absorption coefficients and refractive indices to obtain extinction coefficients at a wavelength where quantum confinement effects are negligible, in this case, 350 nm. Knowing the extinction coefficient at this wavelength directly converts an absorption spectrum to an extinction coefficient spectrum. The extinction coefficient spectra are then used to obtain absolute oscillator strengths and radiative lifetimes using equations 1 – 4.

1. Exciton energy as a function of core size and shell thickness.

The size-dependent spectroscopy of wurtzite versus zincblende CdSe particles has not been extensively studied, but indications are that the crystal structure makes little difference in the effects of quantum confinement. This is not surprising, as the energetic difference between the two forms is very small, 1.4 meV per CdSe. We therefore assume that size calibration curves obtained for wurtzite may also be applied to zincblende particles. The cores have an absorption maximum at 516.6 nm, see figure 4-1. Using the well-established sizing curve for CdSe particles,[13] this corresponds to 2.64 nm diameter particles. A TEM image of the core/shell particles having an absorption maximum at 592.4 nm (indicated as CdSe/CdS 4 in figures 4-1 and 4-2) is shown in figure 4-3.

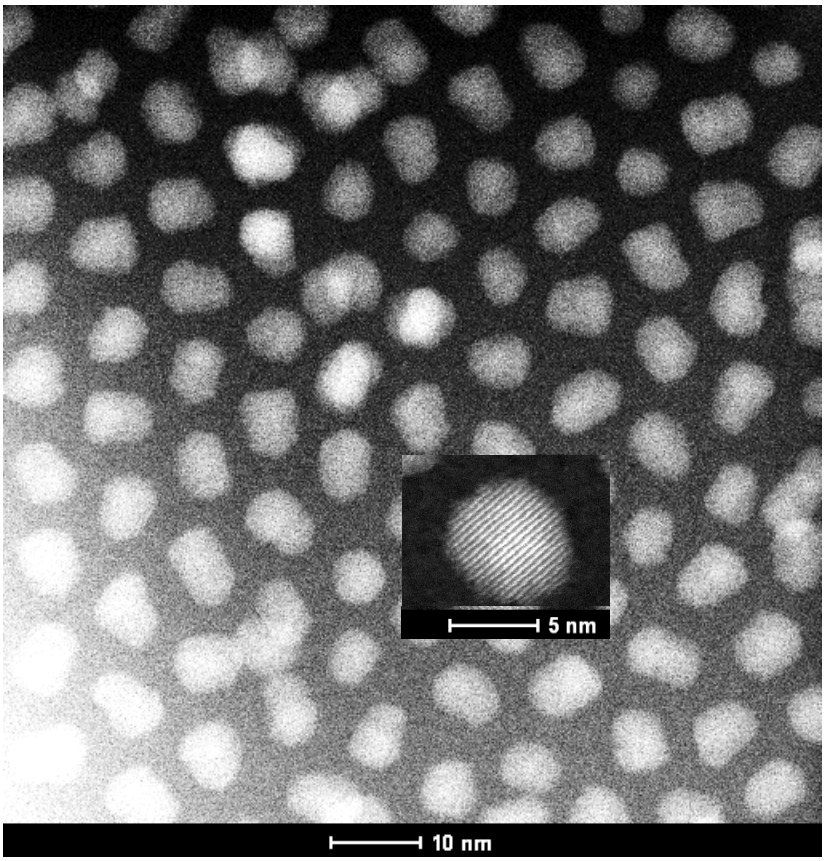

Figure 4-3. TEM image of the core/shell particles having an absorption maximum at 592.4 nm. The inset shows a typical high resolution image.

The particles are somewhat non-spherical, having dimensions varying from about 6.2 to 9.0 nm. The ensemble average dimension is obtained from the measurement of many particles and is found to be 6.6 nm. With the known core diameter of 2.64 nm, these images indicate that for these particles the average shell thickness is 2.0 nm. The shift of the lowest exciton wavelength from 516.6 to 592.4 nm constrains the calculation of any core/shell sizing map.

The approach used here to generate this map is based on the known CdSe sizing curve and calculation of the exciton energies using effective mass approximation (EMA) wavefunctions. Wurtzite and zincblende CdSe have very similar spectroscopic energetic and properties and we make the assumption that the wurtzite CdSe sizing curve can also be used for zincblende particles. EMA calculations are known to predict larger quantum confinement effects than what is observed. These errors are minimized by considering the electron and hole moving in potentials having finite barriers at the particle surface. However, even with finite barriers, EMA calculations typically over-predict the extent of quantum confinement, and the extent of these errors increases with increasing quantum confinement energy. The fundamental problem is that the effective mass is defined as $m^* = \hbar^2 \left(\frac{\partial^2 E}{\partial k^2} \right)^{-1}$, and the plot of E versus k is not quadratic at the larger quantum confinement energies of the smaller particles.[14, 15] The obvious solution to

this problem is to empirically correct the effective masses as a function of quantum confinement energy, and that is the approach taken here. Since most of the quantum confinement is in the conduction band electron, this empirical correction is applied only to the electron effective mass. Applying a correction to the electron effective mass means that the total quantum confinement energy depends on the electron effective mass and vice-versa. It follows that the correction factor to the electron effective mass must be calculated in a way that is self-consistent with the calculated quantum confinement energies. Throughout these calculations, the electron-hole coulombic interaction is treated as a perturbation. We find that the corrected electron effective mass may be given by, $m_e^*(corrected) = m_e^*(bulk)(0.36773 + 2.75634x10^{-4}E_{QC} - 8.3105x10^{-9}E_{QC}^2)$, where E_{QC} is the electron plus hole quantum confinement energy. The way this is implemented is to start out assuming the low energy (bulk) electron effective mass, calculate electron and hole quantum confinement energies, use these quantum confinement energies to get a corrected electron effective mass, and so on. This procedure converges to self-consistent values in a few iterations. This empirical correction is chosen so that the EMA calculations very accurately reproduce the known CdSe sizing curve for particles having exciton wavelengths of 500 – 650 nm.[13]

These calculations are also applied to CdSe/CdS core/shell particles. This extension is non-trivial for two reasons. First, the presence of core/shell lattice mismatch, and second, the possibility of selenium and sulfur interdiffusion. Diffusion is a strongly activated process and appropriate to the low-temperature shell deposition conditions used here, we will initially ignore radial diffusion. The lattice parameter of CdSe is about 4% larger than for CdS, and the core-shell lattice mismatch results in the core being under isotropic pressure and the shell being under radial pressure and tangential tension.[16, 17] These strains affect the respective conduction band energies, which is taken into account through an elastic continuum calculation using the known elastic parameters of each material.[18-20] This calculation gives the volumetric strain as a function of radial position. This result, when combined with the volume dependent conduction band energy shifts, allows calculation of an accurate conduction band radial potential, as was done in reference 21. The valence band potential is much less affected by strain, and is taken to be bulk values. Electron and hole wavefunctions are calculated using these potentials. A crucial parameter in the electron wavefunction calculation is the zero-strain CdSe-CdS conduction band offset, which is estimated to be between 0 and 0.3 eV.[22-24] If this is taken to be 0.047eV and the same electron effective mass correction factor is applied to the CdS conduction band electron, then this EMA calculation also accurately gives the exciton energy of the 6.6 nm core/shell particles, see figures 4-1 and 4-3. This approach has been used to calculate the exciton energies of a wide range of cores sizes and shell thicknesses. A map of the exciton energy as a function of core size and shell thickness is shown in figure 4-4 and in the Supporting Information. The elastic continuum model is not a good approximation for very thin shells, (less than a full monolayer) and calculations for those particles are omitted.

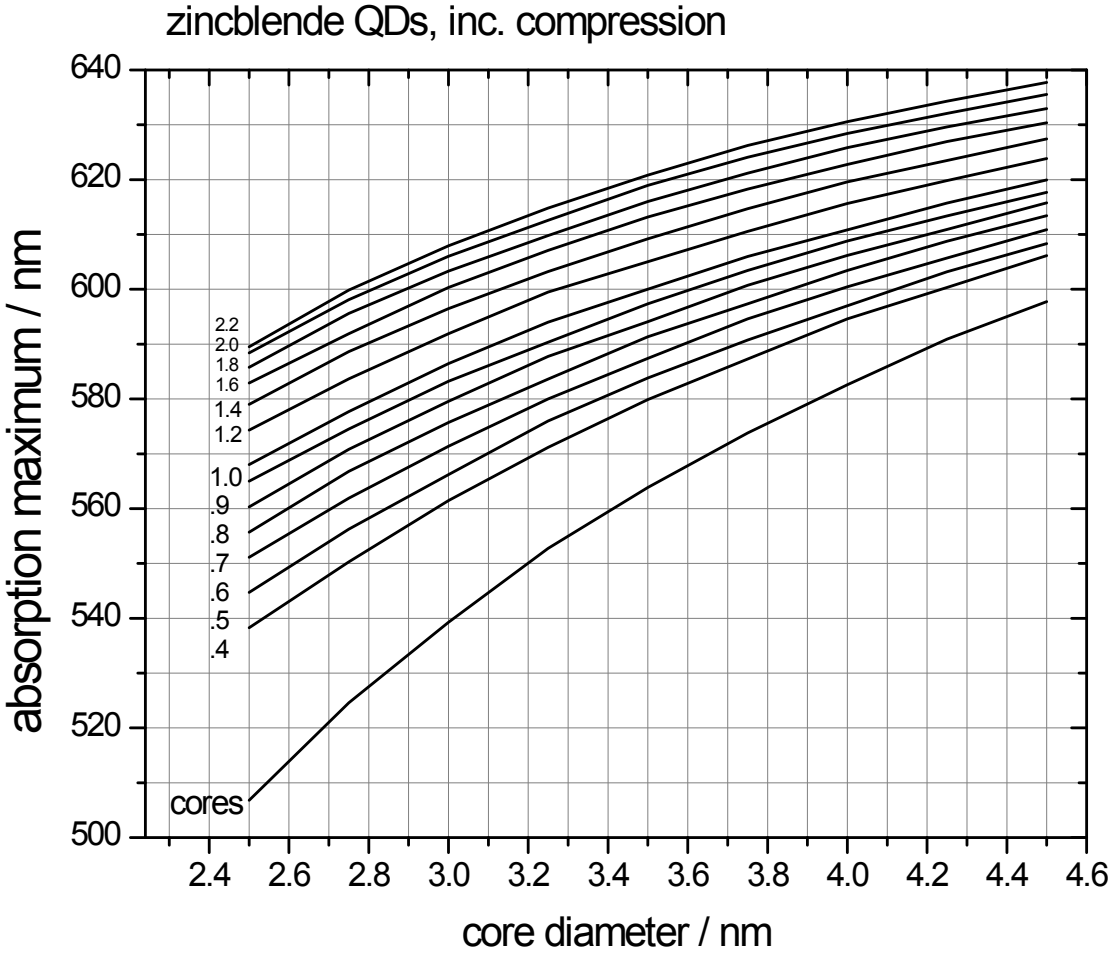

Figure 4-4. Exciton wavelength map assuming no core-shell interdiffusion and core compression calculated with bulk elastic parameters. The calculations assume smooth shells and a coherent core/shell interface.

The map in figure 4-4 assumes both a coherent core-shell interface and a uniform shell thickness, resulting in significant strain-induced spectral shifts. These are good assumptions for the zincblende particles for which the shell has been grown at low temperature. However, much of the lattice strain energy is released upon forming a rough shell and this occurs when thick wurtzite shells are grown at high temperatures and/or subsequently annealed.[9] In addition to relieving much of the lattice strain, high temperature shell deposition and subsequent annealing results in significant radial diffusion of the selenium and sulfur across the core-shell interface. This diffusion has the effect of changing both the conduction and, especially, valence band radial potentials. Thus, the effect of annealing is that the conduction band potential is altered by the graded composition and the loss of volumetric lattice strain. The valence band potential is not greatly affected by volumetric strain, but is affected by the change in composition profile. Valence band energies change nonlinearly with composition, a phenomenon referred to as

"optical band-bowing," and this effect is included in the calculation of the valence band radial potential.[25-27] These considerations are relevant to the results on wurtzite CdSe/CdS particles reported in reference 5. In these studies, the CdS shells were grown at relatively high temperature and subsequently annealed at 200 °C. In contrast, the particles used here are zincblende and with the shells grown at much lower temperatures, <160 °C, and do not readily undergo surface reconstruction. They have more uniform shell thicknesses and are metastable with respect to release of the lattice strain and shell roughening. The present zincblende core/shell particles may therefore be expected to have somewhat different spectroscopic properties than the particles studied in reference 5. Using the same CdSe and CdS valence and conduction band potentials, we have also calculated core/shell exciton wavelengths maps for the case of no core compression, with and without radial interdiffusion. These radial composition profiles are obtained by solving the radial diffusion equation, as explained in reference 21. The valence and conduction band potentials are then calculated, considering the effects of band-bowing. The resulting maps are significantly different that the low temperature zincblende map and are given in the Supporting Information. The map which includes the effects of radial diffusion is most appropriate to high-temperature-synthesized wurtzite core/shell particles of reference 5. We find that if the product of the diffusion coefficient and time is set to 0.03 nm^2, then the resulting map is very similar to that in reference 5, differing in exciton wavelength by at most a few nanometers. Assuming a 1 hour annealing time,[5] this corresponds to a Se-S interdiffusion coefficient of 5 x 10^{-4} nm^2 min^{-1}, which is the same order magnitude as reported for Te-Se interdiffusion reported in reference 21. It is important to note that the map shown in figure 4-4 is not in disagreement with that in reference 5. The two maps are complementary, simply applying to CdSe/CdS particle synthesized under different conditions.

2. Exciton oscillator strengths.

The extinction coefficient spectra in figure 4-1 are obtained from corresponding absorption spectra by scaling the absorbance to the extinction coefficient at a wavelength where the extinction coefficient can be calculated. The scaling assumes Beer's Law, that the absorbance is proportional the extinction coefficient throughout each spectrum. Extinction coefficients are calculated at a wavelength that is sufficiently short that quantum confinement effects are unimportant, in this case, 350 nm. In the case of core/shell particles, the measured absorption at 350 nm may have a contribution from small, homogeneously nucleated CdS particles. Using the present synthesis, this is typically a small contribution (< 10%) and is corrected for by the comparison of the measured absorption and luminescence excitation spectra. The 350 nm extinction coefficients are calculated from the known particle volumes and compositions, using literature values of the 350 nm optical constants for bulk CdSe and CdS. This type of procedure is quite standard and has been shown to give reliable assessments of absolute extinction coefficients.[10, 28-30] The real and imaginary components of the 350 nm complex refractive index for CdSe[28, 31] and CdS[31] are n_{CdSe} = 2.772, k_{CdSe} = 0.7726, and n_{CdS} = 2.58, k_{CdS} = 0.70. The extinction coefficients at λ = 350 nm are given by[13]

$$\varepsilon_{QD}(\lambda) = \frac{2\pi N_A}{0.2303\lambda}\frac{2n_{CdSe}k_{CdSe}}{n_s}\left|f_{LF}\right|^2\left(\tfrac{4}{3}\pi r_c^3 + \frac{n_{CdS}k_{CdS}}{n_{CdSe}k_{CdSe}}\tfrac{4}{3}\pi\left((r_c+h)^3 - r_c^3\right)\right) \quad (5)$$

where r_c is the core radius, h is the shell thickness, λ = 350 nm and f_{LF} is the local field factor. (Equation 5 uses SI units.) The local field factor is given by[13, 32]

$\left|f_{LF}\right|^2 = \frac{9n_s^4}{\left(n_p^2 - k_p^2 + 2n_s^2\right) + 4n_p^2k_p^2}$ where the subscripts p and s refer to the particle and solvent respectively. Evaluation with the CdSe refractive index and chloroform solvent gives a value of $|f_{LF}|^2$ = 0.285 at 350 nm. Equation 5 gives a 350 nm extinction coefficient of 3.57 x 10^5 l $mol^{-1}cm^{-1}$ for the 2.62 nm CdSe core particles. The core absorption spectrum has a 516.6 nm absorbance that is 0.440 that of the 350 nm absorbance, or 1.57 x 10^5 $M^{-1}cm^{-1}$. It is of interest to compare this extinction coefficient to that reported in reference 13 for the same size particles, which is 1.63 x 10^5 $M^{-1}cm^{-1}$. Reference 13 has all of the lowest exciton absorption peaks corrected for inhomogeneous width, to a HWHM of 0.06 eV. Applying the same correction to the spectrum in figure 4-1, we get a 516.6 nm extinction coefficient of 1.68 x 10^5 $M^{-1}cm^{-1}$, which is in close agreement with the value reported in reference 13. This is an important check of the internal consistency of these calculations, and confirms the validity of this approach. Using the literature values of 350 nm absorbance coefficients, $n_{CdS}k_{CdS} / n_{CdSe}k_{CdSe} = 0.84$, equation 5 can also be applied to the core/shell spectra. In all cases, integrated extinction coefficients to be used in the evaluation of equation 1 are obtained from fitting the low energy part of these spectra to a superposition of Gaussian peaks and taking the area of the peak corresponding to the $1S_{3/2}$-$1S_e$ transition.

3. Radiative lifetime calculation.

The radiative lifetimes of the 2.62 nm core, and several core/shell particles having the same CdSe cores and different CdS shell thicknesses have been obtained from time-resolved PL measurements. The PL quantum yields of the core/shell particles are very high (> 80%, and usually about 95%) and the PL decays are dominated by a slow component that is taken to be the radiative lifetime. These lifetimes decrease with increasing shell thickness and exciton wavelength, as shown in figure 4-5. The longest decay component for the core particles is also shown. However, the quantum yield of the core particles is low and the radiationless decay may shorten this decay, compared to the actual radiative lifetime. As such, the measured value of 44.5 ns must be viewed as a lower limit on the actual radiative lifetime. We note that the radiative lifetime decreases with increasing shell thickness and exciton wavelength. This is analogous to what is observed in bare CdSe core particles (where the radiative lifetime decreases with particle size), and the opposite of what is observed in type-II QDs, such as CdTe/CdSe.[10]

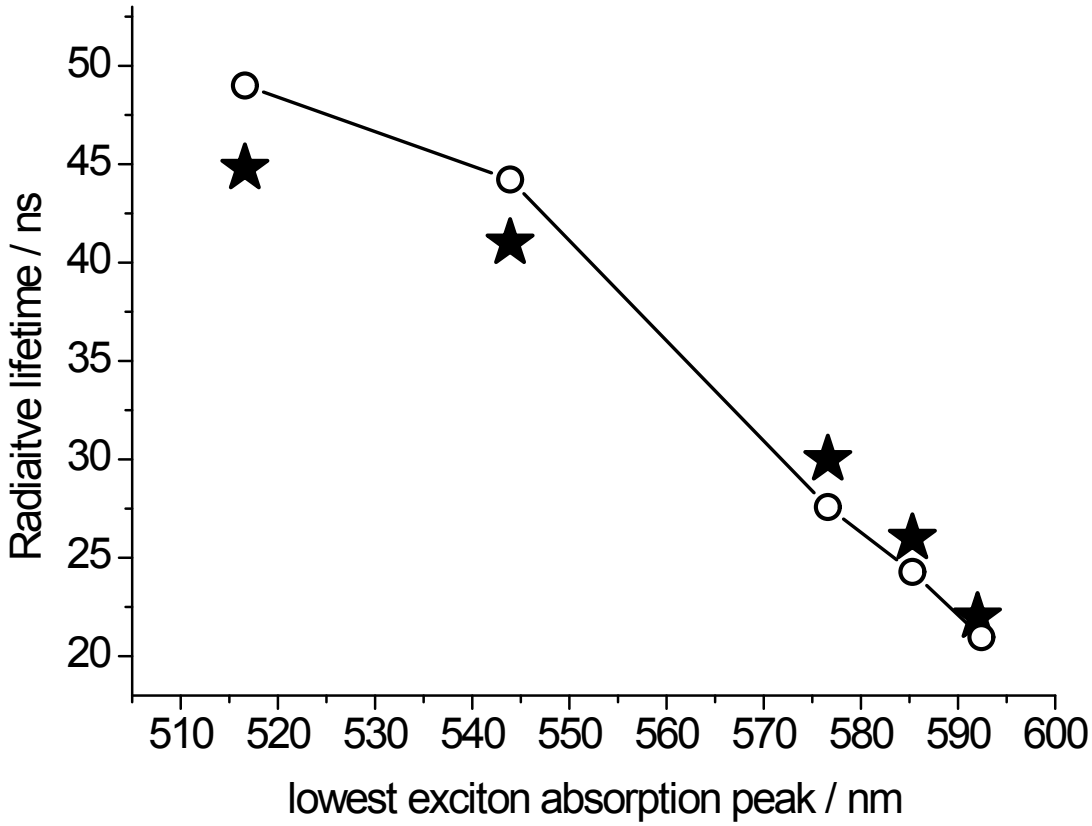

Figure 4-5. Radiative lifetime as a function of the wavelength of the lowest energy exciton in CdSe/CdS particles. The open circles correspond to radiative lifetimes calculated as described in the text. The 2.64 nm zincblende cores (the 516.6 nm point) have a low QY and the measured lifetime is unreliable.

It is of interest to use equation 1 to compare the measured radiative lifetimes to values calculated from the spectra in figure 4-1. Although the PL energies and integrated extinction coefficients are easily obtained from figure 4-1, obtaining accurate C_{fs} values is more complicated. Calculation of C_{fs} amounts to calculating the splittings between the dark and bright angular momentum sublevels[33] and the thermal populations in these sublevels as a function of shell thickness. This calculation also considers the population in the $1P_{3/2}$ hole level, which has only a slight effect.[10, 34] We take the dark-bright splitting to be dominated by the electron-hole exchange interaction, which scales as the reciprocal of the electron-hole separation, 1/r. The electron and hole wave functions calculated to obtain the exciton energy map in figure 4-4 are also used to calculate expectation values of 1/r. These expectation values are obtained by a straight-forward numerical integration over the wavefunctions.[35] Relative 1/r expectation values are used to obtain relative values of E_i compared to those in the core, which are taken from Efros et al.[33] Equation 1 is readily evaluated by using values of C_{fs} obtained from equation 4, the integrated extinctions coefficients, and the exciton energies. A plot of these radiative lifetimes is

also shown in figure 4-5. Very good agreement with the measured decays is obtained for all but the bare CdSe core particles. This may be understood in terms of the fact that the core particles exhibit a lower QY and the long decay component therefore does not reliably give the radiative lifetime. We note that core radiative lifetime is calculated to be 49 ns, in quantitative agreement with the previously reported value for wurtzite QDs.[10]

It should be noted that this calculational approach uses only the observed spectra and literature data; the calculation of the radiative lifetime has no adjustable parameters. The integrated extinction coefficients of the core/shell particles are obtained directly from the static absorption spectra and the known 350 nm optical constants. The values of C_{fs} for the appropriate sized core particles are from results reported by Efros et al.,[33] and values for the core/shell particles are calculated using calculated expectation values of 1/r. All of the calculated results are in good agreement with radiative lifetimes obtained from time-correlated photon-counting measurements. The Einstein relations (of course) very accurately predict radiative lifetimes. One of the conclusions of this study is very simple: these equations very accurately predict the radiative lifetimes, but only when careful measurements are made and all of the appropriate quantities are correctly evaluated.

These results show that the radiative lifetimes decrease with shell thickness, similar to the size dependence of one-component CdSe quantum dots.[10] This observation is in sharp contrast to what is reported in type-II core/shell QDs, such as CdTe/CdSe.[21] The difference is primarily a result of how the electron-hole overlap varies with shell thickness. In the present case of CdSe/CdS, the band offsets are referred to as type-1½, where the hole is localized in the core and the electron is delocalized throughout the core and shell. Despite the electron delocalization, there remains considerable electron-hole overlap for even rather thick shells. For example, the in the case of the 2.0 nm thick shells, the electron hole overlap is calculated to be $\left|\left\langle \Psi_e \mid \Psi_h \right\rangle\right|^2 = 0.31$. In type-II QDs such as CdTe/CdSe, the band offsets are such that the hole is localized in the core and the electron is localized in the shell. The result is that increasing shell thickness causes the electron-hole overlap to decrease much more rapidly in the type-II, compared to type-1½ QDs. This puts less of the oscillator strength in the $1S_h$-$1S_e$ transition for the type-II QDs, resulting in longer radiative lifetimes.

XV. EXPERIMENTAL METHODS

XV.1 Optical measurements

In the time resolved photoluminescence studies, samples were excited with very low intensity 410 nm pulses at 1 MHz from a cavity-dumped frequency-doubled Coherent MIRA laser. The luminescence was imaged through a ¼ m monochromator with a 150 groove/mm grating onto a Micro Photon Devices PDM 50CT SPAD detector. TCPC decays are accumulated using a Becker-Hickle SPC-630 board. The overall temporal response function of the system is about 70 ps.

Quantum yield measurements were made using the same samples as the time resolved luminescence measurements. The static luminescence spectra were measured on a Jobin-Yvon Fluorolog 3 with a CCD detector. Sample spectra were compared with spectra of R6G (assumed to have a 95% QY) taken with the same excitation wavelength and the same absorbance at that wavelength. The wavelength dependence of the CCD detector was taken into account in calculating the nanoparticle quantum yield. This was done by measuring the spectrum of a calibrated tungsten lamp and constructing a detector sensitivity curve.

Chemicals.

Cadmium oxide (CdO, 99.5%), octadecylamine (ODA, 90%), oleylamine (technical grade, 70%), octylamine (99%), sodium diethyldithiocarbamate trihydrate ($NaDDTC \cdot 3H_2O$), cadmium acetate dihydrate ($Cd(Ac)_2 \cdot 2H_2O$), tellurium (Te, 99.8%), trioctylphosphine (TOP, 97%), tributylphosphine (TBP, 97%), octadecene (ODE, 90%), hexane (99.8%), methanol (MeOH, 98%), and toluene (99%) were obtained from Aldrich. Selenium (Se, 99%), oleic acid (OA, 90%), n-octane (98+%) and chloroform ($CHCl_3$, 99.8%) were obtained from Alfa Aesar. ODA was recrystallized from toluene before use. TOP, TBP, and ODE were purified by vacuum distillation. TOPO was purified by repeated recrystallization from acetonitrile. Methanol, chloroform and toluene were purified by distillation from appropriate drying agents. All other chemicals were used as received.

XV.2 Synthesis and sample preparation

The zincblende CdSe core nanocrystals are synthesized and purified using slightly modified procedures reported by Nan et al.[2] Zincblende shell deposition occurs from a cadmium-sulfur single precursor, cadmium diethyldithiocarbamate ($Cd(DDTC)_2$), at low temperature (140 - 145 °C). In a typical synthesis, CdO (0.256 g, 0.2 mmol), oleic acid (1 mL) and 4 mL ODE were loaded into a 25 mL three-neck flask. After N_2 bubbling for 2 min, the flask was heated to 250 °C to form a transparent solution and then cooled to 40 °C. Se powder (0.0079 g, 0.1 mmol) was loaded into the flask. The flask was heated to 240 °C under N_2 flow at a heating rate of 40 °C/min. Needle tip aliquots were taken for UV−vis and PL measurements to monitor the size of zincblende CdSe QDs. The particles are then purified by repeated extraction. In these extractions, tributylphosphine (0.2 mL), octylamine (0.2 mL), hexane (3 mL), and methanol (6 mL) were added to the reaction solution at 50 °C and stirred for 2 min. After stirring

was turned off, the colorless methanol layer was separated from the top ODE/hexane layer by syringe. This extraction procedure was repeated three times, but TBP was added only the first time. The remaining hexane in the ODE layer was removed by nitrogen bubbling at about 60 °C.

Subsequent CdS shell growth requires the synthesis of ($Cd(DDTC)_2$) for use as the single cadmium and sulfur precursor. In this synthesis, $Cd(Ac)_2 \cdot 2H_2O$ (10 mmol) was dissolved with 100 mL of distilled water in a 400 mL beaker. Into this solution, $NaDDTC \cdot 3H_2O$ (20 mmol) dissolved in 60 mL of distilled water was added dropwise under vigorous stirring. A white precipitate of $Cd(DDTC)_2$ quickly forms. The mixture was stirred for another 20 min after mixing to ensure the reaction was complete. The white precipitate was separated from the solution phase by filtration and washed three times with distilled water. The final product in white powder form was obtained by drying under vacuum overnight. For each shell growth reaction, a 3 mL $Cd(DDTC)_2$-amine-octane solution (0.1 mmol/mL) was prepared by dissolving 0.1227 g of $Cd(DDTC)_2$ in a mixture of octane (1.5 mL), oleylamine (0.45 mL), and octylamine (1.05 mL).

In a typical CdS shell growth reaction, a mixture of ODE (2.0 mL), ODA (20 mg), and oleylamine (1.0 mL) was heated to 60 °C in a three-neck flask under argon flow, and then about 1.0 mL of purified CdSe core solution (containing about 1×10^{-7} mol of nanocrystals estimated by their extinction coefficients) was added to this flask. The amount of precursor solution for each injection was estimated using standard SILAR procedure. In this reaction cycle, addition of the CdS precursor solution is done at 80 °C and growth occurs by heating the solution at a targeted temperature (140 °C for typical synthesis) for about 10 min. This inject-heat-cool cycle was repeated until the desired number of CdS monolayers was obtained. The final reaction solution is purified by extraction with hexane/methanol (v:v~1:1) twice. The non-polar layer is separated and heated under vacuum to remove the residual hexane and methanol. The dried sample is then dissolved in octadecene and ligand exchanged with excess TBP and ODA at 100 °C for about an hour. After ligand exchange, the sample is centrifuged and liquid layer is kept. The particles are precipitated by the addition of anhydrous methanol, dried under vacuum then dispersed in toluene or chloroform for the spectroscopic measurements.

---

[1] Ghosh, Y.; Mangum, B. D.; Casson, J. L.; Williams, D. J.; Htoon, H.; Hollingsworth, J. A., New Insights into the Complexities of Shell Growth and the Strong Influence of Particle Volume in Nonblinking "Giant" Core/Shell Nanocrystal Quantum Dots. *J. Am. Chem. Soc.* **2012,** 134, 9634−9643.

[2] Nan, W.; Niu, Y.; Qin, H.; Cui, F.; Yang, Y.; Lai, R.; Lin, W.; Peng, X., Crystal Structure Control of Zinc-Blende CdSe/CdS Core/Shell Nanocrystals: Synthesis and Structure-Dependent Optical Properties. *J. Am. Chem. Soc.* **2012,** 134, 19685−19693.

[3] Embden, J.; Jasieniak, J.; Gómez, D. E.; Mulvaney, P.; Giersig, M., Review of the Synthetic Chemistry Involved in the Production of Core/Shell Semiconductor Nanocrystals. *Aust. J. Chem.* **2007** 60, 457

[4] Li, J. J.; Wang, Y. A.; Guo, W.; Keay, J. C.; Mishima, T. D.; Johnson, M. B.; Peng, X., Large-Scale Synthesis of Nearly Monodisperse CdSe/CdS Core/Shell Nanocrystals Using Air-Stable Reagents via Successive Ion Layer Adsorption and Reaction. *J. Am. Chem. Soc.* **2003,** 125, 12567.

[5] Embden, J. v.; Jasieniak, J.; Mulvaney, P., Mapping the Optical Properties of CdSe/CdS Heterostructure Nanocrystals: The Effects of Core Size and Shell Thickness. *J. Am. Chem. Soc.* **2009,** 131, 14299.

[6] García-Santamaría, F.; Chen, Y.; Vela, J.; Schaller, R. D.; Hollingsworth, J. A.; Klimov, V. I., Suppressed Auger Recombination in "Giant" Nanocrystals Boosts Optical Gain Performance. *Nano Lett.* **2009,** 2, 3482.

[7] Guo, Y.; Marchuk, K.; Sampat, S.; Abraham, R.; Fang, N.; Malko, A. V.; Vela, J., Unique Challenges Accompany Thick-Shell CdSe/nCdS (n > 10) Nanocrystal Synthesis. *J. Phys. Chem. C* **2012,** 116, 2791-2800.

[8] Smith, A. M.; Mohs, A. M.; Nie, S., Tuning the optical and electronic properties of colloidal nanocrystals by lattice strain. *Nature Nanotechnology* **2009,** 4, 56 - 63.

[9] Gong, K.; Kelley, D. F., A Predictive Model of Shell Morphology in CdSe/CdS Core/Shell Quantum Dots. *J. Chem. Phys.* **2014**, in press.

[10] Gong, K.; Zeng, Y.; Kelley, D. F., Extinction Coefficients, Oscillator Strengths, and Radiative Lifetimes of CdSe, CdTe, and CdTe/CdSe Nanocrystals. *J. Phys. Chem. C* **2013,** 117, 20268-20279.
[11] Kelley, A. M., *Condensed-Phase Molecular Spectroscopy and Photophysics*. Wiley: Hoboken, NJ, 2013.
[12] Strickler, S. J.; Berg, R. A., Relationship between Absorption Intensity and Fluorescence Lifetime of Molecules. *J. Chem. Phys.* **1962,** 37, 814 - 822.
[13] Jasieniak, J.; Smith, L.; Embden, J. v.; Mulvaney, P.; Califano, M., Re-examination of the Size-Dependent Absorption Properties of CdSe Quantum Dots. *J. Phys. Chem. C* **2009,** 113, 19468 - 19474.
[14] Yu, P. Y.; Cardona, M., *Fundamentals of Semiconductors*. third ed.; Springer: Berlin, 2001.
[15] Norris, D. J., Electronic Structure in Semiconductor Nanocrystals: Optical Experiment. In *Nanocrystal Quantum Dots*, 2'd ed.; Klimov, V. I., Ed. CRC Press: 2010.
[16] Saada, A. S., *Elasticity Theory and Applications*. Permagon Press: New York, 1974.
[17] Rockenberger, J.; Troger, L.; Rogach, A. L.; Tischer, M.; Grundmann, M.; Eychmuller, A.; Weller, H., The contribution of particle core and surface to strain, disorder and vibrations in thiol-capped CdTe nanocrystals. *J. Chem. Phys.* **1998,** 108, (18), 7807-7815.
[18] West, A. R., *Basic Solid State Chemistry*. Wiley Chichester, 1988.
[19] Shan, W.; Walukiewicz, W.; Ager, J. W., III; Yu, K. M.; Wu, J.; Haller, E. E., Pressure dependence of the fundamental band-gap energy of CdSe. *Appl. Phys. Lett.* **2004,** 84, (1), 67-69.
[20] San-Miguel, A.; Polian, A.; Itie, J. P.; Marbuef, A.; Triboulet, R., Zinc Telluride Under High Pressure: An X-Ray Absorption Study. *High Pressure Research* **1992,** 10, 412.
[21] Cai, X.; Mirafzal, H.; Nguyen, K.; Leppert, V.; Kelley, D. F., The Spectroscopy of CdTe/CdSe type-II Nanostructures: Morphology, Lattice Mismatch and Band-Bowing Effects. *J. Phys. Chem. C* **2012,** 116, 8118 - 8127.
[22] Talapin, D. V.; Koeppe, R.; Gtzinger, S.; Kornowski, A.; Lupton, J. M.; Rogach, A. L.; Benson, O.; Feldmann, J.; Weller, H., Highly Emissive Colloidal CdSe/CdS Heterostructures of Mixed Dimensionality. *Nano Letters* **2003,** 3, 1677.
[23] Steiner, D.; Dorfs, D.; Banin, U.; Della Sala, F.; Manna, L.; Millo, O., Determination of Band Offsets in Heterostructured Colloidal Nanorods Using Scanning Tunneling Spectroscopy. *Nano Lett.* **2008,** 8, 2954.
[24] Wu, K.; Rodrıguez-Cordoba, W. E.; Liu, Z.; Zhu, H.; Lian, T., Beyond Band Alignment: Hole Localization Driven Formation of Three Spatially Separated Long-Lived Exciton States in CdSe/CdS Nanorods. *ACS Nano* **2013,** 7, 7173.
[25] Bailey, R. E.; Nie, S., Alloyed Semiconductor Quantum Dots: Tuning the Optical Properties without Changing the Particle Size. *J. Am. Chem. Soc.* **2003,** 125, 7100.
[26] Regulacio, M. D.; Han, M.-Y., Composition-Tunable Alloyed Semiconductor Nanocrystals. *Acc. Chem. Res.* **2010,** 43, 621–630.
[27] Wei, S.-H.; Zhang, S. B.; Zunger, A., First-principles calculation of band offsets, optical bowings, and defects in CdS, CdSe, CdTe, and their alloys. *J. Appl. Phys* **2000,** 87, 1304.
[28] Leatherdale, C. A.; Woo, W.-K.; Mikulec, F. V.; Bawendi, M. G., On the Absorption Cross Section of CdSe Nanocrystal Quantum Dots *J. Phys. Chem. B.* **2002,** 106, 7619 - 7622.
[29] Capek, R. K.; Moreels, I.; Lambert, K.; Muynck, D. D.; Zhao, Q.; Tomme, A. V.; Vanhaecke, F.; Hens, Z., Optical Properties of Zincblende Cadmium Selenide Quantum Dots. *J. Phys. Chem. C* **2010,** 114, 6371 - 6376.
[30] de Mello Donega, C.; Koole, R., Size Dependence of the Spontaneous Emission Rate and Absorption Cross Section of CdSe and CdTe Quantum Dots. *J. Phys. Chem. C* **2009,** 113, 6511 - 6520.
[31] Palik, E. D., *Handbook of Optical Constants of Solids*. Academic Press: 1998; Vol. II.
[32] Ricard, D.; Chanassi, M.; Schanne-Klein, M., Dielectric confinement and the linear and nonlinear optical properties of semiconductor-doped glasses. *Opt. Commun.* **1996,** 108, 311.
[33] Efros, A. L.; Rosen, M.; Kuno, M.; Nirmal, M.; Norris, D. J.; Bawendi, M., Band-edge exciton in quantum dots of semiconductors with a degenerate valence band: Dark and bright exciton states. *Phys. Rev. B* **1996,** 54, 4843 - 4856.
[34] Efros, A. L.; Rosen, M., Quantum size level structure of narrow-gap semiconductor nanocrystals: Effect of band coupling. *Phys. Rev. B* **1998,** 58, 7120 - 7135.
[35] Jackson, *Classical Electrodynamics*. 2'd ed.; Wiley: New York, 1975.

CHAPTER 5: AN ATOMISTICALLY VALIDATED CONTINUUM MODEL FOR STRAIN RELAXATION AND MISFIT DISLOCATION FORMATION

X. W. Zhou[1], D. K. Ward[2], J. A. Zimmerman[1], J. L. Cruz-Campa[3], and D. Zubia[4], J. E. Martin[5], and F. B. van Swol[6]

[1]Mechanics of Materials Department
Sandia National Laboratories
Livermore, California 94550, USA

[2]Radiation and Nuclear Detection Materials and Analysis Department
Sandia National Laboratories
Livermore, California 94550, USA

[3] MEMS Technologies Department
Sandia National Laboratories
Albuquerque, New Mexico 87185, USA

[4]Department of Electrical Engineering
University of Texas at El Paso
El Paso, Texas 79968, USA

[5]Nanoscale Sciences Department
Sandia National Laboratories
Albuquerque, New Mexico 87185, USA

[6] Computational Materials and Data Science Department
Sandia National Laboratories
Albuquerque, New Mexico 87185, USA

ABSTRACT

A new continuum model of misfit dislocation formation that improves over the traditional model has been developed. This is achieved by developing a robust molecular dynamics (MD) approach that can confidently validate the continuum model. We find that the enabling techniques to make this possible are (a) the calculations of time averaged properties using very long time MD simulations, which produce significantly more accurate results than molecular statics simulations, and (b) the use of dislocation dipole configurations under periodic boundary conditions, which allows dislocation energies to be exactly calculated. Using these techniques, we are able to accurately determine dislocation core radius and energy without imposing continuum boundary conditions that must be assumed in previous MD approaches to avoid the effects of truncating long-range dislocation stress fields. The total dislocation energy as a function of system sizes and dislocation spacing predicted from the MD is in very good agreement with the continuum theory. Detailed study reveals that the traditional misfit dislocation model can become inaccurate for systems with large lattice mismatch. We then propose improvements of the theory, including a more accurate treatment of dislocation energies,

an incorporation of elastic inhomogeneity from the film and the substrate, and an identification of precise definitions of dislocation spacing and Burgers vector which were likely incorrectly applied in previous work. We show that the prediction from the modified continuum model is essentially indistinguishable from the MD results.

ACKNOWLEDGEMENTS

Sandia National Laboratories is a multi-program laboratory managed and operated by Sandia Corporation, a wholly owned subsidiary of Lockheed Martin Corporation, for the US Department of Energy's National Nuclear Security Administration under contract DE-AC04-94AL85000. This work was performed under a DOE Project No. EE0005859-2013Q3 and under a Laboratory Directed Research and Development (LDRD) project.

XVI. INTRODUCTION

Control of strain relaxation and misfit dislocation is a key material issue for electronic devices [45]. Continuum calculations have been effective in guiding material synthesis experiments [46,47,48,49,50,51,52,53]. As modern devices are driven towards smaller dimensions, larger lattice mismatches, and lower defect tolerances, the requirement for the accuracy of continuum predictions becomes increasingly demanding. Continuum models inherently involve a number of approximations. First, most continuum theories neglect dislocation cores. While this can be easily corrected, it requires prior knowledge of the dislocation core energy, which is often unavailable. Second, the continuum theories are often based on linear elasticity, where the elastic constants under tension and compression are assumed to be the same. In reality, however, materials tend to exhibit larger elastic constants under compression than under tension, especially at large strains. Third, the Burgers vector of a misfit (edge) dislocation is essentially associated with the thickness of the half planes removed or inserted. However, inserting a half plane to the film is exactly equivalent to removing a half plane from the substrate. As a result, ambiguity arises whether the Burgers vector should be defined by the film lattice constant or the substrate lattice constant. This problem has not been clarified in previous continuum models. Fourth, the conventional continuum misfit dislocation theories typically use only the elastic properties of the film but not the substrate. While it is possible to incorporate the elastic properties of both film and substrate using more complex theories [46], the simple model can still be accurate as long as the effects of the simplification are determined and corrected. Finally, the continuum misfit dislocation energy expressions can often be significantly simplified through approximations. The construction of an optimum continuum model then requires knowing the accuracy of the approximations, which in turn requires validation from either experiments or simulations at a more fundamental level.

Molecular dynamics (MD) simulations provide an alternative approach to study strain relaxation and misfit dislocation formation. However, practical devices usually have dimensions beyond 100 nm. At such dimensions, MD models are not efficient for generating enough understanding to impact device design and synthesis. On the other hand, MD models do not suffer from the limitations of continuum models. As a result, MD simulations can determine the unknown parameters and access the accuracy of various continuum theory approximations. The insights gained can then lead to improvements of the continuum models. However, this requires that consistent results be achieved from the continuum and MD methods for the same system geometries and dimensions.

---

45 R. M. Farrell, E. C. Young, F. Wu, S. P. DenBaars, and J. S. Speck, Semicond. Sci. Technol., 27, 024001 (2012).
46 J. W. Matthews, and A. E. Blakeslee, J. Crystal Growth, 27, 118 (1974).
47 W. D. Nix, Metall. Trans. A, 20, 2217 (1989).
48 J. R. Willis, S. C. Jain, and R. Bullough, Phil. Mag. A, 62, 115 (1990).
49 X. Feng, and J. P. Hirth, J. Appl. Phys., 72, 1386 (1992).
50 J. P. Hirth, and X. Feng, J. Appl. Phys., 67, 3343 (1990).
51 S. C. Jain, T. J. Gosling, J. R. Willis, R. Bullough, and P. Balk, Solid-State Electron., 35, 1073 (1992).
52 T. J. Gosling, J. R. Willis, R. Bullough, and S. C. Jain, J. Appl. Phys., 73, 8297 (1993).
53 U. Jain, S. C. Jain, J. Nijs, J. R. Willis, R. Bullough, R. P. Mertens, and R. van Overstraeten, Solid-State Electron., 36, 331 (1993).

Two obvious issues prevent MD from matching the continuum models. First, dislocation energy is essentially the energy difference between a system containing a dislocation and a system without a dislocation. In atomistic models, an edge dislocation is created by removing (or inserting) extra half planes. This means that systems with and without a misfit dislocation necessarily have different numbers of atoms. As a result, the dislocation energy is not simply the energy difference between the two systems. Periodic boundary conditions, however, allow for an accurate calculation of dislocation energy. Under periodic boundary conditions, every atom in a dislocation-free system is equivalent. The energy of the dislocation-free system can then be scaled to the same number of atoms in a system containing a dislocation. Unfortunately, the periodic boundary conditions prohibit the creation of a single dislocation. This paper seeks to address this problem by studying dislocation dipole configurations instead of isolated dislocations. Note that the particular dislocation configuration is not important as long as it can be studied in both MD and continuum models to enable the connection. The second problem is that the conventional atomistic methods typically apply molecular statics (MS) energy minimization to calculate the equilibrium properties (e.g., energy) of relaxed systems. As will be shown below, MS simulations do not yield unique minimum energy results when the system is big and contains dislocations. This is because large systems numerically mitigate the resolution for small energy changes while the presence of a dislocation allows the system to relax to many different local energy minima. This paper seeks to address this problem by calculating time-averaged properties using long time MD simulations, which would statistically cancel out numerical errors and at the same time allow different energy minima to be sampled. Clearly, highly converged results can theoretically always be achieved by increasing the averaging time. MD simulations have an additional advantage as they incorporate finite temperatures whereas the MS data pertains only to 0 K.

This work will perform systematic studies to explore the ideas described above to construct an MD validated continuum misfit dislocation model. The validated model can then lead to improved understanding of strain relaxation and misfit dislocation formation. For simplicity and without losing generality, our studies will assume a quasi- two-dimensional (2D) geometry. This simply means that the system is under a plane strain condition $\square_{zz}\square = \square_{xz}\square = \square_{yz}\square = 0$, with the film/substrate interface on the x-z plane and film thickness in the y direction. In such systems, strain relaxation only occurs in the x direction, where misfit dislocations lie in the z direction and periodically form along the x direction.

XVII. DERIVATION OF MISFIT DISLOCATION ENERGY EXPRESSION

The equilibrium energy theory [44,54,55,56] of strain relaxation and misfit dislocation

formation was summarized elegantly by Nix [45] in 1989, which was later improved by Willis and others [46,57,58]. Here for clarity of illustration, we will use Nix's model. Applying Nix's equation to the 2D geometry of a lattice mismatched film containing misfit dislocations the energy (per unit of interface area) can be expressed as

$$E_s = \frac{1}{2}\frac{2G_f h}{(1-\nu_f)}\cdot\left(\varepsilon - \frac{b_f}{S}\right)^2 + \frac{G_f b_f^2}{4\pi(1-\nu_f)}\frac{1}{S}\ln\left(\frac{\beta\cdot h}{b_f}\right) \quad (1)$$

where G, □, and b are respectively, shear modulus, Poisson's ratio and magnitude of the Burgers vector for a misfit dislocation (the subscript f standing for film), S is the spacing between dislocations, h is film thickness, □ is a constant, and □ is the lattice mismatch parameter that can be defined by the lattice constants of film (a_f) and substrate (a_s) as □ = (a_s-a_f)/a_f. Note that in Eq. (1), $\frac{2G_f}{(1-\nu_f)}$ represents the apparent Young's modulus under our plane strain condition $\varepsilon_{xx} \neq 0$, $\varepsilon_{yy} \neq 0$, $\varepsilon_{zz} = \gamma_{xz} = \gamma_{yz} = 0$, and $\sigma_{yy} = 0$. Also note that Eq. (1) differs from Nix expression [45] by a factor of two because we assume a 2D problem whereas his problem is three-dimensional (3D). To understand the physical origins of the theory that is essential for improving the model, we now give a rigorous derivation of Eq. (1).

As in previous continuum models, we assume that the substrate is much thicker than the film. In such a case, the substrate is "rigid" whereas a dislocation-free film must be strained by exactly □ to match the dimension of the substrate. Assume that in a dislocation-free system, n_f planes of film with plane spacing b_f are matched with n_f planes of substrate with plane spacing b. If the substrate is rigid, then the film is subject to a strain of $(n_f b - n_f b_f)/(n_f b_f) = (b - b_f)/b_f = (a_s - a_f)/a_f = \varepsilon$. If a half plane is inserted to the film, then the film is subject to a strain of $[n_f b - (n_f+1)b_f]/[(n_f+1)b_f] = \varepsilon - b/S_f$, where $S_f = (n_f+1)b_f$ is the total length of unstrained film per dislocation (i.e., dislocation spacing). On the other hand, if a half plane is removed from the substrate, then the film is subject to a strain of $[(n_f-1)b - n_f b_f]/(n_f b_f) = \varepsilon - b/S_f$, where $S_f = n_f b_f$ is again the total length of unstrained film per dislocation. This means that regardless if it is viewed as inserting a half plane in the film or removing a half plane from the substrate, a dislocation always causes a consistent strain of $-b/S_f$. By comparing to the first term on the right side of Eq. (1), we see that Eq. (1) inaccurately defines the magnitude of the Burgers vector to be the film value b_f rather than the substrate value b, and dislocation spacing to be the system (or substrate) value S rather than the film value S_f. When the film and substrate dimensions are close, this may not cause significant errors, otherwise Eq. (1) may become inaccurate.

The equilibrium energy theory essentially defines how system energy changes when an array of misfit edge dislocations form at the film/substrate interface. Energy expressions involving dislocation arrays can be quite difficult to derive directly from stress/strain fields. One

---

54 J. H. van der Merwe, J. Appl. Phys., 34, 123 (1963).
55 J. W. Matthews, and A. E. Blakeslee, J. Crystal Growth, 29, 273 (1975).
56 J. W. Matthews, J. Vac. Sci. Technol., 12, 126 (1975).
57 S. C. Jain, T. J. Gosling, J. R. Willis, D. H. J. Totterdell, and R. Bullough, Phil. Mag. A, 65, 1151 (1992).
58 S. C. Jain, A. H. Harker, and R. A. Cowley, Phil. Mag. A, 75, 1461 (1997).

easier approach is to write out the energy expression in terms of the work done to move dislocations:

$$E_{final} = E_{initial} + w = E_{initial} + \int_{initial}^{final} f_s \cdot ds \tag{2}$$

where E_{final} and $E_{initial}$ are system energies when dislocations are in the final and initial locations, f_s is force exerted on dislocations along the direction s in which dislocations are moved, the work w is represented by the integration over the entire distance moved. Prior to deriving our model for the misfit dislocation energy expression, we first show two examples of employing Eq. (2).

First, let us imagine that one positive and one negative edge dislocations lie exactly on top of each other, as shown in Fig. 5-1(a). This is essentially a dislocation-free scenario so that the initial energy $E_{initial}$ equals zero. Now we move the upper dislocation to a distance 2R away as shown in Fig. 5-1(b), where R represents the maximum range of the strain field of a dislocation so that 2R would mean that the R regions of the two dislocations do not overlap so that they can be viewed as isolated dislocations. If the attractive force between the two dislocations is denoted as f_x, Eq. (2) indicates that the final energy E_{final} for moving the two dislocations from separation distance x = 0 to x = 2R equals $E_{final} = \int_0^{2r_0} f_x \cdot dx + \int_{2r_0}^{2R} f_x \cdot dx$, where r_0 represents dislocation core radius so that $x \geq 2r_0$ would mean that dislocation cores do not overlap. In classical continuum theory, $\int_0^{2r_0} f_x \cdot dx$ represents core energies of two dislocations so that $\int_0^{2r_0} f_x \cdot dx = 2E_c$, where E_c is core energy per dislocation. For $x \geq 2r_0$, the attractive force f_x equals $\frac{Gb^2}{2\pi(1-\nu)}\frac{1}{x}$ [59]. Hence, $E_{final} = 2E_c + \int_{2r_0}^{2R} \frac{Gb^2}{2\pi(1-\nu)}\frac{1}{x} \cdot dx = 2E_c + \frac{Gb^2}{2\pi(1-\nu)} \ln\left(\frac{R}{r_0}\right)$. Consider that E_{final} accounts for energies of two dislocations, each dislocation gets an energy of $\Gamma_0 = E_c + \frac{Gb^2}{4\pi(1-\nu)} \ln\left(\frac{R}{r_0}\right)$. This energy is consistent with the classical derivation of the total strain energy within a distance R from an isolated edge dislocation [61].

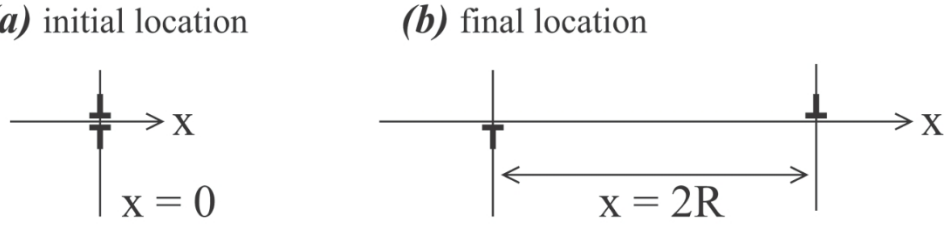

Figure 5-1. Illustration of work for separating a pair of opposite dislocations: (a) initial and (b) final dislocation locations.

[59] D. Hull, and D. J. Bacon, Introduction to dislocations, 4th Ed. (Butterworth-Heinemann, Oxford, 2001).

In the second example, we imagine that two positive edge dislocations are widely separated at r = 2R so that each can be considered as an isolated dislocation with an energy of $\Gamma_0 = E_c + \frac{Gb^2}{4\pi(1-\nu)}\ln\left(\frac{R}{r_0}\right)$ as demonstrated above. In this case, the initial energy $E_{initial} = 2\Gamma_0 = 2E_c + \frac{Gb^2}{2\pi(1-\nu)}\ln\left(\frac{R}{r_0}\right)$. The repulsive force between the two dislocations is $f = \frac{Gb^2}{2\pi(1-\nu)}\frac{1}{x}$. Following Eq. (2), the final energy E_{final} for moving the two dislocations from x = 2R to x = 0 equals $E_{final} = 2E_c + \frac{Gb^2}{2\pi(1-\nu)}\ln\left(\frac{R}{r_0}\right) - \int_{2R}^{2r_0}\frac{Gb^2}{2\pi(1-\nu)}\frac{1}{x}\cdot dx - \int_{2r_0}^{0} f_x \cdot dx = 4E_c + \frac{Gb^2}{\pi(1-\nu)}\ln\left(\frac{R}{r_0}\right)$. Note that unlike the first case where f_x is attractive, here f_x is repulsive so that $\int_{2r_0}^{0} f_x \cdot dx = -2E_c$. When the two positive edge dislocations overlap on top of each other at r = 0, they merge into one dislocation with the burgers vector doubled. According to the classical expression [61], dislocation energy is proportional to b^2. Hence the dislocation energy derived from the work again matches the classical theory.

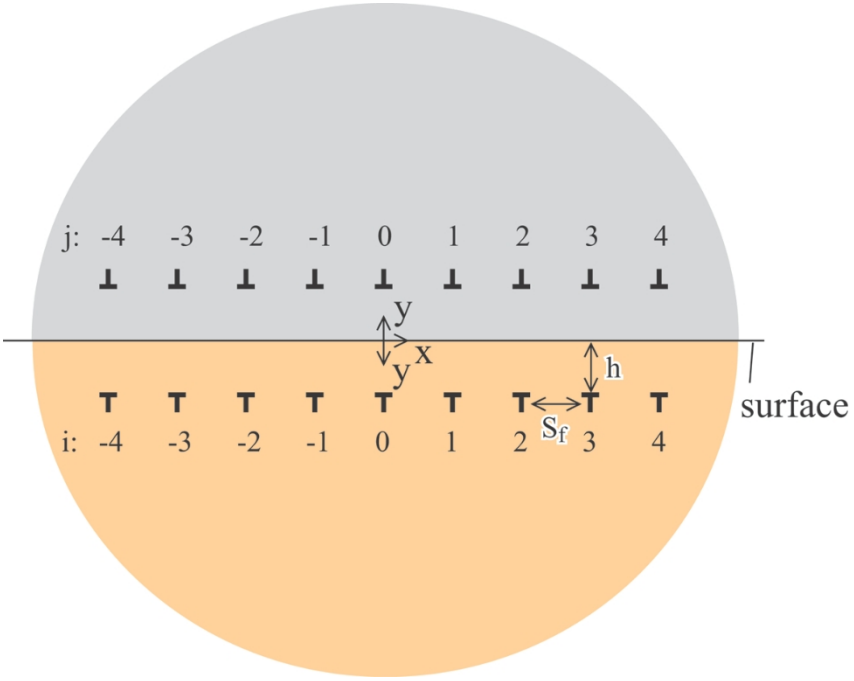

Figure 5-2. Geometry of a dislocation array under a surface.

Now we use Eq. (2) to derive our misfit dislocation model. The geometry of our problem is illustrated in Fig. 5-2, where a misfit dislocation array is formed under a surface. In Fig. 5-2, the horizontal line indicates the surface, and the orange region below the line represents the film. As in common misfit dislocation theory, we assume that the system is elastically homogeneous. Unlike the common misfit dislocation theory where the elastic properties of the homogeneous system are associated with those of the film, here we do not associate the elastic properties of our

system to either the film or the substrate, but rather view these properties as the apparent properties of the entire system. An array of edge type of misfit dislocations (i = …, -4, -3, -2, -1, 0, 1, 2, 3, 4, …) with separation distance S_f are assumed to form at a distance h below the surface. Note that according to the discussion above, S_f is the dislocation spacing in an unstrained film. In order to mimic a free surface, we can imagine that the system is mirror reflected above the surface, where the reflected portion is an image material shown in gray and the reflected dislocations (j = …, -4, -3, -2, -1, 0, 1, 2, 3, 4, …) are image dislocations. Note that for the geometry shown in Fig. 5-1, there is a non-zero normal stress σ_{yy} at the surface. As a result, the effect of the image edge dislocations is not exactly equivalent to that of a free surface. This is different from screw dislocations where the introduction of image dislocations represents exactly a free surface because the traction at the surface is zero. A more precise treatment of a free surface has been provided by Willis *et al* [46]. Our main objective here is to compare MD and continuum models so that the treatment remains precise, provided we use an MD configuration equivalent to the mirror imaged surface (such as the dislocation dipole configurations as will be shown below).

Referring to Fig. 5-2, the energy change due to the formation of the dislocation array below the surface is half of the work done to separate the two dislocation arrays from 2y = 0 to 2y = 2h. Note that the zero initial dislocation separation distance 2y = 0 represents a dislocation-free system because positive and negative dislocations lie exactly on top of each other and therefore they annihilate. Hence, the initial dislocation energy $E_{initial} = 0$. The y component of the attractive force between two opposite dislocations i and j offset in the x and y directions by $(i-j)S_f$ and 2y is expressed as [61]

$$f_{ij} = \frac{Gb^2}{2\pi(1-\nu)} \frac{(2y)\left\{\left[(i-j)S_f\right]^2 + (2y)^2\right\}}{\left\{\left[(i-j)S_f\right]^2 + (2y)^2\right\}^2} \tag{3}$$

According to Eq. (2), the work to overcome this force for separating dislocations i and j from 2y = 0 to 2y = 2h (x separation fixed) is

$$w_{ij} = \int_0^{2h} f_{ij} \cdot d(2y) = \begin{cases} 2E_c + \dfrac{Gb^2}{2\pi(1-\nu)} \ln\left(\dfrac{h}{r_0}\right), & i = j \\ \dfrac{Gb^2}{2\pi(1-\nu)} \left\{ \dfrac{1}{2} \ln\left(\dfrac{\left[(i-j)S_f\right]^2 + (2h)^2}{\left[(i-j)S_f\right]^2} \right) + \dfrac{(2h)^2}{\left[(i-j)S_f\right]^2 + (2h)^2} \right\}, & i \neq j \end{cases} \tag{4}$$

Note that when i = j, the x- coordinates of dislocations i and j are the same so that the integration cannot be performed from 2y = 0 because the dislocation separation distance is zero leading to the overlap of dislocation cores. Instead, integration is performed from $2y = 2r_0$ to 2y = 2h, and the contribution from 2y = 0 to $2y = 2r_0$ is treated as dislocation core energies $2E_c = \int_0^{2r_0} f_{ii} \cdot (2y)$.

The total work done to separate the two dislocations arrays from 2y = 0 to 2y = 2h is $\sum_{i=-\infty}^{\infty}\sum_{j=-\infty}^{\infty} w_{ij}$. The work done between a given dislocation in the i array (say i = 0) and all dislocations in the j array is then w = $\sum_{j=-\infty}^{\infty} w_{0j}$. Only half of the work converts to the energy of the dislocation i = 0 (other half goes to the image dislocation in the j array), and hence, $\Gamma = \frac{1}{2}\sum_{j=-\infty}^{\infty} w_{0j} = \frac{1}{2} w_{00} + \sum_{j=1}^{\infty} w_{0j}$ (here we use the symmetry of j < 0 and j > 0). We then have

$$\Gamma = E_c + \frac{Gb^2}{4\pi(1-\nu)}\ln\left(\frac{h}{r_0}\right) + \frac{Gb^2}{2\pi(1-\nu)}\sum_{j=1}^{\infty}\left\{\frac{1}{2}\ln\left[\frac{(jS_f)^2+(2h)^2}{(jS_f)^2}\right] + \frac{(2h)^2}{(jS_f)^2+(2h)^2}\right\} =$$

$$E_c + \frac{Gb^2}{4\pi(1-\nu)}\left\{\ln\left(\frac{h}{r_0}\right) + 2\pi\frac{h}{S_f}\coth\left(2\pi\frac{h}{S_f}\right) + \ln\left[\sinh\left(2\pi\frac{h}{S_f}\right)\right] - \ln\left(2\pi\frac{h}{S_f}\right) - 1\right\} = \quad (5)$$

$$E_c + \frac{Gb^2}{4\pi(1-\nu)}\left\{\ln\left(\frac{h}{r_0}\right) + f\left(\frac{h}{S_f}\right)\right\}$$

where coth, sinh (and cosh to be referred below) are hyperbolic functions, and f(x) is defined as

$$f(x) = 2\pi\cdot x\cdot\coth(2\pi\cdot x) + \ln[\sinh(2\pi\cdot x)] - \ln(2\pi\cdot x) - 1 \quad (6)$$

Note that f(x) approaches exactly 0 when $x \to 0$, and f(x)/(4πx) approaches exactly 1 when $x \to \infty$. A more direct comparison of f(x) and 4πx is shown in Fig. 5-3, It can be seen from Fig. 5-3(a) that f(x) can be pretty well approximated by 4πx as the relative difference between f(x) and 4πx is small. However, this approximation is associated with an absolute difference between f(x) and 4πx that does not reduce with increasing x as can be seen from the finer-scale plot shown in Fig. 5-3(b). As will be demonstrated below, approximation of f(x) with 4πx can introduce errors. Regardless, if f(x) is approximated by 4πx, we have

$$\Gamma = E_c + \frac{Gb^2}{4\pi(1-\nu)}\ln\left(\frac{h}{r_0}\right) + \frac{Gb^2}{(1-\nu)}\cdot\frac{h}{S_f} \quad (7)$$

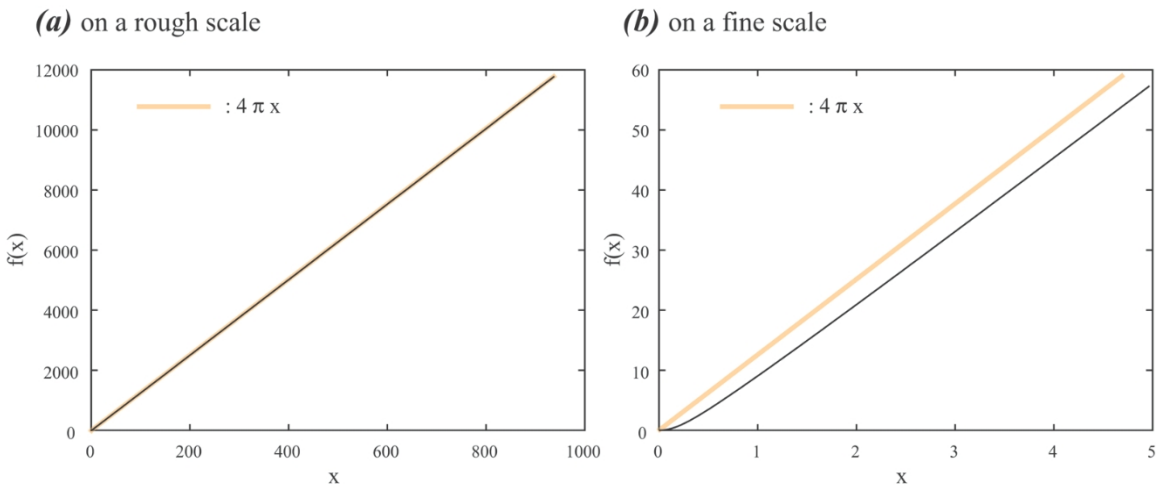

Figure 5-3. Comparison between f(x) and 4□x in (a) a rough and (b) a fine scale.

Assume that the material is subject to a strain of ε prior to the formation of misfit dislocations to mimic the mismatch. Due to the uniform strain ε, the initial dislocation-free system has a strain energy of $E_0 = \frac{1}{2}\frac{2G_f}{(1-\nu_f)}\varepsilon^2 \cdot S_f \cdot h$ in the material volume containing one dislocation (the z- dimension is assumed to be unity). It is important to note that here we use the film elastic properties G_f and ν_f to replace the apparent elastic properties of the film + substrate. This is because the strain energy is clearly caused by the strain in the film whereas dislocation energy comes from the strain fields in both film and substrate. The uniform strain also exerts a force of $\frac{2G_f}{(1-\nu_f)}\varepsilon \cdot b$ on the dislocation in the y direction, which does a work of $w_\varepsilon = \frac{2G_f}{(1-\nu_f)}\varepsilon \cdot b \cdot h$ when the dislocation moves from the surface to a distance of h below the surface. The work consumes the system energy, resulting in the reduction of system energy of $\Delta E_\varepsilon = -\frac{2G_f}{(1-\nu_f)}\varepsilon \cdot b \cdot h$. The total system energy per unit of surface area can be defined as $E_s = \frac{\Gamma + E_0 + \Delta E_\varepsilon}{S}$, where S is dislocation spacing, which equals surface area per dislocation as our z- dimension is unity. It is extremely important to realize that the S_f assumed in our derivation is the unstrained length of the film, but here S stands for the dislocation spacing in the deformed state (the same as the rigid substrate) so that the energy is normalized by the common definition of the surface area. Because S and S_f satisfy $S/S_f = 1 + \varepsilon$, significant error may occur if S is incorrectly used for S_f when ε is large.

Based on Γ defined by Eq. (7), and E_0, ΔE_ε as discussed above, the energy per unit of surface area can be written as

$$E_s = \frac{E_c}{S} + \frac{G_f b^2}{4\pi(1-\nu_f)}\frac{\gamma}{S}\ln\left(\frac{h}{r_0}\right) + \frac{G_f h}{(1-\nu_f)}\left[\frac{\gamma b^2}{S_f S} + \varepsilon^2\frac{S_f}{S} - \frac{2\varepsilon b}{S}\right] \tag{8}$$

where $\gamma = \frac{G}{G_f}\cdot\frac{(1-\nu_f)}{(1-\nu)}$ can be viewed as a correction for the elastic inhomogeneity of the system. It can be seen from Eq. (8) that if we ignore the dislocation core energy, and set $b = b_f$, $\gamma = 1$ and $S_f = S$, Eq. (8) reduces exactly to Eq. (1) where the parameter b_f/β can be considered as equivalent to r_0. For practical applications, the film length S_f is replaced by $S/(1+\varepsilon)$ leading to

$$E_s = \frac{E_c}{S} + \frac{G_f b^2}{4\pi(1-\nu_f)}\frac{\gamma}{S}\ln\left(\frac{h}{r_0}\right) + \frac{G_f h}{(1-\nu_f)}\cdot\left[\gamma\frac{b^2}{S^2}(1+\varepsilon) + \frac{\varepsilon^2}{1+\varepsilon} - \frac{2\varepsilon b}{S}\right] \tag{9}$$

Eqs. (8) and (9) are based on the approximate dislocation energy expression Eq. (7). If we use a more accurate dislocation energy expression Eq. (5), Eq. (9) becomes

$$E_s = \frac{E_c}{S} + \frac{G_f b^2}{4\pi(1-\nu_f)}\frac{\gamma}{S}\ln\left(\frac{h}{r_0}\right) + \frac{G_f h}{(1-\nu_f)}\left\{\gamma\frac{b^2}{S^2}(1+\varepsilon)\frac{f\left(\frac{1+\varepsilon}{S}h\right)}{4\pi\left(\frac{1+\varepsilon}{S}h\right)} + \frac{\varepsilon^2}{1+\varepsilon} - \frac{2\varepsilon b}{S}\right\} \tag{10}$$

where f(x) is defined by Eq. (6). This result is similar to those of Willis et al [46,59,60], although subtle difference must exist as our expression is precise for a mirror boundary whereas theirs are for a free surface.

Our derivation gives some useful insights. In particular, we find from Eq. (7) that the dislocation energy (ignoring the core part) is $\frac{Gb^2}{4\pi(1-\nu)}\ln\left(\frac{h}{r_0}\right) + \frac{Gb^2}{(1-\nu)}\cdot\frac{h}{S_f}$. Clearly $\frac{Gb^2}{4\pi(1-\nu)}\ln\left(\frac{h}{r_0}\right)$ is dislocation self-energy because it is equivalent to Eq. (7) in the isolated dislocation condition $S_f \to \infty$. The additional term $\frac{Gb^2}{(1-\nu)}\cdot\frac{h}{S_f}$ then represents the interactive energy of dislocations. It can be seen that for a homogeneous material system (i.e., the system contains dislocations but the mismatch strain $\varepsilon = 0$), Eq. (9) correctly reduces to dislocation energy per unit of surface area, i.e., Eq. (7) divided by S. Furthermore, Eq. (9) indicates that the energy of the homogeneous system is a summation of dislocation core energy, dislocation self-energy, and a strain energy of $\frac{1}{2}\cdot E\cdot\varepsilon_d^2\cdot V$, where $E = \frac{2G}{1-\nu}$ is the apparent Young's modulus, $\varepsilon_d = \frac{b}{S_f}$ is the strain caused by the dislocations, and $V = h\cdot S_f$ is the volume per dislocation.

This is consistent with the notion that the overlap of the elastic field of an array of edge dislocations essentially leads to a uniform strain ε_d in the far field.

XVIII. CONTINUUM ENERGY OF DISLOCATION DIPOLES UNDER PERIODIC BOUNDARY CONDITIONS

As described above, accurate molecular dynamics simulations of dislocations must be performed using dipole configurations under the periodic boundary conditions. To establish a link between MD simulations and continuum calculations, we now derive a continuum energy expression for dislocation dipoles in a cell with periodic boundary conditions. In this case, the dislocation dipoles are essentially an infinite array, as shown in Fig. 5-4(a), where L_x and L_y represent, respectively, the periodic length in the x- and y- directions, and d is the dipole separation distance. Furthermore we can assume that the dipole separation, d, satisfies $0 \leq d \leq L_y$ because the energy periodically repeats outside this range.

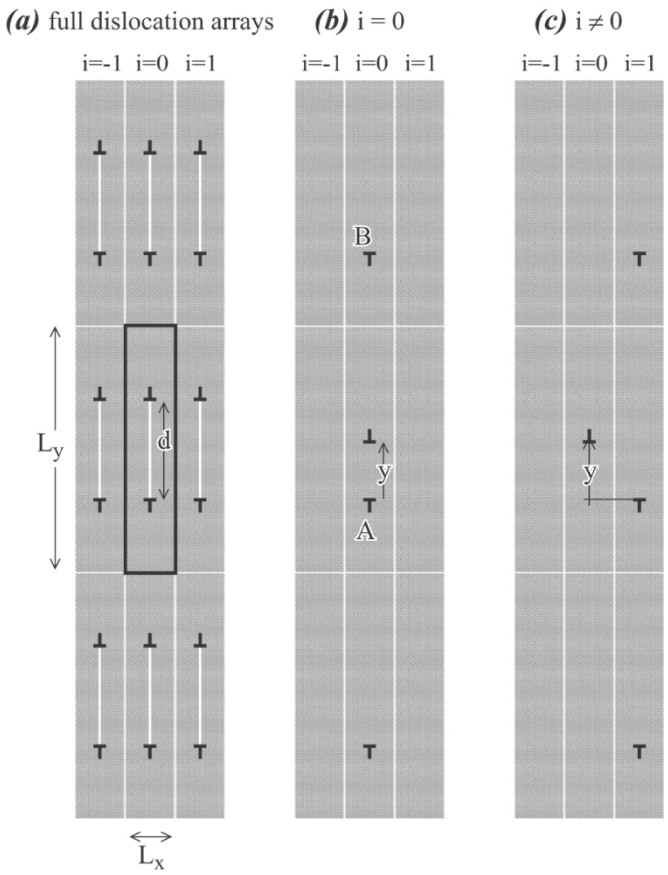

Figure 5-4. (a) Dislocation dipoles under periodic boundary conditions; (b) interaction of a positive dislocation with all the negative dislocations in the same column i = 0; and (c) interaction of the positive dislocation with all the negative dislocations in a different column i □ 0. The unit cell is framed in black.

To derive an energy expression for a dislocation array, we can imagine that initially the positive dislocations (⊥) lie exactly on top of the negative dislocations (**T**). Hence, the dislocations annihilate so that the initial energy $E_{initial}$ is zero. The dislocation energy can then be calculated from the work done to move the positive dislocations away from the negative dislocations. Because dislocations are identical, we only need to consider the work to move one positive dislocation away from the negative dislocation array along the y direction. Since the work is linearly additive, we consider separately the interaction between the positive dislocation and all the negative dislocations in the same column (i = 0) as shown in Fig. 5-4(b), and the interaction between the positive dislocation and all the negative dislocations in a different column (i ≠ 0) as shown in Fig. 5-4(c).

According to Eq. (4) and Fig. 5-4(b), the work to separate two opposite dislocations from an original separation distance Δy_1 to a final separation dislocation Δy_2 can be calculated as

$$w_{pair} = \frac{Gb^2}{2\pi(1-\nu)} \ln\left(\frac{\Delta y_2}{\Delta y_1}\right) \tag{11}$$

Assume that the positive dislocation moves from an initial location at y = 0 to a final location at y = d. For the negative dislocation "A" shown in Fig. 5-4(b), the original separation distance (with the positive dislocation) is $\Delta y_1 = 0$, and the final separation dislocation is $\Delta y_2 = d$. For the negative dislocation B, the original separation distance is $\Delta y_1 = L_y$, and the final separation distance is $\Delta y_2 = L_y - d$. For other negative dislocations below A, the original separation distance is $\Delta y_1 = j \cdot L_y$, and the final separation is $\Delta y_2 = j \cdot L_y + d$ (j = 1, 2, …, ∞). For other negative dislocations above B, the original separation distance is $\Delta y_1 = (j+1) \cdot L_y$, and the final separation is $\Delta y_2 = (j+1) \cdot L_y - d$ (j = 1, 2, …, ∞). Note that for all dislocations below A or above B, the work can be calculated normally because the dislocation separation distances will never approach zero for $0 \neq d \neq L_y$. For dislocations A and B, the work must exclude the overlapped region of dislocation cores (total size of $2r_0$) whereas the excluded energy is replaced by dislocation core energies (total energy of $2E_c$ for two cores) as described above. Hence, the total work to move the positive dislocation against all negative dislocations in the same column (i = 0) from an initial position at y = 0 to a final position at y = d can be expressed as

$$w_0 = 2E_c + \frac{Gb^2}{2\pi(1-\nu)}\left\{\ln\left(\frac{d}{2r_0}\right) + \ln\left(\frac{L_y - d}{L_y - 2r_0}\right) + \sum_{j=1}^{\infty}\left[\ln\left(\frac{j \cdot L_y + d}{j \cdot L_y}\right) + \ln\left(\frac{(j+1) \cdot L_y - d}{(j+1) \cdot L_y}\right)\right]\right\} \tag{12}$$

Because the work increases the energies of both positive and negative dislocations, energy per dislocation is half of the work. We then have an energy contribution due to a positive dislocation interacting with all negative dislocations in the same column:

$$E_0 = E_c + \frac{Gb^2}{4\pi(1-\nu)}\left\{\ln\left(\frac{d}{2r_0}\right) + \ln\left(\frac{L_y - d}{L_y - 2r_0}\right) + \sum_{i=1}^{\infty}\left[\ln\left(\frac{i \cdot L_y + d}{i \cdot L_y}\right) + \ln\left(\frac{(i+1) \cdot L_y - d}{(i+1) \cdot L_y}\right)\right]\right\} \tag{13}$$

The summation of Eq. (13) has a closed form of

$$E_0 = E_c + \frac{Gb^2}{4\pi(1-\nu)}\left\{\ln\left(\frac{d}{2r_0}\right) + \ln\left(\frac{L_y - d}{L_y - 2r_0}\right) - \ln\left[Ga\left(\frac{L_y + d}{L_y}\right)\right] - \ln\left[Ga\left(2 - \frac{d}{L_y}\right)\right]\right\} \tag{14}$$

where Ga is the Euler gamma function.

According to Eq. (3) and Fig. 5-4(c), the work to separate two opposite dislocations that are not in the same column from an initial y- component of separation distance Δy_1 to a final y-component of separation distance Δy_2 can be calculated as

$$w_{pair} = \frac{Gb^2}{2\pi(1-\nu)}\left\{\frac{1}{2}\ln\left[\frac{(i \cdot L_x)^2 + \Delta y_2^2}{(i \cdot L_x)^2 + \Delta y_1^2}\right] - \frac{(i \cdot L_x)^2}{(i \cdot L_x)^2 + \Delta y_2^2} + \frac{(i \cdot L_x)^2}{(i \cdot L_x)^2 + \Delta y_1^2}\right\} \tag{15}$$

Following the same approach used above, the total work to move the positive dislocation from y = 0 to y = d can be expressed as

$$w_i = \frac{Gb^2}{2\pi(1-\nu)}\sum_{j=0}^{\infty}\left\{\begin{array}{l}\frac{1}{2}\ln\left[\frac{(i\cdot L_x)^2+(j\cdot L_y+d)^2}{(i\cdot L_x)^2+(j\cdot L_y)^2}\right]+\frac{1}{2}\ln\left[\frac{(i\cdot L_x)^2+[(j+1)\cdot L_y-d]^2}{(i\cdot L_x)^2+[(j+1)\cdot L_y]^2}\right]- \\ \frac{(i\cdot L_x)^2}{(i\cdot L_x)^2+(j\cdot L_y+d)^2}+\frac{(i\cdot L_x)^2}{(i\cdot L_x)^2+(j\cdot L_y)^2}-\frac{(i\cdot L_x)^2}{(i\cdot L_x)^2+[(j+1)\cdot L_y-d]^2}+ \\ \frac{(i\cdot L_x)^2}{(i\cdot L_x)^2+[(j+1)\cdot L_y]^2}\end{array}\right\} \tag{16}$$

The energy contribution per dislocation is half of the work so we have

$$E_i = \frac{Gb^2}{4\pi(1-\nu)}\sum_{j=0}^{\infty}\left\{\begin{array}{l}\frac{1}{2}\ln\left[\frac{(i\cdot L_x)^2+(j\cdot L_y+d)^2}{(i\cdot L_x)^2+(j\cdot L_y)^2}\right]+\frac{1}{2}\ln\left[\frac{(i\cdot L_x)^2+[(j+1)\cdot L_y-d]^2}{(i\cdot L_x)^2+[(j+1)\cdot L_y]^2}\right]- \\ \frac{(i\cdot L_x)^2}{(i\cdot L_x)^2+(j\cdot L_y+d)^2}+\frac{(i\cdot L_x)^2}{(i\cdot L_x)^2+(j\cdot L_y)^2}-\frac{(i\cdot L_x)^2}{(i\cdot L_x)^2+[(j+1)\cdot L_y-d]^2}+ \\ \frac{(i\cdot L_x)^2}{(i\cdot L_x)^2+[(j+1)\cdot L_y]^2}\end{array}\right\} \tag{17}$$

Eq. (17) has a closed form

$$E_i = \frac{Gb^2}{4\pi(1-\nu)}\left\{\begin{array}{l}\frac{2\pi\cdot i\cdot L_x\cdot Coth\left(\frac{\pi\cdot i\cdot L_x}{L_y}\right)\cdot Sin^2\left(\frac{\pi\cdot d}{L_y}\right)}{L_y\cdot Cosh\left(\frac{2\pi\cdot i\cdot L_x}{L_y}\right)-L_y\cdot Cos\left(\frac{2\pi\cdot d}{L_y}\right)}+ \\ \frac{1}{2}\ln\left[Cos^2\left(\frac{\pi\cdot d}{L_y}\right)+Coth^2\left(\frac{\pi\cdot i\cdot L_x}{L_y}\right)\cdot Sin^2\left(\frac{\pi\cdot d}{L_y}\right)\right]\end{array}\right\} \tag{18}$$

The dislocation energy under the periodic boundary condition is then

$$\Gamma = E_0 + \sum_{i=-\infty}^{-1} E_i + \sum_{i=1}^{\infty} E_i = E_0 + 2\sum_{i=1}^{\infty} E_i \tag{19}$$

We could not find a closed form for Eq. (19). However, E_i is a positive, rapid decreasing monotonic function of i. As a result, Eq. (19) converges well to an accurate value when a sufficiently large number of terms are included.

XIX. MD GEOMETRY OF STRAIN RELAXATION, AND CALCULATIONS OF LATTICE AND ELASTIC CONSTANTS OF OUR MODEL SYSTEM

XIX.1 Geometry of the Strain Relaxation Problem

We first describe the geometry of our strain relaxation problem because it determines the relevant lattice and elastic constants impacting the strain relaxation. As a generic example, here we use the Cd-Te-S Stillinger-Weber potential [60] in our MD simulations to explore the growth of CdTe on a thick (i.e., non-compliant) CdS substrate. Note that, the particular materials are not important, not only because we are studying a 2D problem, but also because our objective is to compare MD and continuum models. Thus, any lattice mismatched systems will be sufficient. The geometry of the periodic system is shown in Fig. 5-5(a), where x-, y-, and z- are aligned

[60] X. W. Zhou, D. K. Ward, J. E. Martin, F. B. van Swol, J. L. Cruz-Campa, and D. Zubia, Phys. Rev. B, 88, 085309 (2013).

with [101], [010], and [$\bar{1}$01] respectively, and the (010) CdTe/CdS interface is parallel to the x-z plane. For the 2D case, we assume that the z- dimension of the system is fixed at the equilibrium lattice size of CdS, and hence, strain relaxation only occurs in the x- direction. To create misfit dislocation dipoles, some atomic planes (with a total thickness of a Burgers magnitude b), as indicated by the white line in Fig. 5-5(b), are removed. It can be seen that under the periodic boundary conditions, the geometry in Fig. 5-5(b) is exactly the same as that shown in 4(a).

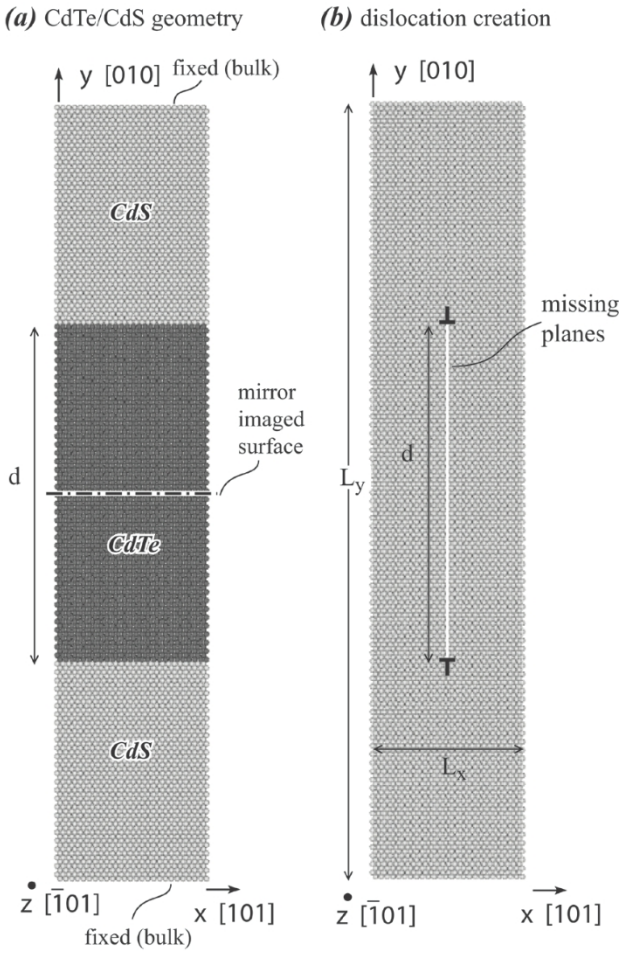

Figure 5-5. (a) MD Geometry of the CdTe on CdS structures where CdS is fixed in the x- and z- directions to the equilibrium bulk sizes to mimic a very large CdS thickness. The dotted-dashed line mimics the "mirror" surface shown in Fig. 5-2; and (b) creation of misfit dislocation dipoles (dislocation and its image) by removing planes within a thickness of Burgers vector magnitude b. Note that geometry shown in (b) is used for both inhomogeneous (CdTe/CdS) and homogeneous (pure CdTe and pure CdS) systems. The homogeneous systems are for dislocation energy calculations, where only the z- direction is fixed to the equilibrium bulk size of CdS and both x- and y- directions are relaxed.

XIX.2 MD Calculations of Lattice Constants

Molecular statics calculations of CdTe and CdS bulk crystals (i.e., apply the periodic boundary conditions) indicated that the CdS and CdTe lattice constants at 0 K are 5.835 Å and

6.478 Å respectively. Performing MD simulations at 300 K for 4 ns to equilibrate the systems, and another 8 ns to calculate average quantities, we found that the CdS and CdTe equilibrium lattice constants at 300 K are 5.847 ± 0.000 Å and 6.491 ± 0.000 Å, respectively. Here the average lattice constants obtained at various times are used to estimate the statistic deviation of the result. It can be seen that the MD results averaged over the 8 ns span gives highly converged results (essentially 0 standard error up to at least the third decimal point).

The lattice constants determined above are for the 3D systems. For our 2D case where the orientation is shown in Fig. 5-5 and the z- dimension is fixed at the 3D CdS size (i.e., $d_{(\bar{1}01)}$= $5.847/\sqrt{2}$), the systems may deviate from the cubic symmetry especially for CdTe where the z-dimension is now highly compressed. As a result, the x- and y- dimensions may correspond to different lattice constants. A second set of MD simulations are performed to calculate the equilibrium CdTe and CdS lattice constants in the x- direction under the 2D condition, again using an equilibration time of 4 ns and an averaging time of 8 ns. The lattice constant in the y-direction is not explored because it is irrelevant to the lattice mismatch. We find that when the z-dimension is constrained at the $d_{(\bar{1}01)}= 5.847/\sqrt{2}$, the 300 K CdS and CdTe lattice constants in the x- direction (from $a = \sqrt{2}\, d_{(101)}$) change to 5.769 ± 0.000 Å and 6.557 ± 0.000 Å, respectively. This means that under the 2D condition, our CdTe/CdS system corresponds to a lattice mismatch of $\varepsilon = (5.769 - 6.557) / 6.557 \approx -12.0177$ %.

XIX.3 C. MD Calculations of Young's Modulus

With the orientation given in Fig. 5-5 and the z-dimension fixed at the 3D CdS size, the 2D CdS and CdTe bulk crystals (i.e., apply the periodic boundary conditions) are uniaxially deformed in the x- direction to various strains $-0.13 < \varepsilon_{xx} < 0.18$, where positive strains means tension and negative strains indicates compression. Using an equilibration time of 4 ns and an averaging time of 8 ns, similar 2D MD simulations as described above are performed to calculate strain energy density E_ε of both CdS and CdTe as a function of ε_{xx} (here the x- dimension is also fixed leaving only the strain in the y- direction relaxed). The results are shown in Fig. 5-6, where red and blue colors distinguish CdS and CdTe. The dashed lines are fitted to linear elastic theory $E_\varepsilon = ½\, E \cdot \varepsilon_{xx}^2$ for a small strain range near equilibrium ($\varepsilon_{xx} = 0$). The solid lines are also fitted to $E_\varepsilon = ½\, E \cdot \varepsilon_{xx}^2$ except that the positive and negative strain ranges are fitted with separate Young's modulus E. Fig. 5-6 shows that the strain energy obtained from MD simulations approximately satisfies the linear elasticity relation $E_\varepsilon = ½\, E \cdot \varepsilon_{xx}^2$ only within a very small strain range. However, if different Young's moduli are used for tensile and compressive loads, then the $E_\varepsilon = ½\, E \cdot \varepsilon_{xx}^2$ relation can accurately describe the elastic behavior of the material over a large strain range. Because the linear elastic theory is based on a single elastic constant for both tension and compression, error may arise. For the 2D case studied here, we find that the CdS Young's modulus is E = 0.4323 eV/ Å^3 for positive strains and E = 0.9399 eV/ Å^3 for negative strains, and

the CdTe Young's modulus is E = 0.2738 eV/ Å^3 for positive strains and E = 0.4358 eV/Å^3 for negative strains. If a single elastic constant is assumed, then we found E = 0.8724 eV/Å^3 for CdS and E = 0.3071 eV/Å^3 for CdTe.

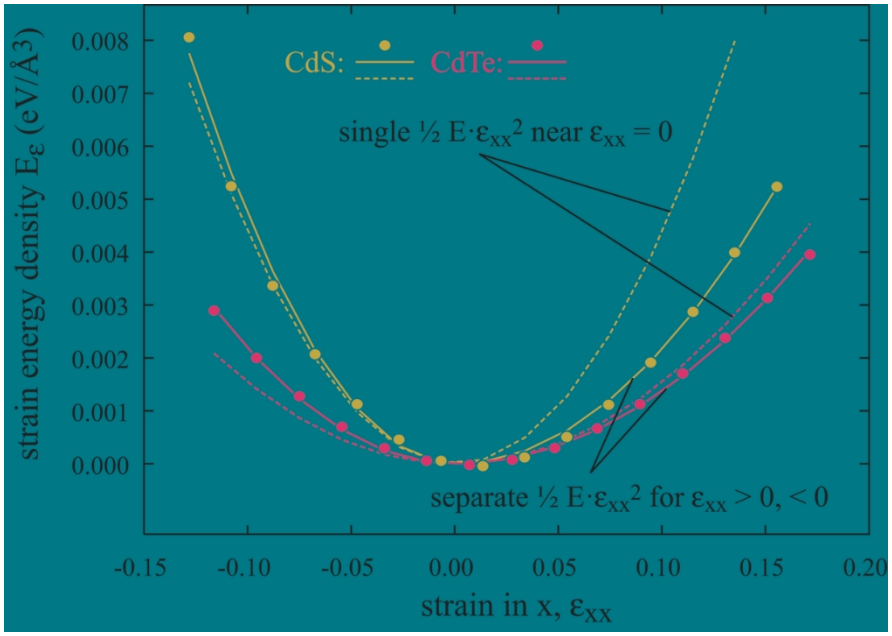

Figure 5-6. Strain energy density of CdS and CdTe.

XX. MD CALCULATIONS OF CDTE AND CDS DISLOCATION DIPOLE ENERGIES UNDER PERIODIC BOUNDARY CONDITIONS

XX.1 A. Effect of System Size

Based on the orientation shown in Fig. 5-5, it is convenient to use the number of atomic planes n_x, n_y, and n_z to represent the dimensions in the three coordinate directions $n_x = L_x / d_{\{101\}}$, $n_y = L_y / d_{\{100\}}$, and $n_z = L_z / d_{\{101\}}$, where $d_{\{101\}}$ and $d_{\{100\}}$ are the spacing between the corresponding atomic planes {hkl}. For the 2D case, only a small dimension in the z- direction is needed, and hence we use a constant $n_z = 6$ ($L_z \sim 25$ Å) throughout our study. With that given, we first explore the effect of system size on dislocation dipole energy using CdS as an example. Dislocation dipoles are created by removing the corresponding planes as shown in Fig. 5-5(b). Two dislocation dipole distances $d = 40\ d_{\{100\}}$ (~ 230 Å) and $d = 60\ d_{\{100\}}$ (~ 350 Å) are studied. For each dislocation dipole distance, 10 system dimensions corresponding to $n_x \times n_y$ = 24×86, 26×92, 28×98, 30×104, 32×110, 34×116, 36×122, 38×128, 40×134, and 42×140 are used. Here the smallest system $n_x \times n_y$ = 24×86 corresponds to $L_x \times L_y \sim 100 \times 500$ Å^2, whereas the largest system $n_x \times n_y$ = 42×140 corresponds to $L_x \times L_y \sim 170 \times 820$ Å^2. With the chosen system dimensions, L_y and L_x roughly satisfy the relation $L_y = 81.7 + 4.24\ L_x$.

MD simulations are performed at 300 K for 4 ns to equilibrate the systems, and another 16 ns to calculate average energies of both perfect crystals and crystals containing the dislocation dipoles. If the energies for the perfect and the dislocated crystals are denoted as E_p and E_d, respectively, then the dislocation line energy is calculated as

$$\Gamma = \frac{E_d - \frac{N_d}{N_p} \cdot E_p}{2 \cdot L_z} \tag{20}$$

where N_d and N_p are respectively total number of atoms in the dislocated and perfect systems (the ratio N_d/N_p scales the perfect energy towards the same number of atoms in the dislocated system), and $2 \cdot L_z$ is the total length of the dislocation dipole. The results of the MD simulations are shown in Fig. 5-7 as the circular data points, where the lines are calculated using Eq. (19). Note that Eq. (19) involves some parameters such as dislocation core radius r_0, core energies E_c, and the Young's modulus $E = \frac{2G}{1-\nu}$. As discovered above, even pure CdS exhibits different elastic constants in tensile and compressive regions around the edge dislocation. Hence, the Young's modulus E is an apparent property not yet known. All three parameters, r_0, E_c, and E, are not fitted to the MD data in Fig. 5-7, but are rather fitted to independent MD data to be described below. Hence, the excellent agreement between the MD data and the line is a strong validation of the consistence between the continuum theory and the MD simulations.

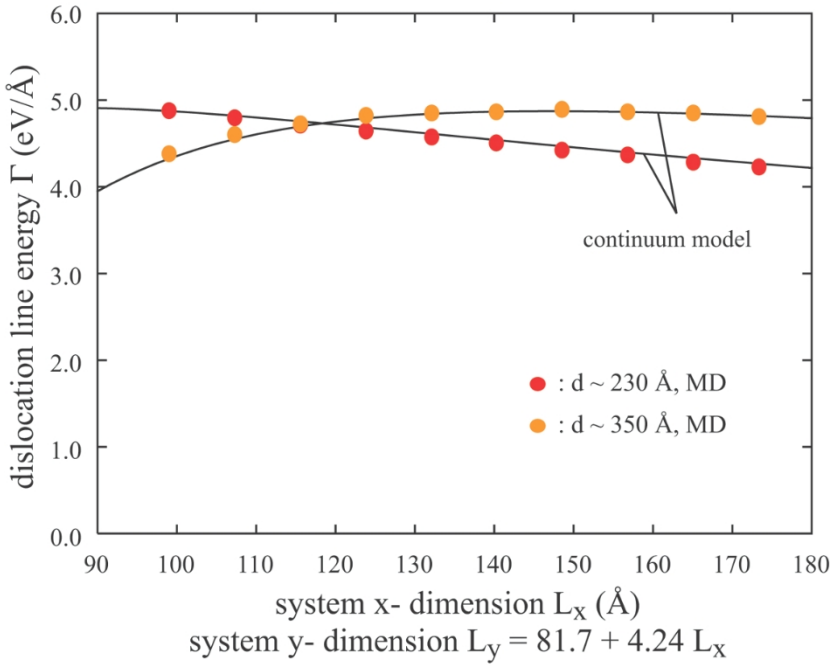

Figure 5-7. CdS dislocation line energy as a function of system dimension.

For the d ~ 230 Å case, both the data points and line in Fig. 5-7 indicate a monotonically decreasing dislocation line energy with system dimension. Considering that the MD data is highly converged and the line represents a continuum model, this monotonic trend is real. Additional simulations with an order of magnitude increase in the dimensions confirmed that dislocation line energies are significantly lower than the ones shown in Fig. 5-7. Intuitively, dislocation energy reaches maximum when opposite dislocations are most widely separated so that their elastic fields least overlap (cancel). Under the periodic boundary condition, the widest dislocation separation occurs when dislocation dipole distance d reaches $L_y/2$. When the spacing d between a dislocation and one of its neighbor reaches $d > L_y/2$, the spacing between this dislocation and its other neighbor becomes $d' = L_y - d < L_y/2$. Based on this recognition, when d = 230 Å, the maximum dislocation energy occurs at L_y = 460 Å, which gives L_x = 89 Å according to our constraint of the L_y vs. L_x relation. This L_x is lower than the dimension range explored in Fig. 5-7, and hence the dislocation energy for the d = 230 Å case is seen to monotonically decrease in Fig. 5-7. When d = 350 Å, the maximum dislocation energy occurs at L_y = 700 Å, which gives L_x = 146 Å. Indeed, the maximum dislocation energy for the d = 350 Å case seems to occur between L_x = 140 Å and L_x = 150 Å.

For comparison, molecular statics simulations are also performed to calculate the dislocation energies for the case with dipole distance d = 40 $d_{\{100\}}$ (~ 230 Å). We found that the MS data is very scattered. Especially at large system dimensions, the scatter is so large that the MS data is essentially useless for validating continuum models. We emphasize that we have tried various approaches to help more thoroughly minimize the energy in our MS simulations,

including many alternating MD and MS steps at various MD temperatures. Hence, it is clear that MS simulations cannot lead to unique results for large systems (e.g., the largest system explored here involves 140,160 atoms) containing defects. On the other hand, the long time (16 ns) averaged MD results are extremely smooth. Without such high quality MD data the present work would not have been possible.

XX.2 B. Effect of Dislocation Dipole Distance

Now we focus on exploring dislocation energy as a function of dipole distance at fixed system dimensions of $n_x \times n_y = 32 \times 110$. The same MD methods as described above are used to calculate the dislocation energies of the CdS and CdTe 2D crystals at 10 different dislocation dipole spacing of d = 10 $d_{\{100\}}$, 20 $d_{\{100\}}$, 30 $d_{\{100\}}$, 40 $d_{\{100\}}$, 50 $d_{\{100\}}$, 60 $d_{\{100\}}$, 70 $d_{\{100\}}$, 80 $d_{\{100\}}$, 90 $d_{\{100\}}$ and 100 $d_{\{100\}}$. The results are shown in Fig. 5-8 using the circular data points. The MD data is also used to fit the unknown parameters in the continuum expression, Eq. (19), namely, dislocation core radius r_0, core energies E_c, and the apparent Young's modulus $E = \frac{2G}{1-\nu}$. The fitted parameters are shown in Table 5-1. Note that Young's moduli of CdS and CdTe have also been determined from independent MD simulation of uniaxial deformation as described above. The Young's moduli from the uniaxial deformation simulations are included in Table 5-1. It can be seen that the Young's modulus derived from the dislocation energy simulations is between the compressive and tensile Young's moduli determined from the deformation simulations, confirming the consistence of the calculations. We point out that strictly speaking, there are no unique solutions for dislocation core radius and energy. This is because by concept, any radius can be taken as the core radius as long as the materials beyond this radius follow the linear elastic theory. Obviously a large radius always satisfies this condition. Practically, a small core radius is preferred to minimize the effect of ignoring the core in the classical elastic theory. Ideally, one would constrain the core radius to progressively smaller values and fit the other parameters. The smallest radius that yields a satisfactory fit can be taken as the ideal radius. Our core radii from un-constrained fits are acceptable as they are not too big, and both our core radii and core energies are consistent with the values typically assumed in literature [61]. Most importantly, we do not ignore the core contribution in our model so that even a big radius does not really introduce a big error.

The fitted continuum curves are included in Fig. 5-8 using lines. An excellent agreement between MD and continuum calculations is obtained. This means that even if the system is elastically inhomogeneous, the use of a single elastic constant between the two (tensile and compressive) elastic constants can still be extremely accurate. This also means that the rigorously derived continuum model incorporates the physics needed to describe the dislocation dipole energy under the periodic boundary conditions. Note that the lines in Fig. 5-7 are also calculated with the same set of parameters fitted for Fig. 5-8. While the agreement achieved in

[61] E. B. Webb III, J. A. Zimmerman, and S. C. Seel, Math. Mech. Solids, 13, 221 (2008).

Fig. 5-8 may be partly attributed to the parameter optimization, the agreement achieved in Fig.5-7 convincingly verifies the transferability of the model.

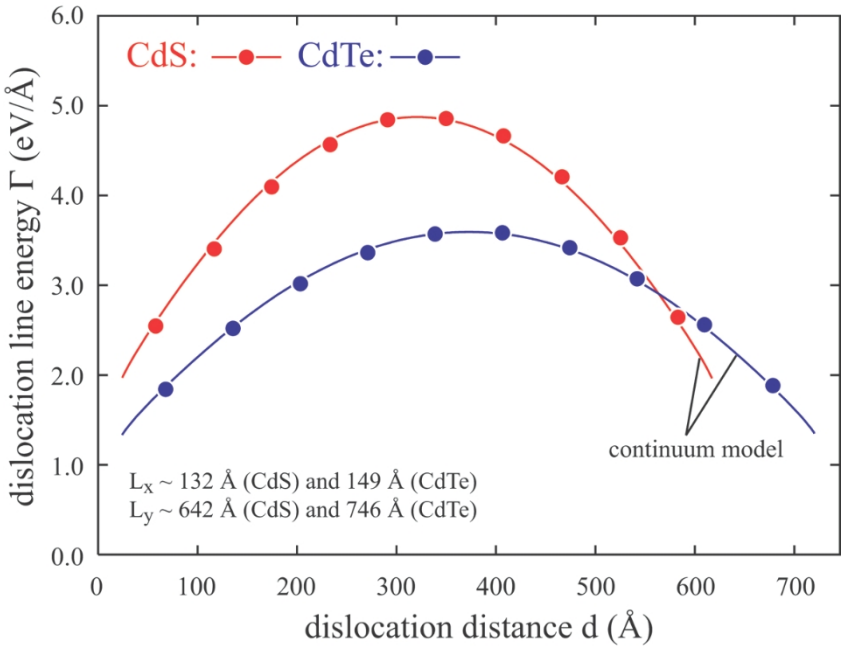

Figure 5-8. CdS and CdTe dislocation energies as a function of dislocation dipole distance for given system dimensions L_x and L_y.

Table 5-1. Dislocation core radius r_0 (Å), core energy E_c (eV/Å), and apparent Young's modulus E (eV/Å^3) as derived from MD dislocation energy and MD uniaxial deformation simulations.

material	dislocation energy simulations			Uniaxial deformation simulations		
	r_0	E_c	E = 2G/(1-ν)	E = 2G/(1-ν)		
				compression	tension	overall
CdS	9.3141	1.7748	0.6894	0.9399	0.4323	0.8724
CdTe	12.4596	1.2984	0.3921	0.4358	0.2738	0.3071

Fig. 5-8 indicates that dislocation energy as a function of dislocation dipole distance d reaches maximum and is symmetric at $d = L_y/2$. This can be easily understood because under the periodic boundary conditions, our dislocation dipole geometry can be described by Fig. 5-4(a). Increasing the dipole distance is equivalent to moving the positive dislocation array in the y direction while keeping the negative dislocations fixed. Each positive dislocation can be viewed as forming two dipoles, one with a negative dislocation below at a distance d, and the other one with a negative dislocation above with a distance L_y - d. Hence, the overall energy is symmetric with the symmetric point occurs at $d = L_y/2$.

XXI. EXAMINATION OF CONTNUUM MISFIT DISLOCATION THEORY USING MD SIMULATIONS

Figs. 5-8 show that MD simulations produce exactly the continuum strain energies and dislocation energies. If our derivation of the continuum energy expression Eq. (10) of the lattice mismatched system is correct, then there are no reasons that Eq. (10) would not match the MD simulations. MD simulations are therefore carried out to calculate energies of lattice mismatched systems. Using the geometry shown in Fig. 5-5(a), CdS crystals with 32 (101) planes in the x-direction, 110 (010) planes in the y- direction, and 6 $(\bar{1}01)$ planes in the z- direction, are created. As described above, the x- and z- dimension are fixed at the CdS sizes (i.e., $d_{(101)}= 5.769/\sqrt{2}$, and $d_{(\bar{1}01)} = 5.847/\sqrt{2}$). The middle region of the CdS crystal of various thicknesses, d = 2h = 10 $d_{(010)}$, 20 $d_{(010)}$, 30 $d_{(010)}$, 40 $d_{(010)}$, 50 $d_{(010)}$, and 60 $d_{(010)}$, are changed to CdTe. Misfit dislocation dipoles are then created by removing extra planes in the CdTe region as shown in Fig. 5-5(b). Zero, one, two, and four dislocation dipoles are all simulated. If no dislocation dipoles are created, then dislocation spacing S = infinity. If the system contains m dislocation dipoles, the dislocation spacing is L_x/m. Hence, creation of 1, 2, and 4 dislocation dipoles give S = 32 $d_{(010)}$ (130 Å), 16 $d_{(010)}$ (65 Å), and 8 $d_{(010)}$ (33 Å) respectively.

MD simulations are performed at 300 K for 8 ns to equilibrate the systems, and another 16 ns to calculate average energies. The energies obtained from MD simulations include cohesive energies of atoms, and extra energies from the CdTe/CdS interfaces. Both energies are not included in Eq. (10), and hence need to be removed. Assume that the number of Te and S atoms in the system are N_{Te} and N_S respectively, then the number of Cd atoms $N_{Cd} = N_{Te} + N_S$. If total energy of the system is E_{tot}, the cohesive energies (per atom) of CdTe and CdS bulk crystals are E_{CdTe} and E_{CdS} respectively, and the interfacial energy is ρ, then the MD version of Eq. (10) becomes

$$E_{s,MD} = \frac{E_{tot} - 2N_{Te}E_{CdTe} - 2N_S E_{CdS} - 2L_x L_z \rho}{2L_x L_z} \tag{21}$$

where the factor 2 in the numerator $2L_xL_z$ accounts for two interfaces, and the factor 2 in the denominator $2L_xL_z$ means that we only calculate half of the energy because the MD geometry shown in Fig. 5-5(a) includes both the CdTe/CdS system and its mirror image (above the dotted-dashed line), whereas Eq. (10) does not include the image contribution. In Eq. (21), only the interfacial energy, ρ, is unknown. Hence, ρ is first determined. For convenience of using MD data, Eq. (11) is first rewritten as

$$E_s = \frac{E_c}{S} + \frac{G_f b^2}{4\pi(1-\nu_f)S}\gamma \ln\left(\frac{h}{r_0}\right) + \frac{1}{2}E_f \frac{2N_{Te}\Omega_{CdTe}}{2L_x L_z}\left\{\gamma \frac{b^2}{S^2}(1+\varepsilon)^2 \frac{f\left(\frac{1+\varepsilon}{S}h\right)}{4\pi\left(\frac{1+\varepsilon}{S}h\right)} + \varepsilon^2 - \frac{2\varepsilon b(1+\varepsilon)}{S}\right\} \tag{22}$$

where E_f is the compressive Young's modulus of the film (CdTe) and Ω_{CdTe} is atomic volume of

CdTe bulk. For the dislocation-free systems, Eq. (22) becomes

$$E_s = \frac{1}{2} E_f \varepsilon^2 \frac{2N_{Te}\Omega_{CdTe}}{2L_x L_z} \tag{23}$$

Equating Eqs. (21) and (23), we obtain an interfacial energy of $\rho = 0.01766$ eV/Å^2 from the MD data for the dislocation-free systems.

When dislocations are present, Eq. (22) involves three unknown parameters r_0, E_c, γ. The dislocation core radius and core energy determined above are for homogeneous CdTe and CdS compounds, and it is reasonable that these parameters changed in the inhomogeneous system. γ reflects the deviation of the apparent elastic properties of the mixed structure as compared to the elastic properties of the film (CdTe). As we discussed above, large core radius always satisfies linear elastic theory, and hence we set r_0 to the core radius of CdTe, $r_0 = 12.4596$ Å, which is larger than that of CdS. Under these conditions, only E_c and γ are unknown. We now compare our modified model, Eq. (22) or equivalently, Eq. (10), and the old model, Eq. (1), in terms of matching the MD data.

The results for the energy as a function of film thickness h at different dislocation spacings, as obtained from the MD simulations and the conventional model, are first examined in Fig. 5-9(a). Note that here the continuum model Eq. (1) is adjusted by including the dislocation core energy of CdTe. This improves the agreement of the continuum model with the MD data. It can be seen from Fig. 5-9(a) that for the dislocation free systems (S = infinity), and the systems where misfit dislocations almost exactly cancel the mismatch strain (i.e., the S = 33Å where the energy becomes almost independent of the film thickness h), the agreement between the continuum and the MD models are very good. However, for the films that contain dislocations but the residual mismatch strain is not zero, the continuum model deviates from the MD model pretty significantly.

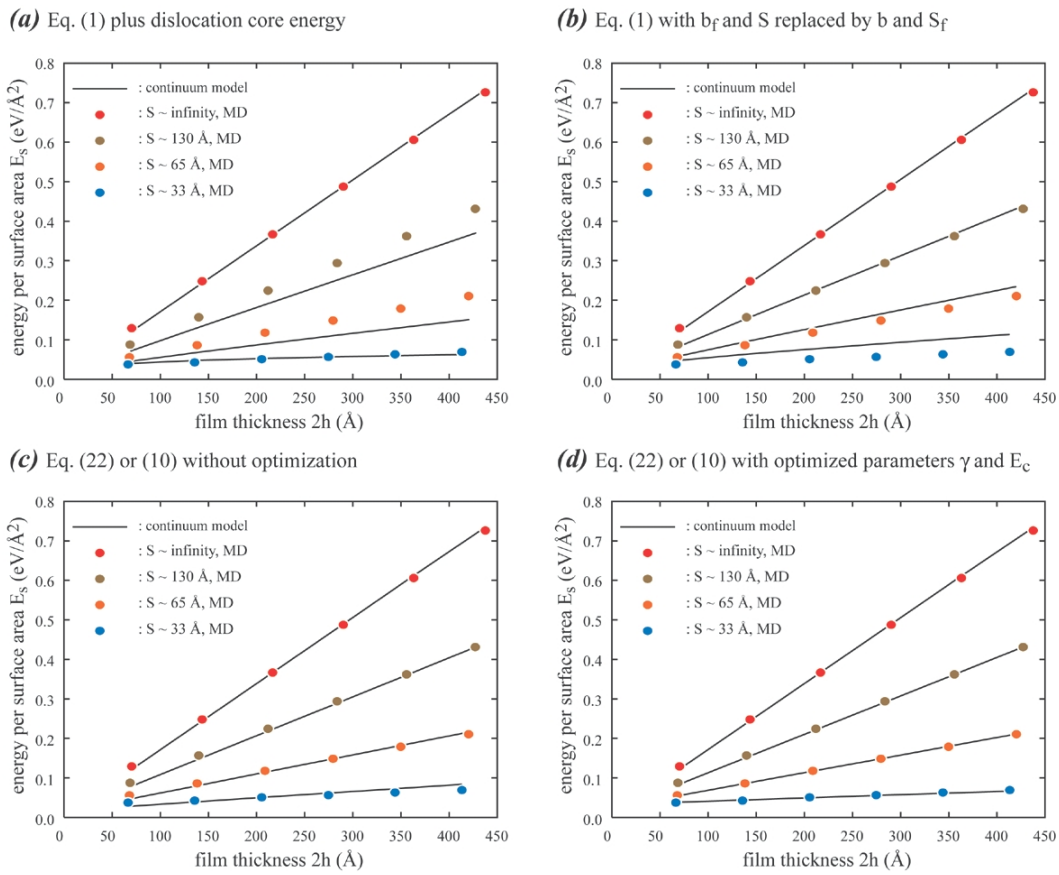

Figure 5-9. Comparison between the MD and continuum models: (a) the old continuum model Eq. (1) plus dislocation core energy; (b) Eq. (1) with the parameters b_f and S replaced by b and S_f, which is equivalent to the simplified new model Eq. (8) or (9); (c) modified model Eq. (22) or (10) without any optimization, i.e., □ = 1, and E_c = 1.2984 eV/Å (CdTe value); and (d) modified model Eq. (22) or (10) with optimized parameters □ = 0.8956 and E_c = 1.8726 eV/Å.

Step by step, we now replace the Burgers magnitude b_f and dislocation spacing S in Eq. (1) by b and S_f respectively according to their correct definitions discovered in this work. This is essentially the same as the simplified new model as described by Eq. (8) or (9). Similar MD and continuum data is shown in Fig. 5-9(b). It can be seen that significant improvement is achieved when dislocations are not too close, say S > 65 Å.

Now we examine the more accurate model, Eq. (22) or equivalently Eq. (10). Eq. (22) involves two parameters γ and E_c. We first test the validity of the model without fitting these two parameters, i.e., we simply set γ = 1 and E_c to be the CdTe value of 1.2984 eV/Å. The results obtained from the MD simulations and continuum calculations are shown in Fig. 5-9(c). Clearly, the new model further improves over the model shown in Fig. 5-9(b). The good agreement achieved at γ = 1 partially supports the conventional model which only uses elastic properties of the film. From Eq. (22) or (10), the elastic inhomogeneity only affects dislocation energy, but not the uniaxial mismatch strain energy in the film. It is therefore not surprising that the results are primarily determined by the elastic properties in the film. This problem, however, needs to be

further explored because coincidently, Table 5-1 shows that the compressive Young's modulus of CdTe is very close to the tensile Young's modulus of CdS (in our system, CdTe is subject to compression and CdS is subject to tension). This suggests that our system is elastically homogeneous. We point out that when calculating dislocation energies of CdS and CdTe in section V, we also have an elastic inhomogeneous problem. Edge dislocations always have one region in tension and another in compression so that they are subject to different elastic properties. The elastic inhomogeneity plays an obvious role because Table 5-1 indicates that the apparent Young's moduli determined from dislocation calculations are somewhere between the compressive and tensile Young's moduli. Yet the moduli are not particularly close to either. Nonetheless, the conditions are different as we do not fix the x- dimension of the material there, whereas here, we fix the x- dimension of CdS so that the effective thickness of the CdS substrate is much larger.

Without fitting any parameters, Fig. 5-9(c) strongly validates our new continuum model. Now we fully optimize our model by fitting γ and E_c to the MD data. Our optimization leads to $\gamma = 0.8956$, and $E_c = 1.8726$ eV/Å. This fully optimized new continuum model is compared with the MD in Fig. 5-9(d). Here the lines calculated from the continuum model are almost indistinguishable from the MD data, convincingly validating the legitimacy of making γ and E_c parameters flexible. In particular, at very small film thickness ~70 Å, the MD energy trends of different dislocation spacings are exactly reproduced by the continuum model. This is improved over Fig. 5-9(c). Accuracy at small film thickness is important for accurately determining the critical film thickness for dislocation formation. For example, Fig. 5-9 indicates that energies of the dislocation-containing systems are lower than those of dislocation-free systems even at the smallest 2h value explored (~70 Å), indicating that the critical thickness h is below 35 Å.

It is worth noting that the condition used in MD is not exactly the same as that used in the continuum model. In particular, in order to mimic the problem of a film on a semi-infinite substrate, we do not address the interaction of dislocations in different periodic MD cells along the y- direction. At the same time, we effectively mitigate the effect by fixing the MD x- and z-dimensions to the CdS sizes to keep the uniaxial strain field from propagating across the CdS periodic boundaries. It would be interesting to release the fixed boundary condition while significantly increasing the y- length of the CdS substrate (say two orders of magnitude). Unfortunately, this would require enormous computing resources. One significant impact of our work, however, is the creation of a robust MD approach that can guide the development of a continuum model for mismatched nanostructures, where the continuum theories are relatively immature, but the MD can more precisely represent the real structures. This means that the future continuum models for new misfit structures (e.g., core/shell particles) can be tuned and improved as they are being developed, because MD validation can be performed step by step by the same group of authors within a time frame much faster than performing experiments.

While being more accurate, our model is just as easy to apply as the old model. In fact, the only complexity introduced in Eq. (22) or Eq. (10) as compared to Eq. (1) is the one-argument function $f(x)/(4\pi x)$ where $x = (1-\varepsilon)h/S$. As for the unknown parameter γ, the condition $\gamma = 1$ is a

reasonable approximation. It simply means that the strain energy is predominantly determined by the elastic properties of the film due to the fact that uniaxial strain energy is proportional to the square of strain and the strain in the substrate is assumed to be zero. As for the unknown parameter core energy E_c, since the old model neglects this term, any reasonable value is likely to improve the results. Regardless, the robust MD approach demonstrated here can always be used to determine these parameters. In that case, our new continuum model can be made indistinguishable from the MD methods. Finally, we emphasize that the studies presented in this paper are rigorous only for mirror imaged interfaces rather than true surfaces. We are currently applying the same approach as established here to examine the case of free surfaces.

XXII. CONCLUSIONS

A systematic study combining continuum calculations and MD simulations has been performed to examine the misfit dislocation formation and strain relaxation problem. The numerous new physics discovered are useful for future researches on lattice mismatched systems where defect density and strain relaxation critically determine the performance. These are summarized below:

1. Time averaged MD simulations can produce much more converged results (essentially zero standard deviation considering three decimal points based on an average time of ~10 ns) than molecular statics, which is currently the most widely used method to calculate static properties of material but is constrained to 0 K temperature, small systems, and defects that do not relax to multiple local minimum energy configurations. This enables MD to be confidently used to validate continuum theories, which would be otherwise impossible;
2. When separate elastic constants are used for tensile and compressive deformation, the "linear elastic theory" can remain accurate for a much larger strain range than if a single elastic constant is used for both tensile and compressive deformation;
3. Continuum expressions of energies have been rigorously derived for both lattice mismatched systems and dislocation dipole arrays. The physics gained during the derivation of the former expression allow the continuum model of misfit dislocation formation to be improved. The latter expression allows the dislocation core radius and the core energy to be accurately calculated from MD simulations using exactly the same dipole array configurations without having to impose the continuum boundary condition – an approximation always used in the past to extend the MD length scales;
4. When applying Eq. (1) to homogeneous material (i.e., the system has dislocations but mismatch strain $\varepsilon = 0$), the energy reduces to $\frac{1}{2}\frac{2G_f h}{(1-\nu_f)}\cdot\left(\frac{b_f}{S}\right)^2 + \frac{G_f b_f^2}{4\pi(1-\nu_f)}\frac{1}{S}\ln\left(\frac{\beta\cdot h}{b_f}\right)$. Our work confirms that this indeed corresponds to the dislocation energy;

5. Lattice mismatched systems contain at least two elastic constants from the two materials. Even one material may involve two elastic constants if both compressive and tensile stresses are encountered (e.g., around an edge dislocation). Our work confirms that the conventional continuum theory, which typically uses only one elastic constant, can in fact remain accurate if an apparent elastic constant somewhere between the two elastic constants is used;
6. The S distance used in the continuum theory should not be measured in the deformed system, but rather measured in the unstrained film. The magnitude of Burgers vector should not be measured in the film, but rather measured in the substrate. Misuse of either of these parameters causes significantly error when the lattice mismatch of the system is large. Our improved model, Eq. (22) or (10), accounts for this effect, as well as dislocation core energy and elastic inhomogeneity effects. When a more accurate dislocation energy term is used and the parameters optimized, the continuum calculations using Eq. (22) or (10) are essentially indistinguishable from the MD simulations;
7. The robust approach outlined here provides a theoretical means (MD) to quickly validate future continuum models for new misfit structures (e.g., core/shell particles). The advantages cannot be overstated: the continuum model can be tuned and improved as it is being developed because the MD validation can be performed step by step by the same group of authors, rather than the publishing a continuum model and then correcting it after follow-on experimental data is created.

XXIII. 9. DISTRIBUTION

4 Lawrence Livermore National Laboratory
Attn: N. Dunipace (1)
P.O. Box 808, MS L-795
Livermore, CA 94551-0808

1	MS0115	OFA/NFE Agreements	10012
1	MS0161	Legal Technology Transfer Center	11500
1	MS0359	D. Chavez, LDRD Office	1911
1	MS0899	Technical Library	9536 (electronic copy)


Sandia National Laboratories